INTERNAL REPORT

SRT TEST ACTIVITIES PROPOSAL: SEARCH FOR RADIO PULSAR COUNTERPARTS IN THE ERROR BOXES OF UNIDENTIFIED GAMMA-RAY SOURCES

M. Marongiu, A. Pellizzoni*, E. Egron*,
M. Bachetti*, M. N. Iacolina*, A. Possenti* (#)

Report n. 47, released: 24/03/2015

Reviewer: M. Pilia

OAC Osservatorio Astronomico di Cagliari

Abstract

This technical note represents one of the starting points for the implementation and test of multi-frequency pulsar search procedures and observation programs with the ***Sardinia Radio Telescope*** (SRT). This radio telescope located in San Basilio (near Cagliari, Sardinia, Italy), works in the radio band in the nominal range 0.3 – 100 GHz, and it is characterized by a parabolic reflector with a diameter of 64 m.

The purpose of this technical note is the identification of a sample of unidentified gamma-ray sources (discovered by the *Fermi-LAT* and included in the *Third Fermi-LAT catalog*, 3FGL), that could potentially be associated and identified with pulsars through radio observations with SRT. Moreover, if in the error box of a gamma-ray source no pulsars are found, we propose the implementation of a procedure to detect radio sources of different nature, such as Pulsar Wind Nebulae (PWNe), Supernova Remnants (SNRs), Active Galactic Nuclei (AGNs) or binary systems. This multi-frequency experiment will be one of the first "targeted pulsar search" type of observation implemented with SRT.
Furthermore, this approach will contribute to improve the multi-frequency picture of pulsar physics from radio ($\gtrsim$10 MHz) to gamma-ray ($\gtrsim 10^{10}$ GHz). At present, the connections between the multi-frequency pulsar emissions are not obvious, if compared with other galactic or extragalactic sources (such as AGN).

A sub-sample of 22 targets have been selected among the brightest gamma-ray sources / pulsar candidates and ranked starting from a sample of 105 unidentified gamma-ray sources, compatible with pulsar like-characteristics.
Pulsar search strategies tailored on SRT were applied for each selected gamma-ray target in different radio bands together with optimal observing parameters.

(#) continued from cover page:

* INAF - Osservatorio Astronomico di Cagliari, Via della Scienza, 5 - 09047 Selargius (CA), Italia

This OAC/SRT Internal Report was created with LaTeX.

Contents

1 Introduction: search for radio pulsar counterparts of unidentified gamma-ray sources

This technical note represents a starting point for the implementation of specific strategies of pulsar observations with the ***Sardinia Radio Telescope*** (hereafter SRT).

The main purpose of this note is the identification, through a selection strategy (§5), of a sample of gamma-ray sources that could potentially be associated and identified with pulsars through radio observations. In particular, we have focused on the unidentified gamma-ray sources (i.e. gamma-ray sources without known counterpart at other wavelengths) that could be studied through radio observations with SRT.

A pulsar is a rapidly-rotating, highly-magnetized neutron star, surrounded by a plasma-filled magnetosphere. The modeling of its emission requires sophisticated electrodynamic calculations (e.g. Wang & Hirotani, 2011[87]; Pétri, 2012[60]). Throughout this technical note, we will call "ordinary" pulsars the objects (typically emitting in gamma-ray band) belonging to the young end of main population of the spin period (P) and period derivative ($\dot{P}$) plane (see §4 and Figure 4), in order to distinguish them from the much older "recycled" pulsars, including millisecond pulsars (MSPs) (e.g. Possenti, 2007[64]). All known gamma-ray pulsars (described in a specific Fermi catalog, §4), and the most promising candidates to date for further radio/gamma identifications are *Rotation-Powered Pulsars* (RPPs, Abdo et al., 2013[8]).

This multi-frequency research activity will constitute an important test of SRT performance, and later one of the first observational experiments of the type "targeted pulsar search" implemented with this radio telescope. In this case, targeted searches consist of scrutinizing the error boxes of unidentified gamma-ray sources in various bands of the electromagnetic spectrum, not only in order to find new pulsars with SRT, but also to study their radio counterparts possibly related to other types of astrophysical objects, such as Pulsar Wind Nebulae (PWNe), Supernova Remnants (SNRs), Active Galactic Nuclei (AGNs) or binary systems. If in the error box of a gamma-ray source no pulsars are found, our selection criteria could help to identify possible radio sources of a different nature.

A multi-frequency approach is necessary in order to provide a complete overview of the astrophysical phenomena. Presently, the connections between the multi-frequency radio/high energy emissions are not obvious for most Galactic and extragalactic sources, although they are possibly related in most cases (e.g. through synchrotron/inverse Compton processes) (e.g. Kaspi, 2010[40]; Petrova, 2009[61]).

The 3FGL catalog (§3) is a major outcome of the *Large Area Telescope* (LAT), the main instrument on board the *Fermi Gamma-ray Space Telescope* (§2.2). From this catalog (Acero et al., 2015[79]), we select a sample of unidentified gamma-ray sources that, based on their specific characteristics, can be considered good pulsar candidates.

For a long time the LAT has not yet detected significant gamma-ray pulsations from any accretion-powered pulsar nor from the magnetars, anomalous X-ray pulsars, and soft gamma repeaters for which the dominant energy source is magnetic field decay (Parent et al., 2011[57]). Recently there has been important progress in this field, thanks to multi-frequency observations of these sources, such as the low-mass X-ray binary system 1RXS J154439.4-112820, the most probable counterpart of the unassociated Fermi-LAT source 3FGL J1544.6-1125 (Bogdanov & Halpern, 2015[17]).

2 The Fermi Gamma-ray Space Telescope

2.1 Main gamma-ray scientific missions

The gamma radiation is mostly produced by non-thermal processes, resulting from interactions between high-energy particles, while in the case of scattered radiation, the emission results from the interaction between cosmic rays and the interstellar medium (ISM).
One among the most important gamma-ray missions was the *Compton Gamma-Ray Observatory* (CGRO), a satellite launched by NASA in 1991 and operative until 2000. This satellite included four instruments operating in the gamma bandwidth, including the *Energetic Gamma-Ray Telescope* (EGRET), operating at energies between 20 MeV and 30 GeV. CGRO produced a first map of galactic gamma-ray diffuse emission and detected several compact sources, including a few pulsars (Thompson, 2004[81]).

The successor to EGRET was the *Astro-rivelatore Gamma a Immagini LEggero* (AGILE). This small and powerful Italian satellite (Tavani et al., 2007[78]) is equipped with the latest generation instrumentation, that takes advantage of new technologies of solid state detectors. Currently AGILE is in operation, and is very effective for detecting and monitoring gamma-ray sources between 30 MeV and 50 GeV. This satellite is also able to study X-ray sources, through the presence of SuperAGILE, a tool that works in the hard X-ray band (10 – 40 keV). Despite having a frequency range comparable with EGRET, AGILE has a field of view larger than EGRET by a factor of 2 (2 sr, or approximately $\frac{1}{5}$ of the sky). AGILE increased the sample of gamma-ray pulsars (Pellizzoni et al., 2009[58]).

About one year after the launch of AGILE, in 2008 the *Fermi Gamma-ray Space Telescope* (FGST) was launched: this space telescope (`http://fermi.gsfc.nasa.gov/`) is the result of a collaboration between NASA and various international institutions (including INAF), and was designed to study the electromagnetic radiation emitted by gamma-ray sources between 8 keV and 300 GeV (Abdo et al., 2010[1]). FGST technology is similar to that of AGILE but its effective area is about one order of magnitude higher having allowed the discovery of about 150 pulsars!

2.2 The Fermi Gamma-ray Space Telescope

The FGST project includes two scientific instruments:

- the *Large Area Telescope* (LAT), a gamma-ray detector operating in the energy range 20 MeV – 300 GeV, designed for the study of gamma-ray sources;
- the *Gamma-ray Burst Monitor* (GBM), to investigate the transient phenomena at relatively lower energies (8 keV – 40 MeV).

The main scientific aims of FGST are:

- the study of the mechanisms of particle acceleration and emission of electromagnetic radiation in many types of sources, such as Active Galactic Nuclei (AGNs), pulsars and Supernova Remnants (SNRs);
- the study of high-energy emission in Gamma-Ray Burst (GRB);
- the study of unidentified gamma-ray sources and galactic and extra-galactic diffused gamma-ray radiation;
- the indirect detection of dark matter, through its decay or annihilation in photons (or electron-positron pairs).

2.2.1 The Large Area Telescope (LAT)

LAT is a fundamental instrument that allows us to study the properties of gamma-ray sources.

The operating principle of LAT is based on the fact that high-energy photons, in contrast to the visible light, interact with matter primarily through the process of production of electron-positron pairs. This detector, hence, is more similar to experimental devices of big particle accelerators for high energy physics than to a telescope.

The large effective area of collection ($\sim$ 6500 cm^2 at 1 GeV), the wide field of view ($\sim$ 2.4 sr at 1 GeV), basically the same as AGILE) and the excellent energy, angular and temporal resolution, allow us to increase sensitivity by more than 1 order of magnitude with respect to EGRET. Although the efficiency of observation is very high, there are two main limitations to the LAT observations (intrinsic to any gamma-ray satellite): (1) detection by LAT of a small number of gamma-ray photons for each observation; (2) interruptions of data acquisition during the passage of Fermi above an area where there is a particular magnetic anomaly (the South Atlantic Anomaly, SAA).

The tracking section of the LAT has 36 layers of silicon strip detectors interleaved with 16 layers of tungsten foil. In particular, this tracking section is composed of 12 thin layers (each one with 0.03 radiation length[1]) at the top (or *Front*) of the instrument, followed by 4 thick layers (each one with 0.18 radiation length) in the *Back* section.
Beneath the tracker is a calorimeter composed of an 8-layer array of CsI crystals ($\sim$ 8.5 total radiation lengths) to determine the gamma-ray energy of the incoming photon.
A segmented charged-particle anticoincidence detector (plastic scintillators read out by photomultiplier tubes) around the tracker is used to reject charged-particle background events.
For each gamma-ray photon, LAT measures its Time of Arrival (ToA), direction and energy. In particular:

- the ToA is measured when gamma-ray photons affect the silicon detector;
- the direction is estimated through conversion of each gamma-ray photon in a electron-positron pair in the tungsten, which in turn is tracked by the silicon detectors;
- the energy is measured through the absorption of the pair in the calorimeter.

FGST is used for most of the time in the *survey sky-scanning mode*: under standard conditions, LAT performs observations for about 35 minutes every 3 hours, covering approximately the entire sky each day.

Additional information about the LAT and its performance can be found in Atwood et al. (2009[13]), while calibration information can be found in Abdo et al. (2009[3]).

3 The Fermi-LAT catalog of Gamma-ray Sources

All the gamma-ray sources detected by the LAT since 4 August 2008 are included in a catalog. There is currently a revised version of this catalog (the third version, called 3FGL) updated to 31 July 2012, in which all detections of gamma-ray sources are based on the average flux measured during the first 4 years of observations (Figure 1). 3FGL contains

[1]The radiation length is a characteristic of a material, and is defined as the distance covered in a given material by an electron along which the electron reduces its energy by $1/e$.

sources distributed in the whole sky (Acero et al., 2015[79]), thanks to the large field of view of LAT and the observation strategy adopted (see §2.2.1).
Compared to previous catalogs, the 3FGL catalog benefits from higher-level improvements in the analysis, including an improved model for Galactic diffuse emission, and a refined method for source detection (see §3.1 and Acero et al., 2015[79]).

Each gamma-ray source is positioned within an eliptical *error box* (with a confidence level of 95%). 3FGL lists fluxes and spectra, fitted as power-law, power-law with an exponential cutoff, or log-parabola form (for further details, see §4.3.6 of this technical note and §3.3 of the paper by Acero et al., 2015[79]).
3FGL indicates if the positional error boxes of the sources include known astrophysical objects, having counterparts at other frequencies, described in other astronomical catalogs (see §3.3.2), such as the radio pulsar database of the Australia Telescope National Facility (ATNF; Manchester et al., 2005[49])[2].

The 3FGL catalog contains 3033 sources[3] detected in the energy bandwidth 100 MeV – 300 GeV (Table 1): 1786 likely belong to the classes of known (or suspected) sources that produce gamma-rays (§3.3.2), and only 238 are firmly identified (§3.3.1), mostly with AGNs and pulsars. The remaining sources (1009) are unidentified (§3.4.5): the identification of the nature of these sources represents an important goal for High Energy Astrophysics.

More information about 3FGL, such as models of observation, structure of this catalog, associations and identifications of sources, are available in the recent paper by Acero et al. (2015[79]).
In the following subsections we describe the main statistical tools for the detection of gamma-ray sources and the source classes contained in the catalog.

3.1 Detection of a gamma source and significance

The process of detection of gamma-ray sources involves a three steps iterative process:

1. identification of potential point sources, denoted as *seeds*, that have not already been selected in a previous iteration;

2. a full all-sky optimization of a model of the gamma-ray sky (diffuse emission plus sources), including the new seeds to refine their estimated positions and evaluate their significances;

3. creation of a "*residual Test Statistic (TS) map*".

In particular, the model for the diffuse gamma-ray background was further updated for the 3FGL analysis and consists of several components, such as:

- the diffuse gamma-ray emission of the Milky Way, originated by the cosmic-ray interactions with interstellar gas and radiation;

- the approximately isotropic background consisting of emission from sub-threshold celestial sources plus residual charged particles misclassified as gamma-rays;

[2] http://www.atnf.csiro.au/people/pulsar/psrcat/
[3] Table 1 has 3034 entries because the PWN component of the Crab nebula is represented by two cospatial sources (Acero et al., 2015[79]).

- the "passive" emission of the Sun and Moon from cosmic-ray interactions with the solar atmosphere, solar radiation field, and the lunar lithosphere, as effectively a diffuse component, because the Sun and Moon move across the sky.

Further details of this model are provided in Acero et al. (2015[79]).

The *significance* of detection of a gamma-ray source $signif_{avg}$ is defined through an important statistical tool, called *Test Statistic* (TS), which quantifies how much gamma-ray signal emerges significantly from the Galactic background radiation.
TS is evaluated as:

$$TS = 2(\log \mathcal{L}_{source} - \log \mathcal{L}_{nosource}) \quad (1)$$

where $\mathcal{L}$ represents the maximum likelihood that the model with ($\mathcal{L}_{source}$) or without ($\mathcal{L}_{nosource}$) a new source (in a given position on the sky) describes correctly the real data. The likelihood $\mathcal{L}$ is maximized with respect to the adjustable parameters of the model, by splitting the sky into *Regions of Interest* (RoI) (further details in Mattox et al., 1996[52]).

$signif_{avg}$ corresponds approximately to $TS^{0.5}$. The detection threshold is considered of $TS > 25$, corresponding to a significance of just over 4σ evalutated from the χ^2 distribution with 4 degrees of freedom (position and spectral parameters, Mattox et al. 1996[52]).

In the 3FGL significance analysis there are many improvements with respect to 2FGL (Nolan et al., 2012[55]).
The most important improvement consists to taking into account the different instrumental backgrounds in the *Front and Back events*[4]. This developement resulted in lower TS (fewer sources) and tended to underestimate the low-energy flux. The impact is largest at high latitude. In order to solve the problem, in 3FGL they used different isotropic spectral templates for Front and Back events (but a common renormalization parameter) and different Front and Back models of the Earth limb. The same distinction was introduced for computing the temporal variability (3.2).
Another improvement is the integration of the model of the Sun and Moon contributions, without any adjustment or free parameter in the likelihood analysis.
Further details of these improvements are provided in Acero et al. (2015[79]).

3.2 Variability

Temporal variability is relatively common on various timescales in gamma-ray sources and it provides a powerful tool to firmly associate them with known objects at other wavelengths and to study the physical processes that power them.

To define the variability of a source, the flux of its gamma-ray photons [5] $\mathcal{F}$ is measured as a function of time over the whole energy range (100 MeV – 100 GeV). The counts of gamma-ray photons are put into a histogram (*light curve*). Because the number of photons is relatively low (§4.3.5), the time binning of the light curve is not performed on a daily basis, but usually monthly.

Variability of each source is measured by the *variability index* $\mathcal{V}$. The variability index is defined as a TS (§3.1), that can be expressed as a sum of terms for the individual time

[4] Separating the photons according to event type is important, especially for the source localization, since the Front-converting events in the tracking section of the LAT (see §2.2.1) are processed differently than the Back-converting events. Thus in the the detection and localization analysis is very important to take into account both these event types (Front, Back).
Further details of this effect are provided in Acero et al. (2015[79]).

[5] The gamma-ray photon flux $\mathcal{F}$ is measured in photons s^{-1} cm^{-2}.

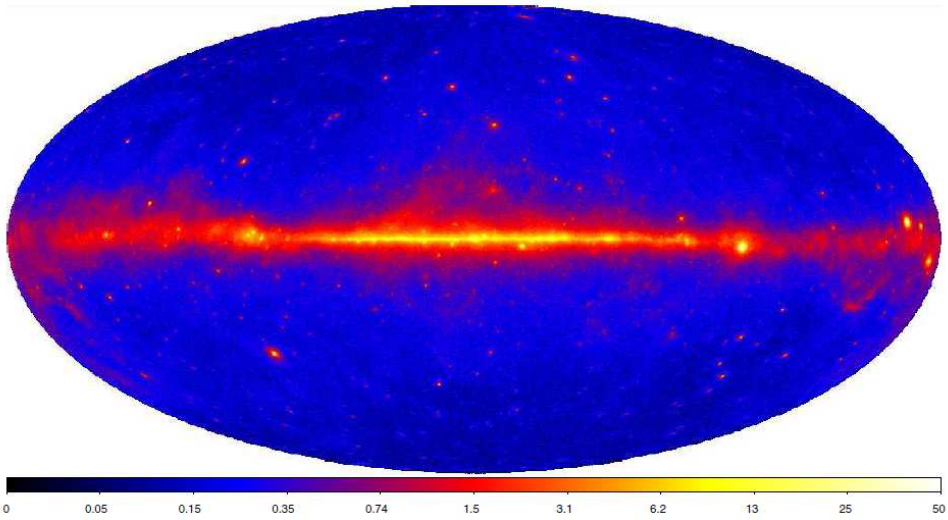

Figure 1: *Sky map of the energy flux (Aitoff projection in Galactic coordinates) derived from the LAT data after 2 years of observations. The image shows gamma-ray energy flux for energies between 100 MeV and 10 GeV, in units of* 10^{-7} *erg* cm^{-2} s^{-1} sr^{-1}.
The energy flux is mostly distributed in a diffused horizontal line, which traces the Galactic plane. Other small diffused regions out of this plane show a high flux, most likely in correspondence with AGNs.
Image taken from Nolan et al., 2012[55].

intervals of observation i, that is:

$$\mathcal{V} = TS_{var} = 2\sum_i [\log \mathcal{L}_i(\mathcal{F}_i) - \log \mathcal{L}_{cost}(\mathcal{F}_{cost})] \tag{2}$$

where $\mathcal{L}$ represents the maximum likelihood that the model (§3.1), in which the measurement of $\mathcal{F}$ is constant over time ($\mathcal{L}_{cost}(\mathcal{F}_{cost})$) or variable for each time interval of observation i ($\mathcal{L}_i(\mathcal{F}_i)$), correctly describes the real data.
These time intervals are not uniform, and correspond to about one month: the empirical limit to identify variable sources is fixed to the threshold of $\mathcal{V}_s = 72.44$, corresponding to 99% confidence in a χ^2 distribution with 47 degrees of freedom (Acero et al., 2015[79]). All sources with $\mathcal{V} \leq \mathcal{V}_s$ are assumed to have a constant flux, while all sources with $\mathcal{V} \geq \mathcal{V}_s$ have a variable flux. 21.3% (647/3033) of the 3FGL sources are found to be significantly variable on monthly timescales.
The 3FGL catalog, for the variability analysis took into account the new model for the diffuse gamma-ray background and the Front and Back events (see §3.1).

3.3 Source association and identification

As we can notice from Table 1, it is possible to make a distinction between tentative multi-frequency source associations (depending primarily on close positional correspondence) and firm identifications.

3.3.1 Firm identifications

Although many associations, particularly those for AGNs, have very high probability of being true, a firm identification can be done based on one of three criteria:

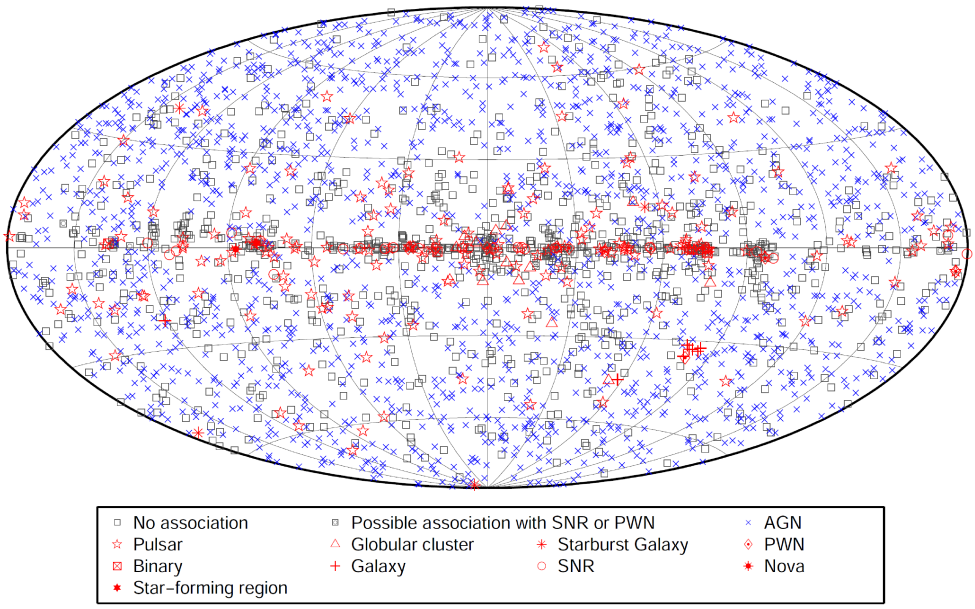

Figure 2: *Full sky map showing sources by source class (see Table 1). All AGN sub-classes are plotted with the same symbol for simplicity.*
Image taken from Acero et al., 2015[79].

1. *Periodic variability*. Pulsars are the larger class in this category, and their firm identification means that pulsed gamma-rays have been seen from the source with a probability of the periodicity occurring by chance of less than 10^{-6}.

2. *Spatial morphology*. Spatially extended sources whose morphology can be related to that seen at other wavelengths include SNRs, Pulsar Wind Nebulae (PWNe, see §3.4.3) and galaxies.

3. *Correlated variability*. Variable sources, primarily AGNs, whose gamma-ray variations can be matched to variability seen at one or more other wavelengths, are considered firm identifications. Although some cases are well documented, such correlated variability is not always easily defined. This criterion conservatively requires data in more than two energy bands for comparison.

3FGL include one exception to these rules. The Crab PWN is listed as a firm identification even though it does not meet any of these criteria. The well-defined energy spectrum distinct from the Crab pulsar spectrum and matching spectra seen at both lower and higher energies provide a unique form of identification (Abdo et al., 2010[4]).
In total, only 7.9% (238/3033) of 3FGL sources are firmly identified (see Table 1).

3.3.2 Automated source associations

The discovery of gamma-ray sources counterparts in the radio (or in other bands of the electromagnetic spectrum) has significantly improved in the last few years thanks to the LAT.

The approach for automated source association is Bayesian, namely it trades the positional coincidence of possible counterparts with 3FGL sources against the expected number of chance coincidences to estimate the probability that a specific counterpart association is

indeed real (i.e., a physical association). 3FGL retains counterparts as associations using the Bayesian method at the 80% confidence level. This method is applied to a set of counterpart catalogs[6] for which the prior source association probabilities are calibrated using Monte Carlo simulations of fake 3FGL catalogs. Many independent simulations are required for each catalog (between 100 and 1000), so that the relative accuracy in the expected false association rate is determined to better than 5% for each catalog. This method improves the precision of the probability computations for catalogs that have only few associations with 3FGL sources.
For some counterpart catalogs the Bayesian method could not be applied since either (1) the location uncertainty of the counterpart is larger than the location uncertainty of the 3FGL source or (2) the counterpart is an extended source. In the first case, all objects for which the separation from the 3FGL source is less than the quadratic sum of the 95% confidence error radii are considered a potential association. In the second case, it is assumed that the counterparts have circular extensions and all objects whose extension circle overlaps with the 95% confidence error radius of the 3FGL source is considered an association. For elliptical error regions the semimajor axis is taken as the error radius.
Further details of the Bayesian method are provided in Abdo et al. (2010[2]).

In total, about 58.9% (1786/3033) of the 3FGL sources are associated with counterparts in various bands of the electromagnetic spectrum by the automated procedure (see Table 1).

3.4 Source types in 3FGL

The identified and associated sources in the 3FGL catalog include many Galactic and extragalactic source classes. In particular, all 3033 gamma-ray sources of 3FGL are divided into 21 different types (see Figure 2). In Table 1 we describe these source types in terms of their main characteristics useful for the purpose of this technical note: the galactic latitude b, the variability $\mathcal{V}$ (§3.2), the photon spectral index γ, and the energy flux (in the range 0.1 – 100 GeV) G_{100} (§4.3.1).

3.4.1 Active Galactic Nuclei

AGNs, and in particular blazars, are the largest class of extragalactic sources in 3FGL at high Galactic latitudes. In 3FGL there are 1746 AGNs (see Table 1), of which 66 are firmly identified and 1680 are associated sources: among these sources there are 1144 blazars (660 BL Lac objects[7] and 484 Flat Spectrum Radio Quasars), 573 of unknown type (candidate blazars), 16 radio galaxies, 6 Seyfert galaxy (among them 5 Narrow Line Seyfert 1[8]), 4 Quasars (3 Soft spectrum Radio Quasars and 1 Compact Steep Spectrum Quasar), 3 non-blazars active galaxies.

AGNs observed by the LAT are also sources of radio (and X-ray) emission, and there is a clear trend that AGNs associated with 3FGL sources have larger radio fluxes than the average object in the counterpart catalogs (Ghisellini & Tavecchio, 2015[34]). This trend already was exploited for the association of blazars in the EGRET catalog (Sowards-Emmerd et al., 2003[75]).

[6] For the automated association of 3FGL gamma-ray sources, catalogs such as ATNF, the updated (to 2010) Globular Cluster database (Harris, 1996[36]), or the catalogs of radio and TeV sources are used.

[7] BL Lac objects are a subclass of AGNs, and usually tend to have the lowest bolometric luminosities and their second emission peaks at the highest energies.

[8] The narrow-line Seyfert 1 galaxies are a subclass of the Seyfert galaxies, and they have been established as a new class of gamma-ray active AGN (Abdo et al., 2009[6]).

The increase in the number of AGN candidates is mainly due to association methods contained in the companion 3LAC catalog (Ackermann et al., 2015[10]). In 3LAC, as in 2LAC (Ackermann et al., 2011[9]), there is another association method next to the automatic one described above (see §3.3.2). This is the *Likelihood Ratio method* (LR), frequently used to assess identification probabilities for radio, infrared and optical sources (e.g., de Ruiter et al., 1977[28]; Ackermann et al., 2011[9]). It is based on uniform surveys in the radio and in X-ray bands, enabling us to search for possible counterparts among the faint radio and X-ray sources. For further details about this association method, see 3LAC catalog (Ackermann et al., 2015[10]).

According to source associations and/or identifications, in the 3FGL catalog 37.7% (1144/3033) of gamma-ray sources are blazars and 18.9% (573/3033) are active galaxies of uncertain type (designated as "*bcu*" in Table 1). The increase of "bcu" can be explained by the extensive use of radio and X-ray surveys in the 3LAC association procedure[9].
In general, AGNs are isotropically distributed in the sky, but from Table 1 the main parameters say of these sources show that they are mostly detected at high galactic latitudes ($b_{RMS} = 42.66$): this fact suggests that these sources are more difficult to detect in the Galactic plane because of the strong contribution of the ISM effects. At high latitudes AGNs are less affected by the Galactic background, and therefore each source has an error box smaller than other sources of a different class. Moreover, these sources have an extremely variable flux over time (the highest variability in 3FGL, $\mathcal{V}_{av} = 231.45$), and the energy flux G_{100} is not very high ($G_{100,av} = 0.16 \cdot 10^{-10}$ erg s^{-1} cm^{-2}).

3.4.2 Supernova Remnants

SNRs represent a special class because they are usually extended enough to be potentially resolved with the LAT.
3FGL contains 23 SNRs: 12 are firmly identified and 11 are associated with SNRs (Table 1).
According to the most widely accepted evolutionary scenario related to the formation of neutron stars (Fryer, 1999[33]), a SNR may contain a neutron star (eventually seen as a pulsar which could power a PWN or being a component of a High Mass Binary, HMB). In the 3FGL catalog there are also 49 potential associations with either SNRs or PWNe (designated as "*spp*" in Table 1). This illustrates the relatively large uncertainty that is tied to these associations and it represents an additional warning to treat these potential associations with great care.

From Table 1, the main parameters of SNRs indicate that these sources are mainly positioned at low galactic latitudes ($b_{RMS} = 2.39$), as expected from evolutionary scenario and location along the Galactic plane (Fryer, 1999[33]). Moreover, these sources have a constant flux over time ($\mathcal{V}_{av} = 61.58$), and a high energy flux G_{100} ($G_{100,av} = 1.44 \cdot 10^{-10}$ erg s^{-1} cm^{-2}).

3.4.3 Pulsars and Pulsar Wind Nebulae

Because pulsed emission can be such a clear signature, pulsars represent the largest class of firmly identified astrophysical objects in the 3FGL catalog. 3FGL contains 167 pulsars: 143 are firmly identified by the LAT through the detection of gamma-ray pulsations and 24

[9] In 3LAC, sources of the "bcu" type have been divided into three sub-types depending of the multi-wavelength information available to characterize their "blazarness". For further details, see 3LAC catalog (Ackermann et al., 2015[10]).

are associated with pulsars, but no pulsations have yet been observed by the LAT.
From Table 1, the main parameters of pulsars highlight that these sources are mostly positioned at low galactic latitudes ($b_{RMS} = 21.47$) because of their evolutionary scenario and typical birth location along the Galactic plane (Fryer, 1999[33]). Moreover, these sources have a fairly constant flux over time ($\mathcal{V}_{av} = 52.47$), and one of the highest energy flux G_{100} in 3FGL ($G_{100,av} = 1.63 \cdot 10^{-10}$ erg s^{-1} cm^{-2}).
Further information about gamma-ray pulsars will be given in section 4.3.

A Pulsar Wind Nebula (PWN) is a nebula powered by the stellar wind of a pulsar. In the early phases of their evolution ($\tau_c \sim 10^5$ yr), PWNe are often located inside the shells of SNRs; however, there are older PWNe without SNRs (see for example, Stappers et al., 2003[76]). Among the known PWNe, Vela PWN was discovered in the gamma-ray energy range from 100 MeV to 3 GeV, through a specific methodology for the data analysis from the AGILE satellite: this discovery establishes a class of gamma-ray emitters that could account for a fraction of the unidentified Galactic gamma-ray sources (Pellizzoni et al., 2010[59]). An important prototype of PWN is the Crab Nebula (Hester et al., 2008[38]).

3FGL contains 12 PWNe: 10 are firmly identified and 2 are associated with PWNe (Table 1).
These sources are mostly positioned in the Galactic plane ($b_{RMS} = 10.62$), as shown in Table 1, because of their evolution cycle (§3.4.2), and have a slightly variable flux over time ($\mathcal{V}_{av} = 91.65$). Compared to gamma-ray pulsars, PWNe typically have lower energy flux G_{100} ($G_{100,av} = 1.46 \cdot 10^{-10}$ erg s^{-1} cm^{-2}).

3.4.4 Other source types

3FGL includes 3 High-Mass Binary (HMB) systems, all of which have been firmly identified through their orbital modulation. No further 3FGL source is associated with a High-Mass X-ray Binary (HMXB) from Liu's catalog (Liu et al., 2006[46]).

Normal (not active) galaxies are now established as a class of high-energy gamma-ray emitters (Abdo et al. 2010[7]), and the gamma-ray emission is powered by cosmic-ray interactions with interstellar gas and radiation.
In 3FGL there are 7 normal galaxies: 2 are firmly identified, and 5 are associated with such objects. In particular, 4 associated sources are classified as starburst galaxies (designated as "*sbg*" in Table 1), that are the most luminous among the normal galaxies and have very high densities of gas and massive star formation near their centers.

The number of globular clusters associated with LAT sources continues to grow. In 3FGL there are 15 gamma-ray sources associated with globular clusters. These sources have among the most constant fluxes over time ($\mathcal{V}_{av} = 48.01$) in the 3FGL catalog.

3.4.5 Properties of unassociated sources

Among the 3033 sources in the 3FGL catalog, 2024 (66.7%) have associations or identifications with known astrophysical objects, and 1009 remain unassociated. Moreover, among these unassociated sources are many that were found in previous LAT catalogs, indicating that some persistent mysteries remain despite extensive efforts to find associations over the past few years. The continued prevalence of unassociated sources is expected, as the improvement in sensitivity with four years of flight data and improvements to the characterization of backgrounds have allowed Fermi-LAT to probe the gamma-ray sky to unprecedented depths. As a result, direct comparison to previous LAT catalogs is difficult.

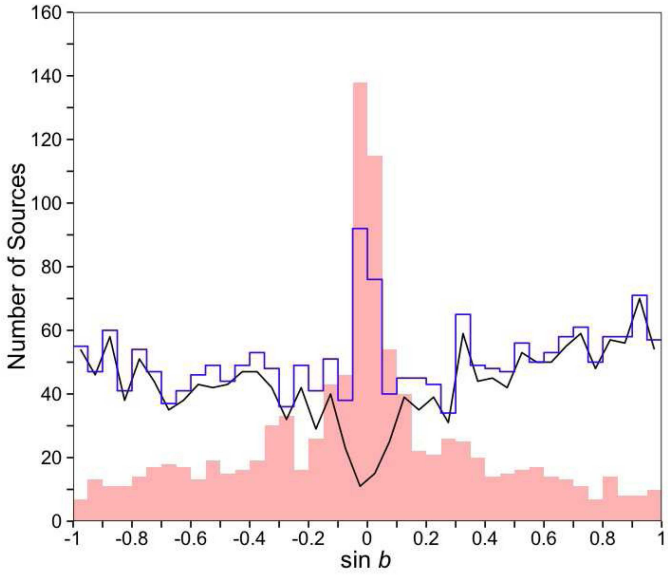

Figure 3: *Distributions in Galactic latitude b of unassociated sources (shaded red region), all associated sources (blue histogram) and all active galaxy source classes (black line). Binned in sine of b, an isotropic distribution would be flat.*
Image taken from Acero et al., 2015[79].

The distribution of unassociated sources on the sky is compared in Figure 3 to the distribution of the associated sources. The plot reveals some important features that should be kept in mind when considering unassociated 3FGL sources.

1. The number of unassociated sources decreases with increasing Galactic latitude b, with the decrease being steeper at positive latitudes (see Figure 3). This asymmetry may be due to relative completeness in the north versus the south of the counterpart catalogs used for the source association analysis (§3.3.2).

2. The numbers of unassociated sources increase sharply below $|b| \approx 10°$. This could be related to the relative lack of sources below $|b| < 10°$ in many of the extragalactic source catalogs used for source association. The Milky Way is a bright source of radio emission limiting sensitive searches for extragalactic sources near the Galactic plane. Furthermore, optical identifications of radio sources are hampered by the strong interstellar obscuration, leaving many radio sources unclassified.

3. A substantial fraction of the unassociated sources have at least one analysis flag set[10]. 40% of the unassociated sources have been flagged due to various issues. Moreover, 57% of these flagged sources is located within the Galactic plane, which reflects the complexity of the Galactic diffuse emission (Acero et al., 2015[79]). Because of the difficulties in source detection against the bright diffuse background along the Galactic plane, unassociated sources with analysis flags set should be considered with caution.

[10]Flags are a number of conditions that can shed doubt on a source. The 3FGL catalog contains about 650 flagged sources.
In the FITS version of 3FGL, these flags are summarized in a single integer column with a specific character; in particular, the designator "c" appended to names of 78 flagged sources indicates probable imperfections in the model for Galactic diffuse emission. Their position, emission characteristics, or even existence may not be reliable.

That difficulty is acute specially in the Galactic bulge (within 5° of the Galactic center), a region on top of bright diffuse emission. Until now, no model has been developed for those regions, so the source positions and characteristics there are not as reliable as in the extragalactic sky. Finally, the fact that such a large fraction of unassociated sources are flagged may indicate that some of these sources are indeed not real. We emphasize that the analysis flags should be taken into consideration when using 3FGL.

Understandably, the main parameters of these sources (labelled in Table 1 with "*und*") are distributed in a fairly broad range. In particular, these sources have a low variability ($\mathcal{V}_{av} = 47.76$), a galactic latitude partly compatible with galactic sources ($b_{RMS} = 27.63$) and a low energy flux ($G_{100,av} = 0.13 \cdot 10^{-10}$ erg s^{-1} cm^{-2}).

According to specific reasonings on the density of populations, among unidentified sources there could be associations with AGNs (about 15%), PSRs (about 40%), SNRs (about 37%) and other sources (about 8%).

Table 1: *Summary of the 16 gamma-ray sources types and their main features.*
The rows labelled with "AGN" (Active Galactic Nucleus), "GAL" (Galaxy), "BIN" (Binary system) and "PSR" (Pulsar) in green field indicate the overall values of the entire class in question.
The slots in yellow field indicate the relevant parameters for each class of source.

Class	Type	Idn	Asc	Tot	b_{min} [deg]	b_{max} [deg]	b_{RMS} [deg]	$\mathcal{V}_{min}$	$\mathcal{V}_{max}$	$\mathcal{V}_{av}$	Γ_{min}	Γ_{max}	Γ_{av}	$G_{100,min}{}^{(a)}$	$G_{100,max}{}^{(a)}$	$G_{100,av}{}^{(a)}$
	agn	0	3	3	18.40	68.26	50.48	57.80	3683.86	1368.85	2.04	2.57	2.37	0.11	0.48	0.24
	bcu	5	568	573	-85.75	85.10	35.56	22.94	3202.14	85.37	1.13	3.02	2.19	0.02	0.78	0.08
	rdg	3	13	16	-56.70	74.51	38.87	24.26	622.21	89.33	1.87	2.79	2.19	0.02	1.99	0.27
AGN	sey	0	1	1	-3.78	-3.78	3.78	55.42	55.42	55.42	2.43	2.43	2.43	0.13	0.13	0.13
	css	0	1	1	80.84	80.84	80.84	39.02	39.02	39.02	2.60	2.60	2.60	0.04	0.04	0.04
	bll	18	642	660	-87.66	86.37	46.65	24.24	5716.50	113.11	1.26	2.81	2.02	0.02	3.83	0.16
	fsrq	38	446	484	-86.33	84.38	44.75	30.68	60733.90	563.59	1.64	3.10	2.42	0.02	12.34	0.26
	nlsy1	2	3	5	-31.83	50.26	37.19	57.45	985.87	371.45	2.28	2.61	2.42	0.08	0.49	0.24
	ssrq	0	3	3	-38.19	30.17	31.20	40.48	117.52	91.51	2.37	2.47	2.42	0.05	0.19	0.10
	AGN	66	1680	1746	-87.66	86.37	42.66	22.94	60733.90	231.45	1.13	3.10	2.19	0.02	12.34	0.16
	gal	2	1	3	-44.42	-21.55	34.24	39.55	68.50	50.65	2.02	2.56	2.27	0.06	1.92	0.80
GAL	sbg	0	4	4	-87.95	40.54	55.35	39.80	57.51	48.92	2.17	2.43	2.28	0.07	0.14	0.10
	GAL	2	5	7	-87.95	40.54	47.47	39.55	68.50	49.66	2.02	2.56	2.28	0.06	1.92	0.40
	hmb	3	0	3	-1.69	1.09	1.38	42.29	344.33	152.33	2.19	2.55	2.37	2.50	4.73	3.35
BIN	bin	1	0	1	-0.63	-0.63	0.63	57.50	57.50	57.50	2.39	2.39	2.39	1.38	1.38	1.38
	BIN	4	0	4	-1.69	1.09	1.24	42.29	344.33	128.62	2.19	2.55	2.38	1.38	4.73	2.85
	GLC	0	15	15	-44.90	19.47	16.23	37.20	75.42	48.01	1.77	2.64	2.22	0.04	0.73	0.21
	NOV	1	0	1	-0.50	-0.50	0.50	286.41	286.41	286.41	2.55	2.55	2.55	0.10	0.10	0.10
	SFR	1	0	1	1.40	1.40	1.40	-	-	-	2.18	2.18	2.18	6.57	6.57	6.57
	SNR	12	11	23	-8.56	4.67	2.39	31.29	110.99	61.58	1.51	2.48	2.08	0.06	5.36	1.44
	SPP	-	49	49	-6.25	9.93	2.57	23.32	104.96	51.27	1.79	2.84	2.39	0.05	2.69	0.39
	psr	143	24	167	-68.07	71.25	21.47	20.01	621.93	52.47	0.50	3.12	1.68	0.02	89.30	1.63
PSR	pwn	10	2	12	-35.71	0.14	10.62	35.56	269.87	91.65	1.57	5.72	2.28	0.05	3.93	1.46
	PSR	153	26	179	-68.07	71.25	20.92	20.01	621.93	54.47	0.50	5.72	1.72	0.02	89.30	1.62
	UND	-	-	1009	-84.07	84.04	27.63	24.93	510.76	47.76	1.10	3.12	2.34	0.02	2.31	0.13

[a] G_{100} is in units of 10^{-10} erg s^{-1} cm^{-2}.

Note – Columns 1 and 2 list the source class and the source type. Columns 3, 4 and 5 list the firm identifications (Idn), the associations (Asc) and the total amount ($Tot = Idn + Asc$). Columns 6, 7 and 8 list the minimum, the maximum and the rms of galactic latitude (b_{min}, b_{max} and b_{RMS}). Columns 9, 10 and 11 list the minimum, the maximum and the average value of variability ($\mathcal{V}_{min}$, $\mathcal{V}_{max}$ and $\mathcal{V}_{av}$). Columns 12, 13 and 14 list the minimum, the maximum and the average value of photon spectral index (Γ_{min}, Γ_{max} and Γ_{av}, see §3). Columns 15, 16 and 17 list the minimum, the maximum and the average value of energy flux in range 0.1 – 100 GeV ($G_{100,min}$, $G_{100,max}$ and $G_{100,av}$).
Moreover, "*agn*" indicates non-blazar Active Galaxy; "*bcu*" indicates Active Galaxy of Uncertain type; "*rdg*" indicates Radio Galaxy; "*sey*" indicates Seyfert Galaxy; "*css*" indicates Compact Steep Spectrum Quasar; "*bll*" indicates BL Lac type of blazar; "*fqsr*" indicates Flat Spectrum Radio Quasar; "*nlsy*1" indicates Narrow line Seyfert 1; "*ssrq*" indicates Soft Spectrum Radio Quasar; "*gal*" indicates Normal Galaxy, or part; "*sbg*" indicates Starburst Galaxy; "*hmb*" indicates High Mass Binary; "*bin*" indicates Binary; "*GLC*" indicates Globular Cluster; "*NOV*" indicates Nova; "*SFR*" indicates Star-forming region; "*SNR*" indicates Supernova Remnant; "*SPP*" indicates potential association with SNR or PWN; "*psr*" indicates pulsar; "*pwn*" indicates Pulsar Wind Nebula.

4 The Fermi-LAT catalog of Gamma-ray Pulsars

As of March 2015, 2405 pulsars are reported in the ATNF pulsar catalog. Most of these pulsars were discovered in the radio band, while a small number was identified in optical, X and gamma-ray bands, and as even smaller group does not have any radio counterpart. The constant increase of gamma-ray pulsars detected since the launch of FGST required a continuous updated catalog for these pulsars. This catalog is relevant for our work in order to know both methods of discovery (§4.1) and main global characteristics of gamma-ray pulsars (§4.3). This could ease the search for further radio pulsar as possible counterparts of unidentified gamma-ray sources.

The *second Fermi-LAT Catalog of Gamma-ray Pulsars* (2PC) reports 117 high-confidence ≥ 0.1 GeV gamma-ray pulsar detections (see Table 2) from three years of data acquired by the LAT (Abdo et al., 2013[8])[11].
Roughly half (40 ordinary and 20 MSPs) of the gamma-ray pulsars in this catalog were known in radio and/or X-rays prior to the launch of FGST (§4.2.1). The remaining pulsars were discovered thanks to the LAT, with 36 being ordinary pulsars found in blind searches on LAT data (§4.2.2) and 21 (1 ordinary and 20 MSPs) found in radio searches for unassociated LAT sources (§4.2.3). 2PC reported pulsations for 93% of the 3FGL detected pulsars. The missing 7% did not reach the 3FGL detection threshold ($TS > 25$) of gamma-ray sources (see §3.1 and Acero et al., 2015[79]).
This catalog has expanded the results of the *first Fermi-LAT Catalog of Gamma-ray Pulsars* (1PC, Abdo et al., 2010[5]), the pulsar sample growing from 46 (six data months) to 117 (36 months).
2PC is a milestone in progress toward the long-term goal of acquiring a significant sample of gamma-ray pulsars, so that comparisons with model predictions (e.g. Gonthier et al., 2007[35]; Pierbattista et al., 2012[62]) will allow improved tests of emission models and of their links with their parent population of massive stars or with diffuse Galactic emission.

The pulsar spindown rate $\dot{P}$ versus the rotation period P of all 117 gamma-ray pulsars is shown in the $P\dot{P}$ diagram (see Figure 4). This diagram presents three physical parameters derived from the timing information: characteristic age τ_c, magnetic field at the neutron star surface B_S and spin-down luminosity $\dot{E}_{rot}$.
These parameters are derived as, respectively:

$$\tau_c = \frac{P}{2\dot{P}} \text{ yr} \tag{3}$$

$$B_S = 3.2 \cdot 10^{19} \sqrt{P\dot{P}} \text{ G} \tag{4}$$

$$\dot{E}_{rot} = -I \left(\frac{2\pi}{P}\right)^2 \left(\frac{\dot{P}}{P}\right) \text{ erg s}^{-1} \tag{5}$$

where I is the moment of inertia of the neutron star[12].
The observations of gamma-ray pulsars contained in this catalog will allow us to obtain

[11] As of March 2015, there are 161 gamma-ray pulsars: in addition to the 117 pulsars of 2PC, there are 44 other gamma-ray pulsars discovered both as 2PC neared completion, and by the LAT collaboration or by other groups using public LAT data having publications in preparation. An updated list of gamma-ray pulsars is available at https://confluence.slac.stanford.edu/display/GLAMCOG/Public+List+of+LAT-Detected+Gamma-Ray+Pulsars.

[12] The moment of inertia I of neutron star is assumed to be 10^{45} g cm^3 ("Handbook of Pulsar Astronomy", Lorimer & Kramer, 2005[47]).

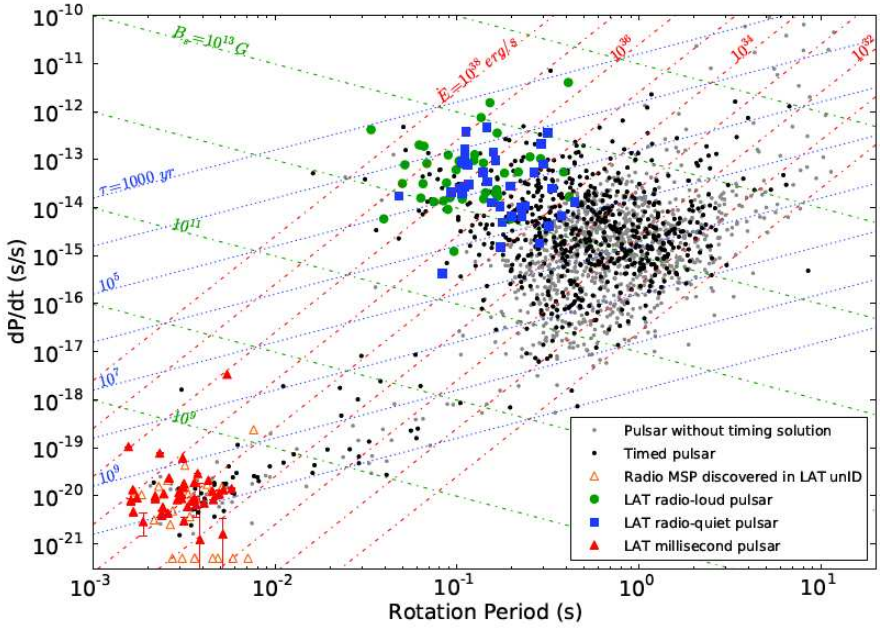

Figure 4: *Pulsar spindown rate $\dot{P}$ versus the rotation period P. Green dots indicate the 42 ordinary "radio-loud" gamma-ray pulsars, and blue squares show the 35 ordinary "radio-quiet" pulsars. Red triangles indicate the 40 millisecond gamma-ray pulsars. The 710 black dots indicate pulsars phase-folded in gamma-rays using rotation models provided by the "Pulsar Timing Consortium" for which no significant pulsations were observed. Orange open triangles indicate radio MSPs discovered at the positions of previously unassociated LAT sources. For clarity, error bars are shown only for the gamma-detected pulsars.*
Image taken from Abdo et al., 2013[8].

important information about their distance and galactic distribution (§4.3).

The 117 pulsars are divided into three groups: MSPs, ordinary radio-loud pulsars, and ordinary radio-quiet pulsars (see Figure 4 and Table 2).
We define a pulsar as "radio-loud" if the 1400 MHz flux density (§4.3.4) is $S_{1400} > 30$ μJy, and "radio-quiet" if $S_{1400} < 30$ μJy (or if no radio detection has been achieved). The smaller radio beaming fractions leave a large number of radio-quiet pulsars that can only be discovered in high-energy data.
Radio-loud pulsars represent 55% (42/77) of the ordinary pulsars contained in 2PC. Because the sensitivity for blind searches is lower than for simple folding, the parent population must contain substantially more radio-quiet than radio-loud pulsars (to a given gamma-ray flux limit). By contrast, all known gamma-ray MSPs are radio-loud. Although this circumstance might seem to be just a result of the difficulty to perform blind searches for MSPs, an analysis first performed by Romani (2012[71]) showed that the lack of gamma-ray MSPs without detectable radio emission is not an artifact.

A striking change in the pulsar sample with respect to 1PC is the dramatic increase in the MSP fraction (34%, 40/117), even compared to the number of known radio MSPs.
No pulsed detection of a young spin-powered object in a massive binary has yet been made. With improved search techniques, such objects may appear in future LAT pulsar catalogs.
Compared with the ordinary radio-loud pulsars, MSPs are often detected: (1) at smaller distances because of their lower luminosities, and (2) at larger $|b|$ because of the much greater age of this population.

Table 2 summarizes the census of known gamma-ray pulsars of the 2PC catalog according to the radio flux S_{1400} (§4.3.4) and the method by which the pulsars were discovered (§4.2). Additional information about the catalog are available on the *Fermi Science Support Center* (FSSC) servers at http://fermi.gsfc.nasa.gov/ssc/data/access/lat/2nd_PSR_catalog/.

4.1 Gamma-ray pulsation detection

The main aim of a gamma-ray telescope observing neutron stars is to increase the number of photons detected for the search of pulsation in the gamma-ray band, and to reveal the gamma-ray emission from the numerous young and very energetic radio pulsars that were discovered after the completion of the CGRO mission.

Events recorded by the LAT have timestamps derived from GPS clocks integrated into a particular accurate subsystem (Abdo et al., 2009[3]), which provides the instantaneous spacecraft position with high accuracy.
Through these recorded events, it is possible to compute the pulsar rotational phases ϕ_i, using the standard pulsar timing code *TEMPO2* (Hobbs et al., 2006[39]) with the *fermi plug-in* (Ray et al., 2011[70]). This plug-in uses the recorded times and spacecraft positions combined with a pulsar timing ephemeris. The accuracy of the determined pulse phase is determined by the ephemeris.
In 2PC are retained pulsars with a $\geq 5\sigma$ confidence level detection of modulation in the phase histogram. Gamma-ray pulsar data from a gamma-ray telescope usually present a few photons detected whitin tens of thousands of pulsar rotations (§4.3.5). In these circumstances, the favored techniques are unbinned tests for periodic signals, such as the *H-test*, which is a statistical test for discarding the null hypothesis that a set of photon phases is uniformly distributed[13]. The sharpness of the peaks in the gamma-ray profile has a large impact on the detectability of pulsar; in particular, pulsars with narrow, sharp peaks are easier to detect than pulsars with broad peaks covering most of the pulse phase.

4.2 Gamma-ray pulsar discovery method

There are currently three main methods for the detection of a pulsed signal from gamma-ray pulsars: exploiting known rotational ephemerides from radio (or X-ray) observatories, blind periodicity searches in gamma-ray, and radio targeted searches.
In this subsection we briefly describe these methods.

4.2.1 Applying known rotation ephemerides to gamma-ray sources or sky regions

The first method mentioned above has provided 60 gamma-ray pulsars detections in 2PC (40 ordinary and 20 MSPs, see Table 2). It uses known rotational ephemerides from radio or X-ray observatories. The 2405 known RPPs (mostly from ATNF) have mostly been discovered by radio searches (and minimally X-ray searches), and they all represent candidate gamma-ray pulsars. Radio ephemerides are useful in order to provide a straightforward gamma-ray phase-folding: this folding can be performed both using data around the position of an unidentified gamma-ray source (in 3FGL), or with a piece of "gamma-ray sky" taken from the LAT data corresponding to the position of the considered radio pulsar (or X-ray pulsar). Phase-folding with a radio or X-ray ephemeris is the most sensitive way to find gamma-ray

[13] For further details about H-test, see de Jager et al. (1989)[27] and de Jager & Büsching (2010)[26].

pulsations, since no penalities are incurred for trials in position, P, $\dot{P}$, or other search parameters. Having a reliable ephemeris for as many known pulsars as possible is of critical importance to LAT science. Through this method, it is possible to find most of the gamma-ray counterparties of radio (or X-ray) pulsars.

In addition to the ephemeris, radio observations also provide the information necessary to measure the absolute phase alignment (after interstellar dispersion corrections) between the radio or X-ray and gamma-ray pulses, providing key information about the relative geometry of the different emission regions.

4.2.2 Blind periodicity searches

The second method of gamma-ray pulsars search (which resulted into 36 gamma-ray pulsars detections in 2PC, see Table 2) involves the detection of the rotational period in the LAT data through blind searches without the use of any radio/X-ray ephemeris. This kind of search (as well as radio searches, described in §4.2.3) begins with the definition of a target list of candidate pulsars. Some targets are sources known at other wavelengths that are suspected of harboring pulsars. These include SNRs, PWNe and other high-energy sources mostly located along the Galactic plane.
Generally, these sources have already been scrutinized in deep radio searches independent of FGST. Through these deep radio searches it is possible to determine the radio-loud (or radio-quiet) nature of the pulsars.

Blind searches for pulsars in gamma-rays are challenging due to the wide pulsar parameter ranges that must be searched and due to the sparseness of the data (a few photons per hour for the brightest sources). The very limited statistic results in very long integration times (months to years). This aspect makes the standard Fast Fourier Transform search techniques computationally prohibitive. New semi-coherent search techniques (Atwood et al., 2006[14]; Pletsch et al., 2012b[63]) have been extremely successful to discover gamma-ray pulsars with modest computational requirements.

The LAT blind search sensitivity depends on several pulsar parameters, such as the rotation frequency, the energy spectrum, the pulsed fraction and the accuracy of the ephemeris.

Overall, well over one hundred LAT sources have been subjected to blind period searches. Pulsars might have been missed for some reasons: (1) low pulsed fraction, (2) broad pulse profiles, (3) high levels of timing noise[14] or glitches[15], (4) being in an unknown binary system or very high backgrounds. In particular, gamma-ray pulsars usually show the phenomena of glitches and timing noise that worsen the timing solutions. Since pulsars observed by a gamma-ray telescope are subject to these irregularities, the ephemeris relative to a given epoch cannot be extrapolated for a period exceeding a few months: it is therefore necessary to perform regular radio observation of pulsars and to cover the full observation range of gamma-ray telescope.

For the LAT pulsars undetected in the radio band, or too faint for regular radio timing, the pulsar timing ephemeris is determined directly by the LAT data. Techniques for the pulse's ToA determination optimized for sparse photon data have been developed and applied to generate the timing models required for the profile analysis (Ray et al., 2011[70]). This timing provides much more precise pulsar positions than can be determined from the LAT event directions, which is important for multiwavelength counterpart searches.

[14] Timing noise is a stochastic irregularity in the period of pulse repetition. This irregularity is typical of the ordinary pulsars, younger ($\tau_c \lesssim 10^7$ – 10^8 yr) than the recycled pulsars ($\tau_c \gtrsim 10^8$ yr).

[15] A glitch indicates a sudden change in the rotational period of a pulsar. The cause of this phenomenon is still unclear, but it could be due to sudden changes on the pulsar surface and/or interior.

4.2.3 Radio pulsar discoveries leading to gamma-ray pulsations

In the third discovery method, unassociated LAT source positions are searched for radio pulsations. In 2PC, only 21 pulsars (1 ordinary and 20 MSPs, see Table 2) were discovered with this method[16]. When a new radio pulsar is positionally associated with a LAT source, it must be observed for a substantial period (typically from six months to one year or more) in order to determine a timing model that allows a gamma-ray periodicity search in the LAT data, through gamma-ray phase-folding described in section 4.2.1. The long observation times are used in order to collect a statistically significant number of gamma-ray photons while the analysis of the radio pulsar provides a very precise rotational ephemeris: these strategies allow to calculate the phase for each gamma-ray photons received. The radio pulsar searches are sensitive to binary systems with the application of techniques to correct for the orbital acceleration in short data sets (with durations much less than the binary period, Ransom et al., 2002[67]): this feature allows for the discovery of binary MSPs which are largely inaccessible to gamma-ray blind searches.

Radio searches of LAT sources are performed by the Fermi *Pulsar Search Consortium* (PSC)[17]. As the LAT Collaboration generates internal source lists and preliminary catalogs of gamma-ray sources from the accumulating sky-survey data, these target localizations are provided to the PSC for searching, with rankings on how strongly their characteristics resemble those of gamma-ray pulsars, as described in subsection 4.2.2. This technique was employed during the EGRET era as well, but with modest success, in part due to the relatively poor source localizations. With the LAT, there are many more gamma-ray sources detected and each one is localized to an accuracy that is comparable to, or smaller than, the beam width of the radio telescopes being used. This enables deep searches by removing the need to mosaic a large region, and also it facilitates repeated searches of the same source (Kerr et al., 2012[41]).
In particular, because the MSP population beyond the detection limit of LAT ($\sim$ 2 kpc) is distributed nearly uniformly across the sky, full sky surveys are required, whereas most young pulsar searches are concentrated on the Galactic plane (or targeted on Globular Clusters).

Interestingly, the success rate for radio searches of LAT sources in the plane has been much poorer. Only 4 ordinary pulsars have been discovered, and only one of those turned out to be a gamma-ray pulsar (PSR J2030+3641, Camilo et al., 2012[18]). This is probably due to a combination of ordinary pulsars having smaller radio beaming fractions than MSPs (as evidenced in Table 2 by the large number of ordinary, radio-quiet pulsars discovered) and the fact that the Galactic plane has been well surveyed for radio pulsars. The great success of the blind gamma searches in the plane is because ordinary pulsars mainly reside there.

Despite the limited success of LAT source discoveries in the Galactic plane through radio searches, in this project we insist on this kind of strategy because most of the pulsars are located in the plane. In order to perform this strategy, the method of detection of a pulsed signal from gamma-ray pulsars is similar to the one described in this subsection, with the difference that the radio search is performed in the gamma-ray error boxes of unidentified LAT sources, in order to discover pulsars, SNRs, PWNe, AGNs, or other astrophysical objects. This discovery method is essential for the observational strategy of exploring these gamma-ray error boxes at SRT (see §7).

[16] Actually at least 34 pulsars were discovered with this method when 2PC was already nearing completion.
[17] PSC (Ray et al., 2012[69]) is an international collaboration of radio observers with access to large radio telescopes.

Table 2: *Summary of the known gamma-ray pulsars of the 2PC catalog according to the radio flux measured at 1400 MHz S_{1400} (see §4 and §4.3.4) and the method by which the pulsars were discovered.*

Category	Type	Ephemeris	Blind	Gamma	Total
Ordinary	Radio-loud gamma-ray	39	2	1	42
	Radio-quiet gamma-ray	1	34	-	35
	Total	40	36	1	77
Millisecond	Radio-loud binary	11	-	17[a]	31
	Radio-loud isolated	9	-	-	9
	Total	20	-	20	40
Total 2PC		60	36	21	117

[a] The radio flux S_{1400} of two MSPs has not yet been measured (PSRs J1858-2216 and J2047+1053), and PSR J1514-4946 scintillates too much to obtain a good flux measurement.

Note – Columns 1 and 2 list the category and the type of pulsars; column 3 lists pulsars discoveried through the rotation ephemeris (§4.2.1); column 4 lists pulsars discoveried through the rotation ephemeris (§4.2.1); column 5 lists pulsars discoveried through the blind periodicity search (§4.2.2); column 6 lists radio pulsar discoveries leading to gamma-ray pulsations (§4.2.3); column 7 lists total amounts.

4.3 Gamma-ray pulsars

Pulsars have featured prominently in the gamma-ray sky since the birth of gamma-ray astronomy (§2.1). Important information about the characteristics of pulsars can be obtained through gamma-ray observations. The 2PC catalog captures much of this information (see §4).
The Crab (Kniffen et al., 1974[43]; Moran et al., 2013[53]) and the Vela (Thompson et al., 1975[84]; Zyuzin et al., 2013[89]) pulsars are the better studied young gamma-ray pulsars, since they have a very strong signal and emission observed at multiple frequencies.

The discovery strategies discussed in section 4.1 yielded 117 gamma-ray pulsars in three years of data. These pulsars represent the brightest galactic gamma-ray sources and the only ones currently identified with emission at energies above one GeV.
FGST has significantly increased the number of known energetic ordinary and millisecond pulsars. Pulsar discoveries continue as increased statistics bring light curves above the 5σ detection threshold; improved methods for event selection and blind searches allow increased sensitivity, and multiwavelength studies either detect radio pulsations or constrain the blind search space for likely pulsar candidates.

4.3.1 Luminosity and energy flux

The minimum energy flux necessary to detect gamma-ray pulses is not uniform in the sky because of the different levels of background (particularly near the galactic plane).
The total energy flux F_{tot} of a pulsar located at a distance d is defined by the relation ("Handbook of Pulsar Astronomy", Lorimer & Kramer, 2005[47]):

$$F_{tot} = \frac{\dot{E}_{rot}}{d^2} \tag{6}$$

An estimate of both $\dot{E}_{rot}$ and d is necessary in order to obtain a measure of F_{tot}.
The estimate of the distance d, which will be addressed in section 4.3.2, is very important because the dominant term in the uncertainty of F_{tot} is d^2, for almost all gamma-ray pulsars.
The estimate of $\dot{E}_{rot}$ involves, instead, the knowledge of P and $\dot{P}$ of the pulsar, which are derived from the results of the early stages of the timing procedure of sources. EGRET

results (Thompson, 2008[82]) as well as theoretical expectations indicated that ordinary pulsars with large spin-down luminosity $\dot{E} > 10^{34}$ erg s^{-1} are the most likely gamma-ray pulsar candidates. This aspect is confirmed by the fact that all gamma-ray pulsars of 2PC have $\dot{E} > 3 \times 10^{33}$ erg s^{-1}. Study of $\dot{E}_{rot}$ (such as Klesper et al., 2013[42]) suggests that most of gamma-ray pulsars should be associated to PWNe (see §3.4.3).

Generally, the associability of a gamma-ray source to a pulsar can be verified by comparing F_{tot} with the flux observed in the gamma-ray F_γ: if this comparison shows that $F_\gamma > F_{tot}$, then almost surely the source is not associable with a pulsar.
Gamma-ray emission models predict different relations between the spin-down luminosity $\dot{E}_{rot}$ and the gamma-ray luminosity L_γ, making this a discriminating observable when applied to a large sample of gamma-ray pulsars. The dependence of gamma-ray luminosity on spin-down luminosity is one of the most important results of 2PC.
L_γ is defined as:

$$L_\gamma = 4\pi d^2 f_\Omega G_{100} \text{ erg s}^{-1} \tag{7}$$

where f_Ω is the beam correction factor, and G_{100} is the energy flux in the 0.1 – 100 GeV energy band.

f_Ω describes the fraction of solid angle illuminated by the pulsar beam and it depends on the gamma-ray emission model used. In the past, the gamma-ray beam was conventionally assumed to sweep out 1 steradians solid angle, and then the relation 7 becomes $L_\gamma = d^2_{kpc} G_{100}$. Such a beam is appropriate to near-surface polar cap emission and corresponds to $f_\Omega = \frac{1}{4\pi} \sim 0.08$ (for example Thompson et al., 1994[83]). An outer magnetosphere fan-like beam sweeping the entire sky (4π steradians) gives $f_\Omega \sim 1$, which is the value adopted in 2PC for calculating L_γ. However, Pierbattista et al. (2012[62]) found a large spread in f_Ω values for different emission models and for radio-loud versus radio-quiet ordinary pulsars.

The energy flux G_{100} is obtained from equation 11 and the fits as:

$$G_{100} = \int_{100\ MeV}^{100\ GeV} E \frac{dN}{dE} dE \text{ erg cm}^{-2} \text{ s}^{-1} \tag{8}$$

In 2PC, G_{100} of the ordinary LAT-detected pulsars is in range $0.20 \cdot 10^{-11}$ – $9.06 \cdot 10^{-9}$ erg cm^{-2} s^{-1}, and in range $0.24 \cdot 10^{-11}$ – $0.11 \cdot 10^{-9}$ erg cm^{-2} s^{-1} for the MSPs.
In 3FGL, G_{100} of all firmly identified gamma-ray pulsars is in range $2.28 \cdot 10^{-12}$ – $8.93 \cdot 10^{-9}$ erg s^{-1} cm^{-2}.

It is possible to derive a "*heuristic*" gamma-ray pulsar luminosity L^h_γ through the emission properties of pulsars. Above the open field-line threshold voltage $V \simeq 3.18 \times 10^{-3}$ volts, gamma-ray emitting electron-positron cascades occur, and a linear dependence of L_γ on V would give $L_\gamma \propto \sqrt{\dot{E}}$ (Arons, 1996[11]) (lower diagonal line in Figure 5.
With an arbitrary normalization, L^h_γ is:

$$L^h_\gamma = \sqrt{10^{33} \dot{E}} \text{ erg s}^{-1} \tag{9}$$

At low $\dot{E}$ values L_γ seem to be falling below L^h_γ. The upper diagonal line in Figure 5 shows $L_\gamma = \dot{E}$, that is a 100% efficiency ε for converting spin-down luminosity into gamma-rays (see §4.3.3). A few pulsars appear above this line, likely due to over-estimated distances (see §4.3.2) or f_Ω values.
The relationship between $\dot{E}_{rot}$ and L_ν emitted at a specific range frequency ν is summarized in Table 3.

Table 3: *Relationship between $\dot{E}_{rot}$ and L_ν for different frequency ranges ν.*

Range	Relationship	Study
Radio	$L_r \propto \dot{E}_{rot}^{\frac{1}{3}}$	Arzoumanian et al., 2002[12]
Optic	$L_o \propto \dot{E}_{rot}^{1.6 \pm 0.2}$	Shearer e Golden, 2001[73]
Soft X	$L_{X,m} \propto \dot{E}_{rot}$	Becker e Trümper, 1997[15]
Hard X	$L_{X,d} \propto \dot{E}_{rot}^{1.5}$	Possenti et al., 2002[65]
γ	$L_\gamma \propto \dot{E}_{rot}^{0.5}$	Thompson, 2001[80]

4.3.2 Distances

The distance d to the source is necessary for converting the measured pulsar flux to emitted luminosity L_γ. A known distance also allows mapping neutron star distributions relative to the spiral arms of our Galaxy, or evaluating their scale height above the plane.
The distances of the LAT-detected ordinary pulsars are in the range 0.25 – 25.3 kpc, and in the range 0.16 – 7.6 kpc for the MSPs. These distances are consistent with the pulsar evolutionary scenario and location along the Galactic plane (Fryer, 1999[33]).
To estimate these distances, mainly three methods can be used; however, the methods vastly differ in reliability.

1. The most accurate distance estimator is the annual trigonometric parallax. Unfortunately, parallax can only be measured for relatively nearby pulsars, using X-ray or optical images, radio interferometric imaging technique, or accurate timing procedure. Obtaining pulsar parallaxes via relative astrometry yields distances that can be used to probe properties of the pulsar population and the ISM. Large programs are essential to obtain the sample sizes necessary for these population studies, but must be efficiently conducted to avoid requiring unfeasible large amounts of observing time. In this context, the PSRπ program uses a specific software in order to study an astrometric survey of 60 pulsars (Deller et al., 2011[30]; Deller, 2014[29]).

2. The *dispersion measure* DM is by far the most commonly used radio-loud pulsar distance estimator. Given a model for the electron density n_e in the various structures of our Galaxy, DM is the column density of free electrons along the path from Earth to the pulsar:
$$DM = \int_0^d n_e dl \tag{10}$$
DM is measured in units of pc cm^{-3}.
The electrons delay the radio pulse arrival by $\Delta t_{DM} = DM(p\nu^2)^{-1}$, where ν is the observing frequency (in MHz) and $p = 2.410 \times 10^{-4}$ MHz^{-2} pc cm^{-3} s^{-1}. Given a model for the electron density n_e (usually the *NE2001* model developed in 2002 by Cordes & Lazio[22]), the line integral of equation 10 yields the distance d for which DM matches the radio measurement.

3. Comparing the absorbing hydrogen column density N_H with the total hydrogen column density for that line of sight obtained from 21 cm radio surveys yields a rough distance estimate. The Doppler shift of neutral hydrogen (H I) absorption or emission lines measured from clouds on the our line of sight, together with a Galactic rotation

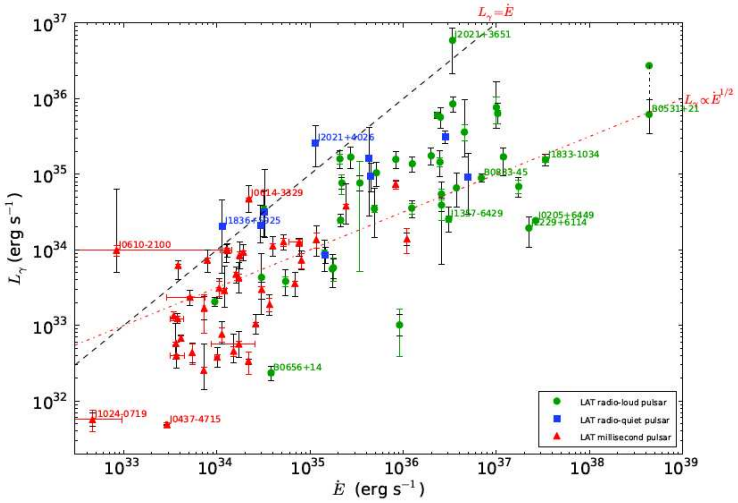

Figure 5: *Gamma-ray luminosity L_γ in the 0.1 – 100 GeV energy band versus spin-down luminosity $\dot{E}$. The vertical error bars due to the distance uncertainties are black. Doppler corrections (see §4.3.7) have been applied to MSPs with known proper motions, leading to visible horizontal error bars in some cases. The upper diagonal line indicates 100% conversion of spin-down luminosity into gamma-ray flux ($L_\gamma = \dot{E}$): for pulsars above this line, the distance d may be smaller, and/or the assumed beam correction $f_\Omega = 1$ is wrong. The lower diagonal line indicates the heuristic luminosity ($L_\gamma^h \propto \sqrt{\dot{E}}$), to guide the eye.*
Image taken from Abdo et al., 2013[8].

model, can give "kinematic" distances to the clouds. The pulsar distance is then constrained if there is evidence that the pulsar is in one of the clouds, or between some of them. Associations can be uncertain and these distance estimates can be controversial.

Pulsar distance cannot well be determined for the growing number of gamma-ray pulsars not detected at radio wavelengths, and thus without a DM, due to the difficulties of the other methods. Currently 2PC contains 26 objects with no distance estimates: to mitigate this, a maximum distance is determined by assuming that the pulsar is within our Galaxy. The Galaxy edge is defined as the distance for a given line of sight where the NE2001 DM reaches its maximum value.

4.3.3 Energy conversion efficiency

Pulsars emit in a wide range of the electromagnetic spectrum, but most of the total energy flux is released in the X and gamma-ray bands. This conclusion has been strengthened in recent years due to LAT that is contributing to a better understanding of pulsars energetics.

The amount of input radiation converted into emission at a given range of frequency ν is defined *emission efficiency* $\varepsilon = \frac{L_\nu}{\dot{E}_{rot}}$. From several studies, it is clear that (1) ε shows a large variation at different frequencies ν and (2) ε increases with frequency following a law of the type $\varepsilon \propto \nu^{0.17 \pm 0.10}$ (Figure 6). In the gamma-ray band, usually ε_γ is around 10%[47]. Moreover, Figure 5 shows a general trend: ordinary pulsars show increased efficiency to produce gamma-rays as the spin-down luminosity decreases toward $\dot{E} \sim 5 \times 10^{35}$ erg s^{-1}. This trend is in conflict with the model of Takata et al. (2010[77]) that predicts a much flatter trend at high $\dot{E}$. Above $\dot{E} \sim 5 \times 10^{35}$ erg s^{-1} MSPs show a similar trend but there is a wide range of efficiencies below this $\dot{E}$.

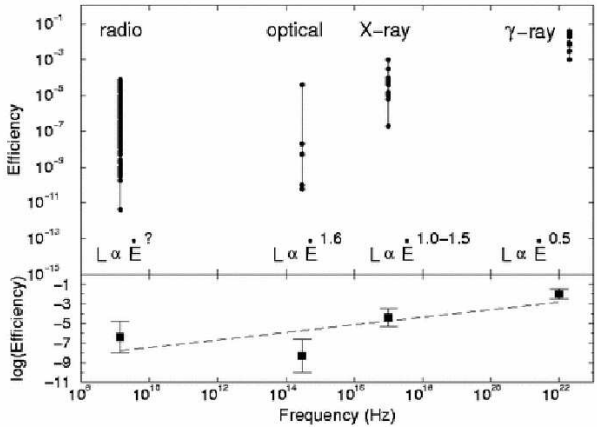

Figure 6: *(top) Efficiency ε derived for radio optical, X and gamma-ray frequencies; the $L \propto \dot{E}$ differs as indicated for each frequency band.*
(below) Fit of the average values of ε for each frequency band; this fit shows an increase of ε as frequency ν increases.
Image taken from "Handbook of Pulsar Astronomy" by Lorimer and Kramer, 2005[47].

Nevertheless, the high efficiencies are remarkable, meaning that gamma-rays trace the bulk energetics of the pulsar machine and implying that studies correlating this output with other observables provide excellent prospects for understanding pulsar magnetosphere physics. Some factors complicate such studies, particularly the difficulty of obtaining accurate pulsar distances (discussed in §4.3.2). Improvements to the distance determination are needed for reduce this large uncertainty.

4.3.4 Radio intensities

The 1400 MHz flux densities S_{1400} of the ordinary LAT-detected pulsars are in the range 0.003 – 1100 mJy, and in range 0.04 – 149 mJy for the MSPs. Whenever possible, in 2PC, S_{1400} is reported as given in the ATNF catalog. For radio-loud pulsars with no published value at 1400 MHz, S_{1400} is extrapolated from measurements at other frequencies, assuming $S_\nu \propto \nu^\alpha$, where α is the spectral index: for most pulsars α has not been measured and therefore they use an average value[18] $\langle\alpha\rangle = -1.7$.

Blind search pulsars that have been observed with LAT, but were not detected at radio frequencies, do not have a tabulated S_{1400}. In this case in 2PC an upper limit is defined as the sensitivity of the observation, given by the pulsar radiometer equation (equation 23 in §7) assuming a minimum signal-to-noise ratio of 5 for a detection and a pulse duty cycle δ of 10%[19]. All the 36 pulsars discovered in blind searches have been searched deeply for radio pulsations (Saz Parkinson et al., 2010[72]; Ray et al., 2012[69]), and only 4 have been detected (for example, Camilo et al., 2009[19]; Pletsch et al., 2012[63]).

4.3.5 Profile characterization

Although the emission efficiency in gamma-rays is greater than the efficiencies in the other bands of the electromagnetic spectrum (see §4.3.3 and Figure 6) and the gamma-ray emis-

[18] This value is a middle ground between $\alpha = -1.6$ from Lorimer et al. (1995[48]) and $\alpha = -1.8$ from Maron et al. (2000[50]).

[19] The pulse duty cycle is defined as the ratio between the effective pulse width W_{eq} (see §7.4) and the rotation period P.

sion is usually strongly pulsed and collimated, a gamma-ray pulsar emits very few detectable gamma-ray photons. This is due to the fact that the gamma-ray emission is released through highly energetic photons which are numerically inferior (about 13 orders of magnitude compared to radio photons) to those issued in the radio band. In this way then it is difficult to produce an integrated profile of the pulses through the procedures used in radio timing.

The 2PC catalog shows for each pulsar the gamma-ray pulse profiles at different energies, overlaid with the radio profiles when available.
The gamma-ray light curves (see §3.2) are computed as a weighted histogram of gamma-ray photons as a function of gamma-ray rotational phases ϕ. The number of bins in this histogram is choosen according to the weighted H-test (see §4.1). The background photons contribution is estimated from diffuse sources and neighboring point sources through the statistical calculation of the likelihood that the photon does not originate from the pulsar (for details, see Abdo et al., 2013[8]).

As we have seen in section 4.3.2, the propagation of radio pulses through the dispersive ISM is delayed by Δt_{DM}. This delay can be accounted for by TEMPO2, the software used to create the pulsar ephemerides, allowing precise alignment of radio and gamma-ray light curves.
The fiducial phase ($\phi = 0$) represents ideally the rotational phase when the magnetic axis, the spin axis, and the line of sight lie in the same plane. For some pulsars, this phase can be identified by fitting the rotating vector model (Radhakrishnan & Cooke 1969[66]) to radio polarization position angle versus phase.
In 2PC, if radio emission from the polar cap of radio-loud pulsars is symmetric, the peak intensity can also be used as a proxy for the fiducial phase. If radio emission from the polar cap is asymmetric, there are several case studies with which to associate the fiducial phase (for details, see Abdo et al., 2013[8]).

Additional clues to the pulsar beaming and detectability can be extracted from patterns in the radio and gamma-ray light curves. The majority of pulsars in 2PC show two peaks, P1 and P2: 75% (58/77) of the ordinary pulsars, and 60% (24/40) of the MSPs. Figure 7 shows a sample of four recurring profile shapes, classifiable according to the ratio R^i_{rf} of the half-widths of the rising and falling peak edges. Here, the index i indicates the first and second gamma-ray peaks following phase $\phi = 0$. In panel (a) of the Figure, the sharpest edges are the trailing edge of the first peak, $R^1_{rf} > 1$, and the leading edge of the second peak, $R^2_{rf} < 1$. In panel (d), it is the opposite: the "outer" peak edges are the most abrupt, $R^1_{rf} < 1$ and $R^2_{rf} > 1$. In panel (b), the leading edges are sharpest ($R^1_{rf} = R^2_{rf} < 1$) while for panel (c), the trailing edges are steep ($R^1_{rf} = R^2_{rf} > 1$). About half of the profiles are classifiable with good statistical significance and nearly all of these have sharp outer edges (see Figure 7d). This is the expected pattern for caustics from a hollow cone (Abdo et al., 2013[8]). A few pulsars depart significantly from this pattern, most prominently those for which both peaks fall sharply (see Figure 7c). These suggest emission from both poles (Abdo et al., 2013[8]). Many MSPs do not fit this simple scheme and cannot be classified in this way with any confidence.
More detailed analysis of the pulse width statistics may uncover other trends. One feature noted is that for pulsars with two strong caustic peaks, the P2/P1 ratio increases with energy.
Through the improvement of LAT statistics, it has been possible to show a third peak (P3) for 4 pulsars (2 ordinary pulsars and 2 MSPs). This is very important in order to study

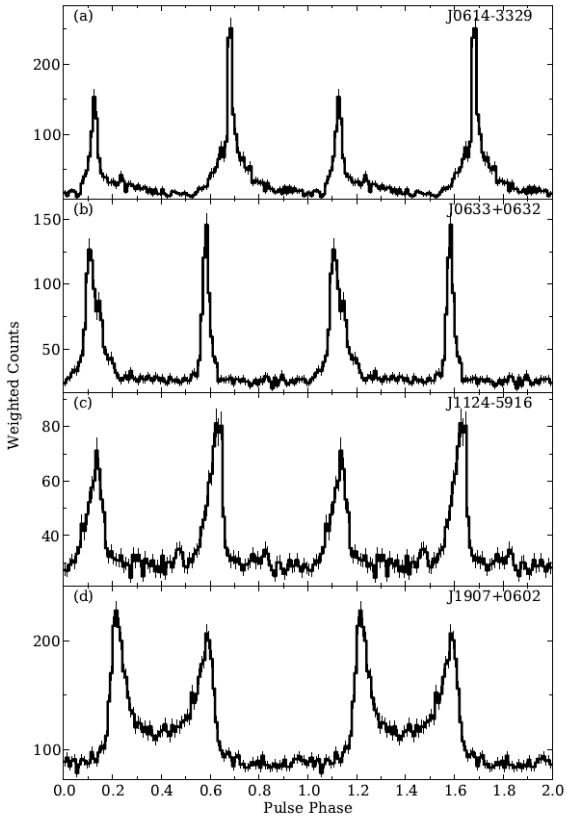

Figure 7: *Examples of four types of two-peak gamma-ray pulse profiles: (a) PSR J0614-3329, sharpest peak edge between the two peaks; (b) PSR J0633+0632, sharp leading edge for both peaks; (c) PSR J1124-5916, sharp trailing edge for both peaks; (d) PSR J1907+0602, "outside" peak edges are sharpest. Image taken from Abdo et al., 2013[8].*

better constraints on the origin of pulse components: to explain such a structure it is necessary to go beyond a simple geometrical approximation and to employ models with a full treatment of the radiation spectrum and its variation through the magnetosphere (for example, Du et al., 2011[31]; Wang et al., 2011[88]).

The majority of MSPs (27) have profiles that are very similar to those of ordinary pulsars, and the rest has very different profile types. In particular, a relatively large fraction (6) has phase-aligned radio and gamma-ray pulses. The peak alignment suggests that the radio as well as the gamma-ray pulses result from caustic emission at altitudes that are a large fraction of the light cylinder in the relatively small MSP magnetospheres (Venter et al., 2012[86]). The Crab pulsar, with sharp (caustic) main and inter-pulse radio components composed of "giant pulse" emission and aligned with the two gamma-ray pulses, likely represents a similar case.

The gamma-ray light curves in 2PC strongly suggest that the gamma-ray emission is distributed in a narrow gap bordering the closed field line boundary (Abdo et al., 2013). Although the light curves show a large degree of regularity, none of the currently proposed emission models alone is able to account for all of the observed properties.

4.3.6 Spectral analyses

Most models of pulsar gamma-ray emission predict that the spectrum in the LAT energy range should be dominated by curvature radiation, in the radiation-reaction limited regime (i.e., Muslimov & Harding, 2004[54]). This mechanism predicts that pulsar spectra should exponentially cut off near energies of a few GeV. The detection of pulsed emission above 100 GeV from the Crab suggests that, for some pulsars, either an additional component becomes dominant above the cutoff or a different mechanism, for example, inverse Compton scattering, may be responsible for the LAT emission.

The pulsed emission is concentrated in one or more narrow peaks. Depending on the viewing geometry and emission model, a pulsar can have a 100% duty cycle and significant magnetospheric emission can also exist away from the peaks.

In 2PC, the point-source detection significance and the spectral parameters for each LAT pulsar are evaluated through a spectral analysis similar to that performed for 3FGL (see §3).
The spectrum of each LAT pulsar was modeled, for the purposes of 2PC, as a power law with an exponential cutoff:

$$\frac{dN}{dE} = K\left(\frac{E}{E_0}\right)^{-\Gamma} exp\left(-\frac{E}{E_{cut}}\right)^{b} \text{ ph cm}^{-2}\,\text{GeV}^{-1}\,\text{s}^{-1} \tag{11}$$

The four parameters are the normalization factor (K), the photon index at low energy (Γ), the cutoff energy (E_{cut}), and a parameter representing the sharpness of the cutoff (b) which is fixed to 1 in the default fit. The energy E_0 at which K is defined is arbitrary: E_0 correspond to the 3FGL pivot energy when it exists and 1 GeV otherwise. In the likelihood analysis Γ is constrained to be between 0 and 5 and E_{cut} to be between 0.1 and 100 GeV.

4.3.7 Doppler corrections

Many pulsar characteristics depend on their *intrinsic* spin period P_{int} and their spin-down rate $\dot{P}_{int}$. The ***Doppler shift*** of the *observed* period is:

$$P = \left(1 + \frac{v_R}{c}\right) P_{int} \tag{12}$$

where v_R is the radial velocity of the pulsar along the unit vector $\boldsymbol{n}_{10}$ from the solar system. The Doppler correction to $\dot{P}$ is obtained by differentiating the equation 12 and separating the effects of the proper motion of system ($\dot{P}_{shk}$; Shklovskii, 1970[74]) from the acceleration due to Galactic rotation ($\dot{P}_{gal}$):

$$\dot{P}_{int} = \dot{P} - \dot{P}_{shk} - \dot{P}_{gal} \tag{13}$$

with

$$\dot{P}_{shk} = \frac{1}{c}\mu^2 dP = k\left(\frac{\mu}{mas \cdot yr^{-1}}\right)^2 \left(\frac{d}{kpc}\right)\left(\frac{P}{s}\right) \tag{14}$$

and

$$\dot{P}_{gal} = \frac{1}{c}\mathbf{n}_{10} \cdot (\mathbf{a}_1 - \mathbf{a}_0)P \tag{15}$$

where $k = 2.43 \times 10^{-21}$ for pulsar distance d and μ is the proper motion transverse to the line of sight. The Galactic potential model of Carlberg & Innanen (1987[20]) and Kuijken & Gilmore (1989[44]) provides the accelerations $\boldsymbol{a}_1$ of the pulsar and $\boldsymbol{a}_0$ of the Sun. Since the constant k is small, the corrections are negligible for the ordinary gamma-ray pulsars, which all have $\dot{P} > 10^{-16}$. However, for MSPs $\mu^2 d$ can be large enough that $\dot{P}_{int}$ differs noticeably from the observed $\dot{P}$ values and quantities derived from $\dot{P}$ will also be affected.

5 Detection of possible gamma-ray pulsars observable and identifiable with SRT

One of the scientific goals of FGST is a deeper study of the gamma-ray pulsars, both to improve the knowledge of the already known pulsars, and to discover new ones in order to increase the sample.
Since the unidentified sources in the 3FGL catalog are so many (1009), we should select a reasonable sample on which to focus further targeted searches: in this context, this technical note focuses on the exploration of about 20 gamma-ray unidentified sources to be observed with SRT, in order to search for radio counterparts and in particular for radio pulsations (§4.2.3).

Starting from the 3033 gamma-ray sources in the 3FGL catalog, the preliminary step was to choose the ones not yet identified or associated to known sources. This step leads to the reduction of the catalog to 1009 sources.
For these 1009 sources we performed six further selection steps, which are described below.

5.1 Step 1: observability at SRT site

The first step of selection involved the choice among these 1009 sources of those that can be observed at SRT latitude.
Through the knowledge of the geographical latitude of SRT ($lat_{SRT} = 39.4917°$), it is possible to calculate the minimum declination dec_{min} that a source should have in order to transit above the local horizon:

$$dec_{min} = lat_{SRT} - 90° = -50.5083° \tag{16}$$

Orographic limitations and radio frequency interference (RFI) phenomena[20] at SRT provide observational limitations equal to $lim_{orog} \sim 6°$ relative to the celestial horizon.
From the relation 16, it follows then that $dec_{min,SRT}$ corresponds to:

$$dec_{min,SRT} = dec_{min} + lim_{orog} \sim -44.5° \tag{17}$$

The observability of a source at SRT is related to his maximum elevation h_{trans} above the horizon (i.e. in transit elevation), defined by the relation:

$$h_{trans} = 90° - [lat_{SRT} - dec_s] \tag{18}$$

where dec_s is the declination of the source under consideration (with the sign).
We arbitrarily decided to put the minimum limit on transit in elevation $h_{trans,min} = 15°$, in order to observe the source above the horizon for a reasonable amount of time and reduce the RFI.
This step led to a further reduction of our sample to 663 sources.

[20] In radio astronomy, the Radio-Frequency Interference (RFI) is any source of transmission that is within the observed frequency band other than the celestial sources themselves. Because transmitters on and around the Earth can be many times stronger than the astronomical signal of interest, RFI is a major concern for performing radio astronomy. Natural sources of interference, such as lightning and the sun, are also often referred to as RFI.

Table 4: *Main features of the four first-light receivers of SRT.*

Band	ν_0 [GHz]	$\Delta\nu$ [GHz]	φ [arcsec]	T_{sys} [K]	G [K Jy^{-1}]
P	0.3575	0.08	3275.70	(65)	(0.53)
L	1.550	0.40	755.53	(21)	(0.55)
C	6.700	2.00	174.79	33	0.56
K	22.250	2.00 [a]	52.69	80	0.51
S [b]	(3.000)	(2.000)	(390.36)	(20)	(0.64)

[a] A wider $\Delta\nu$ (8 GHz) is presently under development.
[b] The S-band receiver is presently under development.

Note − Column 1 lists the observing band; column 2 lists the center observing radio frequency (ν_0, in GHz); column 3 lists the observing bandwidth ($\Delta\nu$, in GHz); column 4 lists the beam-size (φ, in arcsec); column 5 lists the system noise temperature (T_{sys}, in K); column 6 lists the antenna gain (G, in K Jy^{-1}).
G and T_{sys} are measured at 45 degree elevation: where they are not measured, their theoretical estimations are shown between brackets.

5.2 Step 2: selection of pointings

The second step of selection involved the choice among these 663 sources of all those that can be observed with a single pointing in L-band (Table 4) at SRT. This criterion was adopted mostly because typically, in the L-band, the physical characteristics of gamma-ray pulsars (i.e. the spectra) increase the detection probability of the gamma-ray pulsation with good observation time economy (see §7).

It is possible to estimate the number of pointings n_{punt} required by SRT to observe a given source as the ratio between the sky area S_γ (solid angle) defined by the error box of a gamma-ray source[21] and the area of the sky observed by SRT of radius r ($S_{\nu,SRT}$) in L-band in a single-dish pointing (beam Full Width Half Maximum, FWHM, of the antenna[22] φ).
$S_{\nu,SRT}$, measured in square degrees, can be estimated through the relation:

$$S_{\nu,SRT} = \pi \cdot r^2 = \pi \cdot \left(\frac{\varphi}{2}\right)^2 = 7.85 \cdot 10^{-1}\varphi^2 \text{ deg}^2 \tag{19}$$

where φ is the FWHM of the antenna, measured in degrees.
From S_γ and $S_{\nu,SRT}$ (relation 19), then n_{punt} is equal to:

$$n_{punt} = \frac{S_\gamma}{S_{\nu,SRT}} = \frac{\pi \cdot s_{min} \cdot s_{max}}{7.85 \cdot 10^{-1}\varphi^2} = 4\frac{s_{min} \cdot s_{max}}{\varphi^2} \tag{20}$$

By imposing $n_{punt} \leq 1$, this step led to a further reduction of the catalog previously generated to 336 sources.

5.3 Step 3: selection of positional source association

As a third selection step we checked whether known radio pulsar from the ATNF catalog are associated or not to gamma-ray error boxes. Usually this selection filter is necessary

[21] $S_\gamma = \pi \cdot s_{min} \cdot s_{max}$, where s_{min} and s_{max} are respectively the semi-minor and the semi-major axis of the error box of the gamma-ray source at 95% confidence, expressed in degrees.

[22] The FWHM of antenna beam is defined as $\varphi = 69.9\frac{\lambda}{D}$ deg, where λ is the wavelength of the incident radiation, and D is the diameter of the reflector ($D = 64$ m for SRT).

because the ATNF catalog is updated more frequently than a LAT-catalog, and then we secured that there are no further positional associations with pulsars in these gamma-ray error boxes. In this case the 3FGL catalog is relatively recent (January 2015), and so we expect very limited effects due to positional source associations.
To check if one (or more) pulsar of ATNF catalog is within the error box of each gamma-ray source of the sub-sample, we simply verified that $\mathcal{D}_{(b,l)} \leq s_{max}$, where $\mathcal{D}_{(b,l)}$ is the angular distance (in degrees) between each radio pulsar coordinates and each gamma-ray source present in the sub-sample.
$\mathcal{D}_{(b,l)}$ is defined by the relation:

$$\mathcal{D}_{(b,l)} = \frac{180}{\pi} \arccos \varsigma \tag{21}$$

where ς is the angular aperture (in radians) between the centers of the two "positions" in question[23].
As expected, this case has led to a very small reduction of the sub-sample previously generated (336 sources) to 333 sources.

5.4 Step 4: variability selection filter

Since the 143 firmly identified pulsars in the 3FGL catalog show a variability index (§3.2) between $\mathcal{V}_{min} = 20.01$ and $\mathcal{V}_{max} = 157.713$, it is expected that the flux variability of newly discovered pulsars should also lie in this range[24]. Therefore, the fourth step of selection involved the choice of those with $\mathcal{V}$ within that range among these 333 sources.
This step led to a modest reduction of our sample to 330 sources.

5.5 Step 5: flux selection filter

Since the 143 firmly identified pulsars in the 3FGL catalog have fluxes between $G_{100,min} = 2.28 \cdot 10^{-12}$ erg s^{-1} cm^{-2} and $G_{100,max} = 8.93 \cdot 10^{-9}$ erg s^{-1} cm^{-2} (§4.3.1), it is expected that also the fluxes of newly discovered pulsars should lie in this range.
This flux check led to a modest reduction of the sub-sample previously generated (330 sources) to 326 sources. This sample of 326 sources is shown in Appendix A, where we also report the number of SRT pointings required to cover the error box in P, L, C and K bands.

[23] ς is obtainable through the relation $\varsigma = \sin b_{ATNF} \cdot \sin b_{\gamma} + \cos b_{ATNF} \cdot \cos b_{\gamma} \cdot \cos(l_{ATNF} - l_{\gamma})$, where b and l are respectively the galactic latitude and longitude of source in question.

[24] In this reasoning we have not considered the high variability of the Crab pulsar ($PSRJ0534 + 2200$, $\mathcal{V}_{max} = 621.93$), since it is only a feature of the 3FGL automatic analysis and is in no way a real detection of variability in the Crab pulsar (see §3.6 of the paper by Acero et al., 2015[79]).

Table 5: *Sample of 22 gamma-ray sources potentially observable by SRT for the search of new radio and/or gamma-ray pulsars, sorted by energy flux* G_{100}.

Gamma-ray source	ra [deg]	dec [deg]	s_{max} [deg]	s_{min} [deg]	l [deg]	b [deg]	G_{100} [a]	$signif_{avg}$ [b]	$\mathcal{V}$	Γ	$n_{punt\,P}$	$n_{punt\,L}$	$n_{punt\,C}$	$n_{punt\,K}$	h_{trans} [deg]
3FGL J1848.4-0141	282.11	-1.69	0.08	0.05	31.088	-0.11	1.14	18.67	52.63	2.58	0.022	0.41	7.84	86.2	48.8
3FGL J1839.3-0552	279.84	-5.88	0.03	0.02	26.327	-0.01	1.00	14.91	37.43	2.54	0.004	0.08	1.63	17.9	44.6
3FGL J1906.6+0720	286.67	7.333	0.03	0.02	41.192	-0.02	0.99	26.27	41.70	2.35	0.004	0.09	1.69	18.6	57.8
3FGL J1852.8+0158	283.20	1.972	0.06	0.05	34.847	0.587	0.82	13.71	54.51	2.54	0.016	0.31	5.91	65.0	52.4
3FGL J1857.9+0210	284.49	2.170	0.06	0.05	35.607	-0.46	0.68	15.18	50.61	2.59	0.016	0.31	5.87	64.6	52.6
3FGL J2017.9+3627	304.48	36.45	0.03	0.03	74.541	0.410	0.65	25.03	39.85	2.61	0.005	0.09	1.85	20.4	86.9
3FGL J1850.5-0024	282.63	-0.40	0.05	0.04	32.468	0.017	0.57	9.435	64.26	2.41	0.011	0.21	4.03	44.4	50.1
3FGL J1857.2+0059	284.31	0.986	0.04	0.03	34.471	-0.84	0.48	12.39	57.13	2.26	0.007	0.13	2.56	28.2	51.4
3FGL J1919.9+1407	289.98	14.11	0.07	0.06	48.710	0.241	0.46	10.87	67.72	2.69	0.023	0.43	8.14	89.5	64.6
3FGL J2004.4+3338	301.10	33.64	0.03	0.03	70.671	1.185	0.43	18.46	50.29	2.29	0.005	0.10	1.98	21.8	84.1
3FGL J0223.6+6204	35.906	62.08	0.03	0.03	133.49	1.115	0.39	12.87	41.77	2.80	0.006	0.12	2.36	25.9	67.4
3FGL J2038.4+4212	309.62	42.20	0.05	0.05	81.527	0.542	0.39	11.75	45.66	2.69	0.015	0.28	5.34	58.8	87.2
3FGL J1857.9+0355	284.48	3.927	0.07	0.06	37.170	0.342	0.37	9.268	55.58	2.68	0.022	0.41	7.78	85.6	54.4
3FGL J1901.5-0126	285.39	-1.44	0.05	0.05	32.801	-2.92	0.36	13.97	60.36	2.61	0.014	0.27	5.04	55.5	49.0
3FGL J1849.5-0124c	282.39	-1.41	0.07	0.06	31.463	-0.23	0.34	4.902	36.74	2.28	0.024	0.46	8.60	94.7	49.0
3FGL J1653.6-0158	253.41	-1.98	0.03	0.03	16.618	24.92	0.33	31.94	55.40	2.06	0.005	0.11	2.07	22.7	48.5
3FGL J2041.1+4736	310.28	47.60	0.05	0.04	86.091	3.461	0.31	18.37	56.27	2.13	0.011	0.22	4.16	45.8	81.8
3FGL J1827.6-0846	276.90	-8.77	0.05	0.04	22.418	1.241	0.30	8.678	51.62	2.36	0.012	0.23	4.32	47.6	41.7
3FGL J1838.9-0646	279.72	-6.77	0.07	0.05	25.477	-0.31	0.29	7.123	50.15	1.92	0.022	0.41	7.80	85.9	43.7
3FGL J1844.3-0344	281.10	-3.74	0.05	0.04	28.795	-0.14	0.28	10.06	44.78	2.28	0.012	0.23	4.45	49.0	46.7
3FGL J1837.6-0717	279.40	-7.29	0.08	0.05	24.866	-0.26	0.26	5.551	41.26	2.03	0.023	0.44	8.40	92.4	43.2
3FGL J2034.4+3833c	308.62	38.56	0.05	0.05	78.158	-1.04	0.26	8.889	55.76	2.52	0.013	0.24	4.65	51.1	89.0

[a] In units of 10^{-10} erg s^{-1} cm^{-2}.

[b] The number of σ of detection is approximately associated with the square root of $signif_{avg}$.

Note − Column 1 lists the name of gamma-ray source; columns 2 and 3 list the right ascension and the declination of the gamma-ray source (ra and dec); columns 4 and 5 list the semi-major and the semi-minor axis of the error box (elliptical in shape) at 95% confidence (s_{max} and s_{min}); columns 6 and 7 list the galactic longitude and the galactic latitude (l and b); column 8 lists the energy flux in range 0.1 – 100 GeV (G_{100}); column 9 lists the significance of the detection of the gamma-ray source ($signif_{avg}$); column 10 lists the variability ($\mathcal{V}$); column 11 lists the photon spectral index (Γ); columns 12, 13, 14 and 15 list the number of pointings practicable by SRT ($n_{punt\,P}$, $n_{punt\,L}$, $n_{punt\,C}$ and $n_{punt\,K}$) respectively in P-band ($\nu_0 = 0.3575$ GHz), L-band ($\nu_0 = 1.55$ GHz), C-band ($\nu_0 = 6.7$ GHz) and K-band ($\nu_0 = 22.25$ GHz); finally column 16 lists the maximum elevation of the gamma-ray source (h_{trans}).
The designator "c" to the names of the sources indicates *flags* (§3.4.5) and therefore these sources can be considered as potentially confused with interstellar emission. Their position, emission characteristics, or even existence may not be reliable.

Table 6: *Sample of 22 gamma-ray sources potentially observable by SRT for the search of new radio and/or gamma-ray pulsars, sorted by right ascension ra.*

Gamma-ray source	ra [deg]	dec [deg]	s_{max} [deg]	s_{min} [deg]	l [deg]	b [deg]	G_{100} [a]	$signif_{avg}$ [b]	$\mathcal{V}$	Γ	$n_{punt\,P}$	$n_{punt\,L}$	$n_{punt\,C}$	$n_{punt\,K}$	h_{trans} [deg]
3FGL J0223.6+6204	35.906	62.08	0.03	0.03	133.49	1.115	0.39	12.87	41.77	2.80	0.006	0.12	2.36	25.9	67.4
3FGL J1653.6-0158	253.41	-1.98	0.03	0.03	16.618	24.92	0.33	31.94	55.40	2.06	0.005	0.11	2.07	22.7	48.5
3FGL J1827.6-0846	276.90	-8.77	0.05	0.04	22.418	1.241	0.30	8.678	51.62	2.36	0.012	0.23	4.32	47.6	41.7
3FGL J1837.6-0717	279.40	-7.29	0.08	0.05	24.866	-0.26	0.26	5.551	41.26	2.03	0.023	0.44	8.40	92.4	43.2
3FGL J1838.9-0646	279.72	-6.77	0.07	0.05	25.477	-0.31	0.29	7.123	50.15	1.92	0.022	0.41	7.80	85.9	43.7
3FGL J1839.3-0552	279.84	-5.88	0.03	0.02	26.327	-0.01	1.00	14.91	37.43	2.54	0.004	0.08	1.63	17.9	44.6
3FGL J1844.3-0344	281.10	-3.74	0.05	0.04	28.795	-0.14	0.28	10.06	44.78	2.28	0.012	0.23	4.45	49.0	46.7
3FGL J1848.4-0141	282.11	-1.69	0.08	0.05	31.088	-0.11	1.14	18.67	52.63	2.58	0.022	0.41	7.84	86.2	48.8
3FGL J1849.5-0124c	282.39	-1.41	0.07	0.06	31.463	-0.23	0.34	4.902	36.74	2.28	0.024	0.46	8.60	94.7	49.0
3FGL J1850.5-0024	282.63	-0.40	0.05	0.04	32.468	0.017	0.57	9.435	64.26	2.41	0.011	0.21	4.03	44.4	50.1
3FGL J1852.8+0158	283.20	1.972	0.06	0.05	34.847	0.587	0.82	13.71	54.51	2.54	0.016	0.31	5.91	65.0	52.4
3FGL J1857.2+0059	284.31	0.986	0.04	0.03	34.471	-0.84	0.48	12.39	57.13	2.26	0.007	0.13	2.56	28.2	51.4
3FGL J1857.9+0355	284.48	3.927	0.07	0.06	37.170	0.342	0.37	9.268	55.58	2.68	0.022	0.41	7.78	85.6	54.4
3FGL J1857.9+0210	284.49	2.170	0.06	0.05	35.607	-0.46	0.68	15.18	50.61	2.59	0.016	0.31	5.87	64.6	52.6
3FGL J1901.5-0126	285.39	-1.44	0.05	0.05	32.801	-2.92	0.36	13.97	60.36	2.61	0.014	0.27	5.04	55.5	49.0
3FGL J1906.6+0720	286.67	7.333	0.03	0.02	41.192	-0.02	0.99	26.27	41.70	2.35	0.004	0.09	1.69	18.6	57.8
3FGL J1919.9+1407	289.98	14.11	0.07	0.06	48.710	0.241	0.46	10.87	67.72	2.69	0.023	0.43	8.14	89.5	64.6
3FGL J2004.4+3338	301.10	33.64	0.03	0.03	70.671	1.185	0.43	18.46	50.29	2.29	0.005	0.10	1.98	21.8	84.1
3FGL J2017.9+3627	304.48	36.45	0.03	0.03	74.541	0.410	0.65	25.03	39.85	2.61	0.005	0.09	1.85	20.4	86.9
3FGL J2034.4+3833c	308.62	38.56	0.05	0.05	78.158	-1.04	0.26	8.889	55.76	2.52	0.013	0.24	4.65	51.1	89.0
3FGL J2038.4+4212	309.62	42.20	0.05	0.05	81.527	0.542	0.39	11.75	45.66	2.69	0.015	0.28	5.34	58.8	87.2
3FGL J2041.1+4736	310.28	47.60	0.05	0.04	86.091	3.461	0.31	18.37	56.27	2.13	0.011	0.22	4.16	45.8	81.8

[a] In units of 10^{-10} erg s^{-1} cm^{-2}.

[b] The number of σ of detection is approximately associated with the square root of $signif_{avg}$.

Note − Column 1 lists the name of gamma-ray source; columns 2 and 3 list the right ascension and the declination of the gamma-ray source (ra and dec); columns 4 and 5 list the semi-major and the semi-minor axis of the error box (elliptical in shape) at 95% confidence (s_{max} and s_{min}); columns 6 and 7 list the galactic longitude and the galactic latitude (l and b); column 8 lists the energy flux in range 0.1 – 100 GeV (G_{100}); column 9 lists the significance of the detection of the gamma-ray source ($signif_{avg}$); column 10 lists the variability ($\mathcal{V}$); column 11 lists the photon spectral index (Γ); columns 12, 13, 14 and 15 list the number of pointings practicable by SRT ($n_{punt\,P}$, $n_{punt\,L}$, $n_{punt\,C}$ and $n_{punt\,K}$) respectively in P-band ($\nu_0 = 0.3575$ GHz), L-band ($\nu_0 = 1.55$ GHz), C-band ($\nu_0 = 6.7$ GHz) and K-band ($\nu_0 = 22.25$ GHz); finally column 16 lists the maximum elevation of the gamma-ray source (h_{trans}).
The designator "c" to the names of the sources indicates *flags* (§3.4.5) and therefore these sources can be considered as potentially confused with interstellar emission. Their position, emission characteristics, or even existence may not be reliable.

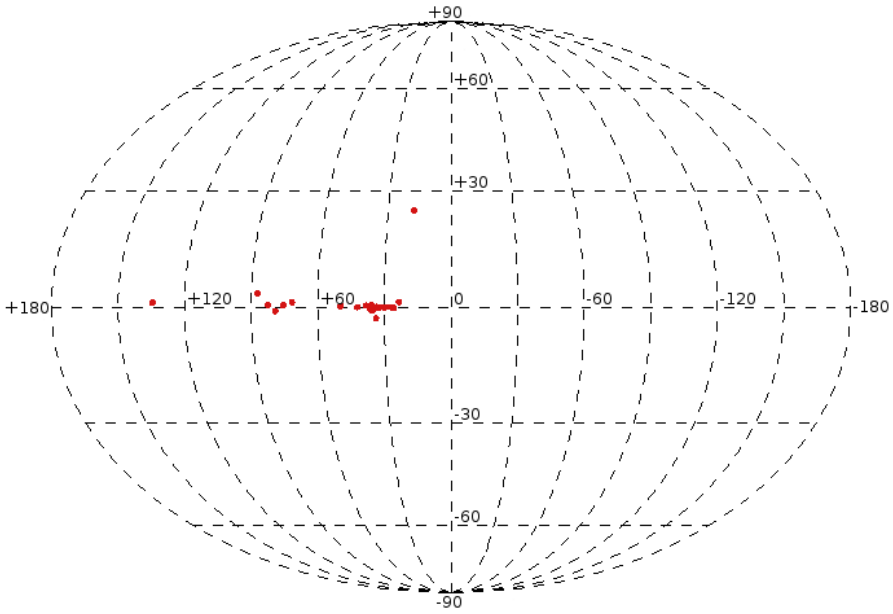

Figure 8: *Galactic map of the 22 gamma-ray sources, selected as good gamma-ray pulsar candidates. The X-axis shows the galactic longitude l, while the Y-axis shows the galactic latitude b.*

5.6 Step 6: selection of 22 gamma-ray sources

The sixth and final step of selection involved the choice, among these 326 sources, of an arbitrary initial sample of about 20 gamma-ray sources with high energy flux G_{100}, highly ranked for our quest. This sample can represent the starting point for a possible multi-frequency observation campaign with SRT.
This sample is obtained by imposing more stringent conditions on our catalog:

- requiring that the sources can be observed at SRT also in C-band (Table 4) with an arbitrary number of pointings[25] not exceeding $n_{punt\,C} = 10$ (relation 20);
- having a minimum elevation $h_{trans,min}$ more stringent ($\geq 40°$), in order to observe the source above the horizon with SRT for more time.

The 22 gamma-ray sources thus selected, shown in Figure 8 and listed in Table 5 (sorted in energy flux G_{100}), are the starting point for a campaign of investigation at SRT for the multi-frequency search of new gamma-ray pulsars. In this table we also report the number of pointings in principle required in K-band at SRT (Table 4).

Table 6 represents the same sources, sorted in right ascension ra, more practical for SRT, because the ra of a celestial body at the local meridian corresponds to the LST-time coordinate system (§6).

This campaign of investigation will take place according to the procedures described in sections 4.2.3 and 7.

[25] We chose $n_{punt\,C} = 10$ pointings in order to be able to cover a significant number of targets at the SRT within a reasonable observing time (a typical filler slot of ≤ 1 h).

6 Visibility of the 22 sources at SRT

An important practical tool for the observation with SRT of these 22 gamma-ray sources is the plot of visibility of the sources (Figure 9), obtained by CASTIA (Vacca, Iacolina et al., 2013[85]). CASTIA is a software package that can check the visibility of radio sources at a certain date at SRT (http://www.ira.inaf.it/Observing/castia/site/index.php). This software package produces a graph containing the visibility of radio sources as a function of time. In this plot, the following symbols are displayed to indicate the observing conditions:

- a yellow line when the source rises and/or sunsets;
- a green line when the source reaches 6° elevation[26];
- a red line when the source exceeds 85° elevation[27];
- a star when the source is in transit, that is when the source is located in the maximum elevation point h_{trans};
- a pink/white dashed-line is overlaid for targets nearby the Sun/Moon.

In the x-axis of the graph shown in Figure 9 there are two kinds of time coordinate systems (adopted in Astrophysics):

- on the top the *Local Sidereal Time* (LST), namely the hour angle between the vernal equinox and the local meridian taken counterclockwise; LST corresponds to the right ascension (ra) of celestial bodies at the local meridian and provides an idea of the distance between the source and the local meridian of SRT;
- on the bottom the *Coordinated Universal Time* (UTC), namely the solar time coordinate referred to the prime meridian (Greenwich).

From Figure 9 we can see that as many as 15 out of 22 sources are visible at almost the same LST (culminating between 18:00 and 19:00) and, in particular, the source $3FGLJ0223.6+6204$ is visible for the whole day. In general, the sources are visible at different UTC times in different seasons of the year, but they cover a not very broad LST and UTC range (on average about 10 hours).

7 SRT observation strategy

The practical implementation of this technical note requires an observational strategy that involves the following sequence of procedures:

- test activities on well known gamma-ray/radio pulsar associations;
- selection of targets to investigate and their visibility;
- study of the pointing strategy for each target and choice of the receivers to use;

[26] This elevation corresponds to the orographic limit at SRT lim_{orog} (see §5.1).

[27] When a source exceeds the elevation of $\sim 85°$, a radio telescope cannot follow it, because together with the motion in elevation it should make a very fast movement in azimuth, that is often incompatible with the mechanics.

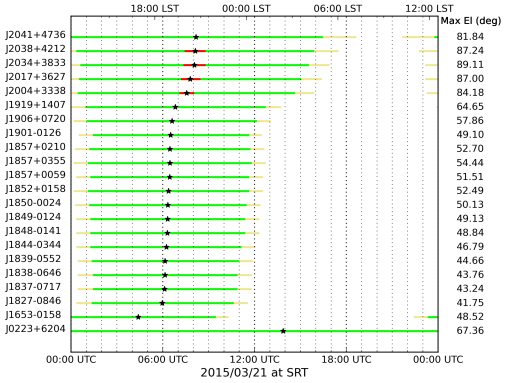

(a) Plot of visibility at 21 March 2015.

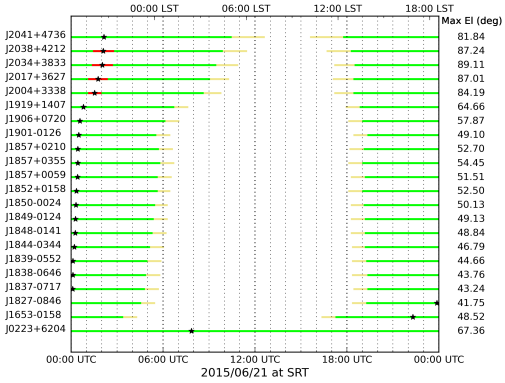

(b) Plot of visibility at 21 June 2015.

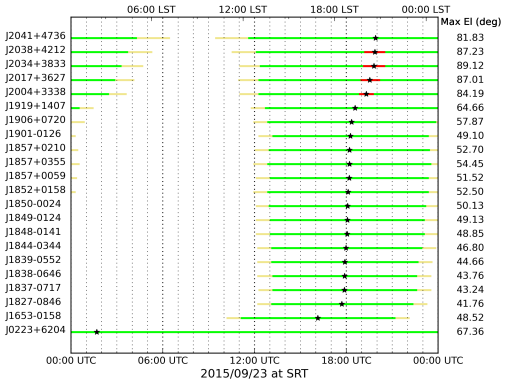

(c) Plot of visibility at 23 Semptember 2015.

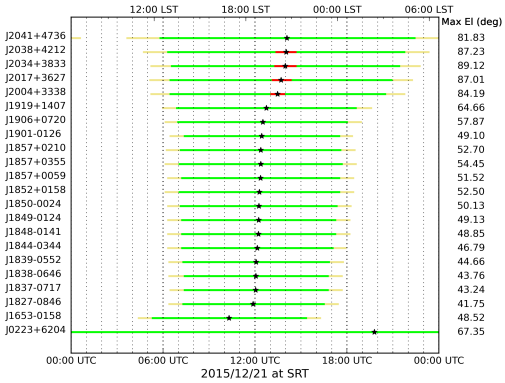

(d) Plot of visibility at 21 December 2015.

Figure 9: *Plot of visibility of 22 gamma-ray sources in SRT site at (a) 21 March 2015, (b) 21 June 2015, (c) 23 Semptember 2015, (d) 21 December 2015.*

- setting the parameters for the back-end;
- study of the integration times of each pointing;
- observation schedule.

These procedures are described below in depth.

7.1 SRT test activities

This procedure is necessary in order to verify the actual performance of the pulsar back-end for SRT. The back-end is the part of the line system that gets the signal emitted by a target source from the receiver and processes it. The test activity consists of the observation of a gamma-ray source (or more) that perfectly simulates the aim of this technical note. This means looking for a gamma-ray pulsar (or more than one) discovered through radio observations of unidentified gamma-ray sources, and visible to SRT.
For this purpose we opted for the pulsars J2302+4442 (Cognard et al., 2011[21]) and J1544+4937 (Bhattacharyya et al., 2013[16]): the first was discovered at the Nancay Radio Telescope (NRT) in L-band (1400 MHz), it has a spin period of $P = 5.19$ ms and a radio flux $S_{1400} = 1.2$ mJy; the latter was discovered at the Giant Metrewave Radio Telescope (GMRT) in P-band (607 MHz), it has a spin period of $P = 2.16$ ms and a radio flux $S_{1400} = 0.18$ mJy. From the visibility plot (Figure 10), we note that these pulsars are visible to SRT throughout the day.

Their radio fluxes allow us to implement the observations at SRT with a reasonable observing time Δt for this project (less than one hour), namely $\Delta t = 5.75$ s for J2302+4442 and $\Delta t = 393.73$ s (about 7 minutes) for J1544+4937, at extrapolated L-band (for details about Δt see the subsection 7.4).

In particular, for these sources we will perform a blind radio search in order to find the "test pulsar". The blind search is one of the two main operating modes currently implemented in the Pulsar Digital Filter Bank (P-DFB), the back-end system used for this work. The back-end setting necessary to use the P-DFB in "search mode" will be described in section 7.3.

7.2 Study of the pointing uncertainties for each target

The selection of which targets to investigate has been discussed in section 5, and the study of the pointings for each target has been discussed in subsection 5.2.
Moreover, the number of pointings indicated in Tables 5 and 6 allow us to implement the observations in the P-band, L-band and C-band. In order to organize an optimal observation strategy with SRT, it is necessary to know both the number of pointings (with the associated uncertainty) and the observing time for these sources (for each pointing).
In this subsection we focus on the analysis of the pointing uncertainties, whereas in the next subsection (§7.4) we focus on the study of the observing times.

From the equation (20), through the error propagation law, we define the pointing uncertainty Δn_{punt}:

$$\Delta n_{punt} = n_{punt}\sqrt{\left(\frac{\Delta s_{max}}{s_{max}}\right)^2 + \left(\frac{\Delta s_{min}}{s_{min}}\right)^2 + 2\left(\frac{\Delta\varphi}{\varphi}\right)^2} \tag{22}$$

where n_{punt} is the number of pointings required by SRT in order to observe a gamma-ray source contained in 3FGL, Δs_{min} and Δs_{max} are respectively the uncertainties on the

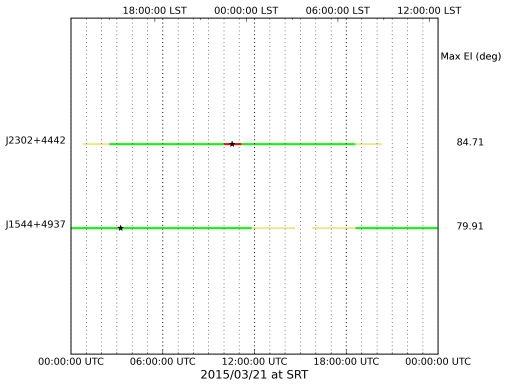

(a) Plot of visibility at 21 March 2015.

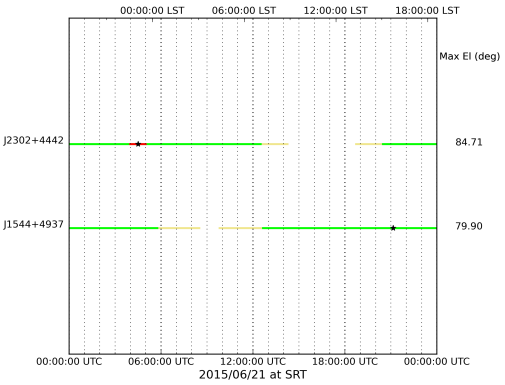

(b) Plot of visibility at 21 June 2015.

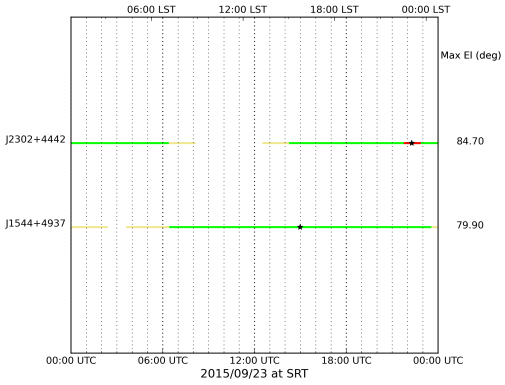

(c) Plot of visibility at 23 Semptember 2015.

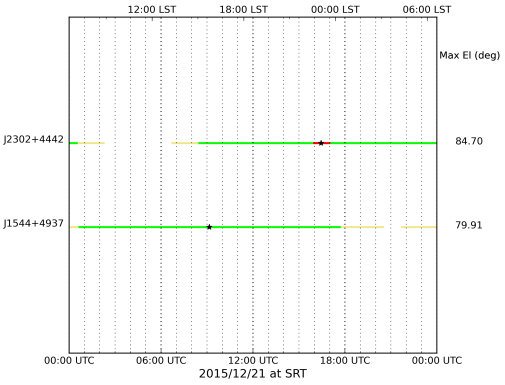

(d) Plot of visibility at 21 December 2015.

Figure 10: *Plot of visibility of pulsars J2302+4442 and J1544+4937 in SRT site at (a) 21 March 2015, (b) 21 June 2015, (c) 23 Semptember 2015 and (d) 21 December 2015.*

measures of s_{min} and s_{max}, and $\Delta\varphi$ is the uncertainty on the measure of φ.
We assume approximately that $\Delta s_{min} = \Delta s_{max} \sim 0.0625^{\circ}$ (Nolan et al., 2012[55])[28], and $\frac{\Delta\varphi}{\varphi} \sim 10\%$.

In particular, $\Delta\varphi$ is determined by the antenna control servosystem accuracy, sistematic errors (misalignement of mechanical and electromagnetic parts) and non sistematic errors (wind pressure, thermal gradients).

From the results shown in Table 7, through the application of the equation 22, we note that Δn_{punt} is in some cases large enough to increase the value of n_{punt} above the prescription limits ($n_{punt\,P,max} = n_{punt\,L,max} = 1$ and $n_{punt\,C,max} = 10$).
In particular we observe that in P-band Δn_{punt} does not influence the observations, in L-band Δn_{punt} influences marginally the observations (82% of the sources in Table 7 is within the limit of $n_{punt\,L,max} = 1$), whereas in C-band Δn_{punt} influences strongly the observations (the number of pointings increased by a factor 2). Now we study the integration times of observations in order to see if the overall number of pointings are compatible with observations no longer than about one hour.

[28] The uncertainties on the measures of s_{min} and s_{max} are approximated to the spatial resolution of the model of the gamma-ray sky (see §3.1 of this note and §2.2 of the paper by Nolan et al., 2012[55]).
In particular, the residual TS map used for source detection (see §3.1) also allows optimizations of the likelihood with respect to the position of each gamma-ray source. The positional uncertainty for each gamma-ray source was estimated by examining the shape of the log likelihood function, fitting the distribution to the expected quadratic form in the angular deviations from the best-fit position. A measure of the quality of this fit is the mean square deviation of the log likelihood with respect to the fit on a circle of radius corresponding to two standard deviations (for further details see §3.1.4 of the paper by Nolan et al., 2012[55]).
A more complete (but more difficult) approach of this uncertainty takes into account the spectral-shape of the gamma-ray source (for further details see Appendix A of the paper by Nolan et al., 2012[55]).

Table 7: *Sample of 22 gamma-ray sources potentially observable by SRT for the search of new radio and/or gamma-ray pulsars, sorted by energy flux* G_{100}.

Gamma-ray source	ra [deg]	dec [deg]	s_{max} [deg]	s_{min} [deg]	l [deg]	b [deg]	G_{100} [a]	$n_{punt\,P}$	$\Delta n_{punt\,P}$	$n_{punt\,L}$	$\Delta n_{punt\,L}$	$n_{punt\,C}$	$\Delta n_{punt\,C}$
3FGL J1848.4-0141	282.11	-1.69	0.080	0.057	31.088	-0.11	1.14	0.022	0.030	0.41	0.565	7.84	10.55
3FGL J1839.3-0552	279.84	-5.88	0.034	0.028	26.327	-0.01	1.00	0.004	0.013	0.08	0.251	1.63	4.698
3FGL J1906.6+0720	286.67	7.333	0.037	0.027	41.192	-0.02	0.99	0.004	0.013	0.09	0.260	1.69	4.863
3FGL J1852.8+0158	283.20	1.972	0.062	0.055	34.847	0.587	0.82	0.016	0.025	0.31	0.477	5.91	8.927
3FGL J1857.9+0210	284.49	2.170	0.060	0.057	35.607	-0.46	0.68	0.016	0.025	0.31	0.474	5.87	8.867
3FGL J2017.9+3627	304.48	36.45	0.034	0.031	74.541	0.410	0.65	0.005	0.014	0.09	0.266	1.85	4.975
3FGL J1850.5-0024	282.63	-0.40	0.054	0.043	32.468	0.017	0.57	0.011	0.021	0.21	0.397	4.03	7.432
3FGL J1857.2+0059	284.31	0.986	0.042	0.035	34.471	-0.84	0.48	0.007	0.016	0.13	0.315	2.56	5.889
3FGL J1919.9+1407	289.98	14.11	0.077	0.061	48.710	0.241	0.46	0.023	0.030	0.43	0.566	8.14	10.58
3FGL J2004.4+3338	301.10	33.64	0.035	0.033	70.671	1.185	0.43	0.005	0.014	0.10	0.275	1.98	5.138
3FGL J0223.6+6204	35.906	62.08	0.039	0.035	133.49	1.115	0.39	0.006	0.015	0.12	0.300	2.36	5.617
3FGL J2038.4+4212	309.62	42.20	0.058	0.053	81.527	0.542	0.39	0.015	0.024	0.28	0.453	5.34	8.472
3FGL J1857.9+0355	284.48	3.927	0.071	0.063	37.170	0.342	0.37	0.022	0.029	0.41	0.548	7.78	10.25
3FGL J1901.5-0126	285.39	-1.44	0.055	0.053	32.801	-2.92	0.36	0.014	0.023	0.27	0.439	5.04	8.215
3FGL J1849.5-0124c	282.39	-1.41	0.076	0.066	31.463	-0.23	0.34	0.024	0.030	0.46	0.578	8.60	10.80
3FGL J1653.6-0158	253.41	-1.98	0.035	0.034	16.618	24.92	0.33	0.005	0.014	0.11	0.281	2.07	5.251
3FGL J2041.1+4736	310.28	47.60	0.050	0.048	86.091	3.461	0.31	0.011	0.021	0.22	0.399	4.16	7.455
3FGL J1827.6-0846	276.90	-8.77	0.053	0.047	22.418	1.241	0.30	0.012	0.021	0.23	0.408	4.32	7.627
3FGL J1838.9-0646	279.72	-6.77	0.078	0.059	25.477	-0.31	0.29	0.022	0.029	0.41	0.558	7.80	10.43
3FGL J1844.3-0344	281.10	-3.74	0.056	0.046	28.795	-0.14	0.28	0.012	0.022	0.23	0.416	4.45	7.786
3FGL J1837.6-0717	279.40	-7.29	0.086	0.057	24.866	-0.26	0.26	0.023	0.031	0.44	0.591	8.40	11.05
3FGL J2034.4+3833c	308.62	38.56	0.052	0.051	78.158	-1.04	0.26	0.013	0.022	0.24	0.421	4.65	7.879

[a] In units of 10^{-10} erg s^{-1} cm^{-2}.

[b] The number of σ of detection is approximately associated with the square root of $signif_{avg}$.

Note − Column 1 lists the name of gamma-ray source; columns 2 and 3 list the right ascension and the declination of the gamma-ray source (ra and dec); columns 4 and 5 list the semi-major and the semi-minor axis of the error box (elliptical in shape) at 95% confidence (s_{max} and s_{min}); columns 6 and 7 list the galactic longitude and the galactic latitude (l and b); column 8 lists the energy flux in range 0.1 – 100 GeV (G_{100}); columns 9 and 10 list the number of pointings practicable by SRT in P-band (ν_0 = 0.3575 GHz) and its uncertainties ($n_{punt\,P}$, $\Delta n_{punt\,P}$); columns 11 and 12 list the number of pointings practicable by SRT in L-band (ν_0 = 1.55 GHz) and its uncertainties ($n_{punt\,L}$, $\Delta n_{punt\,L}$); columns 13 and 14 list the number of pointings practicable by SRT in C-band (ν_0 = 6.7 GHz) and its uncertainties ($n_{punt\,C}$, $\Delta n_{punt\,C}$).
The designator "c" to the names of the sources indicates *flags* (§3.4.5) and therefore these sources can be considered as potentially confused with interstellar emission. Their position, emission characteristics, or even existence may not be reliable.

7.3 SRT pulsar back-end setting

In order to properly process the signal we will employ the *Pulsar Digital Filter Bank* (P-DFB) back-end. This system, developed by the ATNF (Australia Telescope National Facility), was installed at SRT in 2012. Currently two of the four operating modes[29] have been implemented: *folding mode* and *search mode*. For the purposes of this technical note, we are concerned with the P-DFB in search mode.

The commands related to the control of the antenna are executed through the Nuraghe software. This control software at the current development stage allows us to control all the devices of the telescope (e.g. the antenna mount, the receivers and some back-end) and to perform single-dish observations in the most common modes[30]. When the SEADAS software will be ready (Corongiu[23][24][25], 2014), data acquisition will be automated.

The P-DFB is able to process up to 1 GHz of bandwidth, $\Delta\nu$. Because of the interstellar dispersion's effects on pulsar observations, the observed bandwidth is divided into several narrow channels, n_{chan}. The observer can choose the bandwidth and the number of frequency channels according to some determined configurations (see Table 8). The current status of the P-DFB allows the observer to use only a single-band receiver at a time[31].
The P-DFB back-end is inserted inside a specific box. Several warning lights are visible on the front of the P-DFB. One of the most important is the temperature alert, since the P-DFB suffers from overheating when the running configuration is too computationally demanding (usually for bandwidths larger than 512 MHz). If this light is red, the data acquisition must be stopped for at least 10 minutes. During an observation, the temperature of the P-DFB must remain below $\sim 70°C$[32].

Before observing a target source in search mode, it is necessary to check the values of the P-DFB temperature and attenuations through a fake observation on a default source[33] using the "folding mode". Once these values stabilize in an appropriate range, it is possible to start the observations with the P-DFB in search mode.
In order to observe a target with the P-DFB in search mode at L-band, it is necessary to set in the associated graphical interface the correct parameters and information about the observation types (the main values are listed in Table 8). Currently the setting of parameters is done manually and it has to be performed in a specific sequence in order to correctly complete an observation using the P-DFB in both folding and search modes. The system is then ready to observe.

During the observation it is important to check the P-DFB temperature. The bandpass of the P-DFB and the data flow (frequency domain plots or a selection of a range of frequency channels) is verifiable, in real time, through the SPD (Spectra Display for ATNF correlators) graphic display. If the pulsar is not visible in the data, some strong RFI might be corrupting the data and hiding the signal even of strong pulsars. To remove RFI in both time and frequency domains, it is necessary to use the *pazi* tool from the psrchive software (http://psrchive.sourceforge.net/manuals/pazi/)[34].

[29] Baseband and spectrometer modes will be implemented later.
[30] For further details see http://www.srt.inaf.it/project/antenna-control-software/ and Orlati et al., 2012[56].
[31] It will later be possible to observe in parallel with the L and P-band receivers.
[32] It is a good idea to choose a lower threshold for the temperatures (e.g. $67°C$), in order to enable a better cooling down of the P-DFB. For an observation in folding mode the temperature can be checked through the graphical interface, while for a search mode observation it can be checked in the display on front of the instrument.
[33] The default source is the "23ms", a dummy pulsar to check that the P-DFB levels are correct.
[34] This operation can be done in real time.

Table 8: *Main parameters required in the P-DFB graphical interface in order to use the P-DFB in search mode in P-band, L-band and C-band. The source coordinates are inserted as hh : mm : ss.sss (for ra) and +/ − dd.mm.ss.sss (for dec).*

Band	Pulsar type	ν [MHz]	$\Delta\nu$ [MHz]
P	all	384	256
L	recycled[(a)]	1804	1024
	ordinary or recycled[(b)]	1548	512
C	all	7312	1024

[a] millisecond pulsars with $DM > 50$ (blind search at low latitudes or timing of binaries with poorly known ephemeris).
[b] millisecond pulsars with $DM < 50$.

Note − Column 1 and 2 list the observing band and the pulsar type; columns 3 and 4 list the central observing radio frequency (ν_0, in MHz) and the observing bandwidth ($\Delta\nu$, in MHz).
In general, C-band is used for the observation of magnetars, using the largest bandwidth (1024 MHz).
P-band is of great interest for the simultaneous observations with L-band, in order to determine the DM with precision. At present, it is not possible with the current state of the P-DFB.
For details, see the P-DFB manual (Egron et al., 2015[32]).

Once the observation is completed, the data are stored in a file with extension $.sf$ for search mode observation.

For further details and informations about the P-DFB and its user manual, it is strongly recommended to see the P-DFB manual (Egron et al., 2015[32]).

7.4 Study of the radio fluxes, integration times and choice of receivers to use

An accurate study of the unidentified gamma-ray sources (using the method described in the section 4.2.1) requires adequate observation times, Δt. Therefore, in the radio band (and not only) it is important to have a good synergy between the instrumental apparatus (e.g. the receiver or the back-end to use) and its parameters.
In this sense, we can proceed through two possible approaches:

1. studying how long (and how) unidentified gamma-ray sources can be observed at SRT for each pointing with a typical filler slot no longer than about one hour ($\Delta t = 3600$ s), in terms of the typical radio flux densities S_{1400} (see §4.3.4) of the gamma-ray pulsars contained in 2PC (S_{1400} is in the range 0.003 – 1100 mJy) and of the usable receivers;

2. studying the integration times Δt required in order to detect unidentified gamma-ray sources with radio flux densities typical of the gamma-ray pulsars contained in 2PC (S_{1400} is in the range 0.003 – 1100 mJy).

With regard to the first approach, it is useful to know the radio flux density S; a good estimate of this flux density S_{min}, detectable by a specific receiver, can be estimated from the radiometer equation (see e.g., "Handbook of Pulsar Astronomy" by Lorimer & Kramer, 2005[47]):

$$S_{min} = \beta \frac{\sigma(T_{sys} + T_{sky})}{G\sqrt{n_p \Delta t \Delta\nu}} \sqrt{\frac{W_e}{P - W_e}} \text{ Jy} \qquad (23)$$

where S_{min} is the flux density corresponding to a pulse signal-to-noise ratio threshold σ, T_{sys} is the system noise temperature (in K), T_{sky} is the sky background temperature[35] (in K), G is the telescope gain (in $K \cdot Jy^{-1}$), n_p is the number of polarizations, Δt is the integration time (in s), $\Delta\nu$ is the observing bandwidth (in Hz), P is the rotational period of the pulsar, and β is a correction factor (~ 1.2) due to the system imperfections (such as digitization of the signal). W_e is the effective pulse width that depends by the contributions of the intrinsic width W_i (expressed in seconds), by the propagations in the ISM (dispersion and scattering) and by the instrument time resolution:

$$W_e = \sqrt{W_i^2 + (\beta\delta t_{sampl})^2 + \delta t_{DM}^2 + \delta t_{scatt}^2} \tag{24}$$

where $\delta t_{DM} = 8.3 \cdot 10^3 DM \frac{\Delta\nu_{MHz}}{n_{chan} \cdot \nu_{MHz}^3}$ is the smearing of the pulse in a single channel due to the dispersion[36], $\delta t_{scatt} \propto \nu^{-4.4}$ is the smearing of the pulse due to the scattering[37] and δt_{sampl} is the sampling time of the signal from the receiver[38].
We studied S_{min} with $\Delta t = 3600$ seconds for each pointing and with respect to both the pulsar types (ordinary and recycled) and the position with respect to the Galactic plane. In particular, we used the radiometer equation (relation 23) with $\alpha = -1.7$ and $\sigma = 5$, with a pulse duty-cycle δ of 10% for ordinary pulsars (with $P = 2$ s and $DM = 50$ pc cm^{-3}) and a pulse duty-cycle δ of 30% for millisecond pulsars (with with $P = 2$ ms and $DM = 100$ pc cm^{-3}), with $n_p = 2$ and a sampling time $\delta t_{sampl} = 50$ μs; we also used a sky temperature T_{sky} (at 408 MHz) of 7 K (for pulsars outside the galactic plane), of 26 K (for pulsars in the galactic plane), and of 125 K (for pulsars near the center of the galactic plane), according to a study by Ransom (Ransom et al., 2011[68]).
Knowing that S_{min} depends on the observing frequency of each radio receiver according to the relation $S \propto \nu^{\alpha}$ (§4.3.4), we have obtained the minimum radio flux S_{min}, for each receiver of SRT. In particular, among these values the minimum detectable radio flux is in C-band for ordinary pulsars outside the Galactic plane (Table 9). This result is expected because T_{sky} is inversely proportional to the distance from the center of our Galaxy.

With regard to the second approach, if S_{min} is known, through the radiometer equation (23) we obtain an estimate of the integration time Δt:

$$\Delta t = \frac{\beta^2\sigma^2(T_{sys} + T_{sky})^2}{S_{min}^2 G^2 n_p \Delta\nu} \left(\frac{W_e}{P - W_e}\right) \text{ s} \tag{25}$$

In particular, we estimated the maximum integration time Δt, for each pointing, with respect to both the pulsar type and the position relative to the Galactic plane.
For this estimate, we choose a radio flux $S_{1400_{min}}$ threshold that must be measurable with SRT through an acceptable integration time (no longer than about one hour). Among the 78 gamma-ray pulsars of radio-loud type listed in the 2PC catalog (see Table 2), the minimum detected flux density is $S_{1400_{min}} = 0.04$ mJy (J1124-3653; Hessels et al., 2011[37]). This flux density measured at GBT has characteristics not compatible with SRT: this would imply very long observation time (Δt much greater than one hour) with SRT. For this reason, we

[35] T_{sky} is often given by the code "tt408", at 408 MHz, and it scales as $T_{sky} \propto \nu^{-2.7}$ (Lawson et al., 1987[45]).

[36] δt_{DM} is inversely proportional (at the same DM and $\frac{\Delta\nu_{MHz}}{n_{chan}}$ for single channel) to ν^3 and therefore we expect smaller corrections for C-band and, especially, for K-band.

[37] The value of δt_{scatt} is often given by the code "ne2001".

[38] The sampling time δt_{sampl} is the rate at which data are sampled in the acquisition system (back-end, see §7.3).

Table 9: *Values, for each pointing, of the minimum detectable radio flux S_{min} (with $\Delta t = 3600$ s), and the integration time Δt (with $S_{1400,min} = 0.15$ mJy) at SRT according to the pulsar type and its position with respect to the Galactic plane.*
We recall that S scales as $S \propto \nu^{\alpha}$ (with $\alpha = -1.7$), therefore at SRT $S_{1400,min} = 0.15$ mJy becomes $S_{P,min} = 1.527$ mJy, $S_{L,min} = 0.126$ mJy, $S_{C,min} = 0.011$ mJy, $S_{K,min} = 0.001$ mJy.

Type	Band	Plane		Out		Centre	
		S_{min} [mJy]	Δt [s]	S_{min} [mJy]	Δt [s]	S_{min} [mJy]	Δt [s]
Ordinary	P	0.51846	$4.14820 \cdot 10^2$	0.37294	$2.14630 \cdot 10^2$	1.21186	$2.26636 \cdot 10^3$
	L	0.04651	$4.89309 \cdot 10^2$	0.04541	$4.66271 \cdot 10^2$	0.05229	$6.18334 \cdot 10^2$
	C	0.03107	$3.16699 \cdot 10^4$	0.03106	$3.16508 \cdot 10^4$	0.03112	$3.17692 \cdot 10^4$
	K	0.08268	$1.32724 \cdot 10^7$	0.08267	$1.32723 \cdot 10^7$	0.08268	$1.32731 \cdot 10^7$
Millisecond	P	2.93314	$1.32767 \cdot 10^4$	2.05458	$6.51430 \cdot 10^3$	8.45917	$1.10428 \cdot 10^5$
	L	0.09236	$1.92916 \cdot 10^3$	0.09016	$1.83833 \cdot 10^3$	0.10382	$2.43786 \cdot 10^3$
	C	0.06124	$1.23034 \cdot 10^5$	0.06122	$1.22960 \cdot 10^5$	0.06133	$1.23421 \cdot 10^5$
	K	0.16295	$5.15591 \cdot 10^7$	0.16295	$5.15586 \cdot 10^7$	0.16295	$5.15617 \cdot 10^7$

Note – Column 1 and 2 list the pulsar type the observing band; columns 3 and 4 list S_{min} and Δt for pulsars in the Galactic plane; columns 5 and 6 list S_{min} and Δt for pulsars outside the Galactic plane; columns 7 and 8 list S_{min} and Δt for pulsars near the center of the Galactic plane.

decided to choose a higher threshold, obtainable through measurements with radio telescopes with features at least similar to SRT. Therefore, the chosen value is $S_{1400_{min}} = 0.15$ mJy, compatible with the available integration time to SRT (no longer than about one hour). In the 2PC catalog, the 65% (76/117) of gamma-ray pulsars has $S_{1400_{min}} = 0.15$ mJy.
Using the values for the estimation of $S_{1400_{min}}$ (see above), we obtained the maximum integration time Δt, for each receiver of SRT and for each pointing. Observing Table 9, and compatibly with our purposes and the time available for SRT and with the pointings (in particular with Δn_{punt}, studied in subsection 7.2), we conclude that in the near future we will be able to study with SRT gamma-ray sources at L-band. In particular, we will study those sources in which we can find, with good probability, ordinary pulsars. For millisecond pulsars, the overall observing time is longer than one hour (but not exceeding 2 hours).
Furthermore, it would be very important to observe also in the C-band (where some bright pulsar could be discovered), because (1) the effects of the interstellar medium are reduced, (2) very few radio telescopes have tried to look these and (3) these frequencies are better suited for eventual studies with imaging techniques. Unfortunately, this observation would require integration times much longer than one hour ($\Delta t \sim 9$ hours for each pointing).
Many gamma-ray sources could be studied with each receiver at SRT, but these should be associated to radio pulsars with a flat spectrum ($\alpha \sim 0$).

8 Conclusions

The purpose of this technical note is to propose and plan SRT observations for the identification of a sample of about 20 previously unidentified gamma-ray sources (Table 5). These sources could potentially be associated and identified with pulsars through radio observations (see §4.2.3). This multi-frequency research activity will constitute an important SRT test, and later one of the first observational strategies of type "targeted search" implemented with this radio telescope.

The candidate pulsars have been selected among all the unidentified gamma-ray sources

and with certain characteristics listed in the 3FGL catalog (§3), following a specific selection strategy (§5).
We considered a $\geq 5\sigma$ confidence level detection of new pulsars, and we choose a radio flux threshold of $S_{1400} = 0.15$ mJy, detectable at SRT through a reasonable integration time, no longer than about one hour. Using S_{1400}, we obtained the required integration time Δt, for each receiver of SRT and standard back-end configuration: an optimal value of Δt, compatible both with our purposes, and the time available for SRT and the pointings (in particular with Δn_{punt}, §7.2), is found in the L-band principally for those gamma-ray sources in which we can find, with good probability, ordinary pulsars (see Table 9). Therefore these observational campaigns with SRT can be performed almost completely with only one pointing in L-band, with limited observing times. For the millisecond pulsars, the observational campaigns with SRT would be longer, but shorter than one hour.
Furthermore, it would also be very important to observe also in the C-band, but this would require campaigns of "pulsar targeted search" at SRT site with integration times much longer than one hour ($\Delta t \sim 9$ hours for each pointing). Many gamma-ray sources could be studied with each receiver at SRT, but these should be associated with radio pulsars with a flat spectrum.

21 out of the 22 selectted sources are in the Galactic plane in the range of $-10^\circ \leq b \leq 10^\circ$, as can be seen from the Figure 8. This means that these 21 sources could potentially be associated and identified with ordinary gamma-ray pulsars.
The remaining source is located at $b >| 10^\circ |$, where 40.8% of gamma-ray pulsars[39] (73/179) in the 3FGL catalog were discovered. This aspect leads to the conclusion that this gamma-ray source may be more probably associated and identified with "recycled" gamma-ray pulsar, according to the evolutionary scenario of pulsars (Fryer, 1999[33]).

[39]These gamma-ray pulsars may be quite close ($d \lesssim 1$ kpc), because generally an astrophysical object appears close to a higher galactic latitude.

References

[1] A. A. Abdo, M. Ackermann, M. Ajello, A. Allafort, E. Antolini, and et al. Fermi Large Area Telescope First Source Catalog. *ApJS*, 188:405–436, jun 2010.

[2] A. A. Abdo, M. Ackermann, M. Ajello, A. Allafort, L. Baldini, and et al. Fermi Large Area Telescope Observations of the Vela-X Pulsar Wind Nebula. *ApJ*, 713:146–153, apr 2010.

[3] A. A. Abdo, M. Ackermann, M. Ajello, J. Ampe, B. Anderson, and et al. The on-orbit calibration of the Fermi Large Area Telescope. *Astropart. Phys.*, 32:193–219, oct 2009.

[4] A. A. Abdo, M. Ackermann, M. Ajello, W. B. Atwood, M. Axelsson, and et al. Fermi Large Area Telescope Observations of the Crab Pulsar And Nebula. *ApJ*, 708:1254–1267, jan 2010.

[5] A. A. Abdo, M. Ackermann, M. Ajello, W. B. Atwood, M. Axelsson, and et al. The First Fermi Large Area Telescope Catalog of Gamma-ray Pulsars. *ApJS*, 187:460–494, apr 2010.

[6] A. A. Abdo, M. Ackermann, M. Ajello, L. Baldini, J. Ballet, and et al. Radio-Loud Narrow-Line Seyfert 1 as a New Class of Gamma-Ray Active Galactic Nuclei. *ApJ*, 707:L142–L147, dec 2009.

[7] A. A. Abdo, M. Ackermann, M. Ajello, L. Baldini, J. Ballet, and et al. Fermi-LAT Study of Gamma-ray Emission in the Direction of Supernova Remnant W49B. *ApJ*, 722:1303–1311, oct 2010.

[8] A. A. Abdo, M. Ajello, A. Allafort, L. Baldini, J. Ballet, and et al. The Second Fermi Large Area Telescope Catalog of Gamma-Ray Pulsars. *ApJS*, 208:17, oct 2013.

[9] M. Ackermann, M. Ajello, A. Allafort, E. Antolini, W. B. Atwood, and et al. The Second Catalog of Active Galactic Nuclei Detected by the Fermi Large Area Telescope. *ApJ*, 743:171, dec 2011.

[10] M. Ackermann, M. Ajello, W. Atwood, L. Baldini, J. Ballet, and et al. The Third Catalog of Active Galactic Nuclei Detected by the Fermi Large Area Telescope. *ArXiv e-prints*, 1501.06054, jan 2015.

[11] J. Arons. Pulsars as gamma ray sources. *A&AS*, 120:C49, nov 1996.

[12] Z. Arzoumanian, D. F. Chernoff, and J. M. Cordes. The Velocity Distribution of Isolated Radio Pulsars. *ApJ*, 568:289–301, mar 2002.

[13] W. B. Atwood, A. A. Abdo, M. Ackermann, W. Althouse, B. Anderson, and et al. The Large Area Telescope on the Fermi Gamma-Ray Space Telescope Mission. *ApJ*, 697:1071–1102, jun 2009.

[14] W. B. Atwood, M. Ziegler, R. P. Johnson, and B. M. Baughman. A Time-differencing Technique for Detecting Radio-quiet Gamma-Ray Pulsars. *ApJ*, 652:L49–L52, nov 2006.

[15] W. Becker and J. Truemper. The X-ray luminosity of rotation-powered neutron stars. *A&A*, 326:682–691, oct 1997.

[16] B. Bhattacharyya, J. Roy, P. S. Ray, Y. Gupta, D. Bhattacharya, and et al. GMRT Discovery of PSR J1544+4937: An Eclipsing Black-widow Pulsar Identified with a Fermi-LAT Source. *ApJ*, 773:L12, aug 2013.

[17] S. Bogdanov and J. P. Halpern. Identification of the High-Energy Gamma-Ray Source 3FGL J1544.6-1125 as a Transitional Millisecond Pulsar Binary in an Accreting State. *ArXiv e-prints*, mar 2015.

[18] F. Camilo, M. Kerr, P. S. Ray, S. M. Ransom, S. Johnston, and et al. PSR J2030+3641: Radio Discovery and Gamma-Ray Study of a Middle-aged Pulsar in the Now Identified Fermi-LAT Source 1FGL J2030.0+3641. *ApJ*, 746:39, feb 2012.

[19] F. Camilo, P. S. Ray, S. M. Ransom, M. Burgay, T. J. Johnson, and et al. Radio Detection of LAT PSRs J1741-2054 and J2032+4127: No Longer Just Gamma-ray Pulsars. *ApJ*, 705:1–13, nov 2009.

[20] R. G. Carlberg and K. A. Innanen. Galactic chaos and the circular velocity at the sun. *AJ*, 94:666–670, sep 1987.

[21] I. Cognard, L. Guillemot, T. J. Johnson, D. A. Smith, C. Venter, and et al. Discovery of Two Millisecond Pulsars in Fermi Sources with the Nançay Radio Telescope. *ApJ*, 732:47, may 2011.

[22] J. M. Cordes and T. J. W. Lazio. NE2001.I. A New Model for the Galactic Distribution of Free Electrons and its Fluctuations. *ArXiv Astrophysics e-prints*, astro-ph/0207156, jul 2002.

[23] A. Corongiu. Design of a tool for managing pulsar observations with the Sardinia Radio Telescope. *OAC/SRT Internal Report*.

[24] A. Corongiu. Development of a framework for building tools for managing observations with a generic telescope. *OAC/SRT Internal Report*.

[25] A. Corongiu. SRT antenna control: a graphic tool for setting and pointing the Sardinia Radio Telescope. *OAC/SRT Internal Report*.

[26] O. C. de Jager and I. Büsching. The H-test probability distribution revisited: improved sensitivity. *A&A*, 517:L9, jul 2010.

[27] O. C. de Jager, B. C. Raubenheimer, and J. W. H. Swanepoel. A poweful test for weak periodic signals with unknown light curve shape in sparse data. *A&A*, 221:180–190, aug 1989.

[28] H. R. de Ruiter, A. G. Willis, and H. C. Arp. A Westerbork 1415 MHz survey of background radio sources. II - Optical identifications with deep IIIA-J plates. *A&AS*, 28:211–293, may 1977.

[29] A. Deller. Pulsar distance measurements with VLBI. In *40th COSPAR Scientific Assembly*, volume 40 of *COSPAR Meeting*, page 674, 2014.

[30] A. T. Deller, W. F. Brisken, S. Chatterjee, J. M. Cordes, W. M. Goss, and et al. PSRπ: A large VLBA pulsar astrometry program. In W. Alef, S. Bernhart, and A. Nothnagel, editors, *20th Meeting of the European VLBI Group for Geodesy and Astronomy, held in Bonn, Germany, March 29-30, 2011, Eds: W. Alef, S. Bernhart, and A. Nothnagel,*

Institut für Geodäsie und Geoinformation, Rheinischen Friedrich-Wilhelms-Universität Bonn, p. 178-182, pages 178–182, jul 2011.

[31] Y. J. Du, J. L. Han, G. J. Qiao, and C. K. Chou. Gamma-ray Emission from the Vela Pulsar Modeled with the Annular Gap and the Core Gap. *ApJ*, 731:2, apr 2011.

[32] E. Egron and et al. Observing with the DFB at SRT: Practical notes for the user. *OAC/SRT Internal Report*.

[33] C. L. Fryer. Mass limits for black hole formation. *ApJ*, 522:413–418, 1999.

[34] G. Ghisellini and F. Tavecchio. Fermi/LAT broad emission line blazars. *MNRAS*, 448:1060–1077, apr 2015.

[35] P. L. Gonthier, S. A. Story, B. D. Clow, and A. K. Harding. Population statistics study of radio and gamma-ray pulsars in the Galactic plane. *Ap&SS*, 309:245–251, jun 2007.

[36] W. E. Harris. A Catalog of Parameters for Globular Clusters in the Milky Way. *AJ*, 112:1487, oct 1996.

[37] J. W. T. Hessels, M. S. E. Roberts, M. A. McLaughlin, P. S. Ray, P. Bangale, and et al. A 350-MHz GBT Survey of 50 Faint Fermi γ-ray Sources for Radio Millisecond Pulsars. In *American Institute of Physics Conference Series*, volume 1357, pages 40–43, aug 2011.

[38] J. J. Hester. General talk on Crab properties based on Ann. Rev. Paper. In *Polarimetry days in Rome: Crab status, theory and prospects*, 2008.

[39] G. Hobbs, R. Edwards, and R. Manchester. TEMPO2: a New Pulsar Timing Package. *Chinese Journal of Astronomy and Astrophysics Supplement*, 6:189–192, dec 2006.

[40] V. M. Kaspi. Grand unification of neutron stars. *Proc. Nat. Acad. Sci.*, 107:7147–7152, apr 2010.

[41] M. Kerr, F. Camilo, T. J. Johnson, E. C. Ferrara, L. Guillemot, and et al. Five New Millisecond Pulsars from a Radio Survey of 14 Unidentified Fermi-LAT Gamma-Ray Sources. *ApJ*, 748:L2, mar 2012.

[42] S. Klepser, S. Carrigan, E. de Oña Wilhelmi, C. Deil, A. Förster, and et al. A Population of Teraelectronvolt Pulsar Wind Nebulae in the H.E.S.S. Galactic Plane Survey. *ArXiv e-prints*, jul 2013.

[43] D. A. Kniffen, R. C. Hartman, D. J. Thompson, G. F. Bignami, and C. E. Fichtel. Gamma radiation from the Crab Nebula above 35 MeV. *Nature*, 251:397–399, oct 1974.

[44] K. Kuijken and G. Gilmore. The mass distribution in the galactic disc. I - A technique to determine the integral surface mass density of the disc near the sun. *MNRAS*, 239:571–603, aug 1989.

[45] K. D. Lawson, C. J. Mayer, J. L. Osborne, and M. L. Parkinson. Variations in the Spectral Index of the Galactic Radio Continuum Emission in the Northern Hemisphere. *MNRAS*, 225:307–327, 1987.

[46] Q. Z. Liu, J. van Paradijs, and E. P. J. van den Heuvel. Catalogue of high-mass X-ray binaries in the Galaxy (4th edition). *A&A*, 455:1165–1168, sep 2006.

[47] D. Lorimer and M. Kramer. *Handbook of Pulsar Astronomy*. Cambridge Univ Pr, 2005.

[48] D. R. Lorimer, J. A. Yates, A. G. Lyne, and D. M. Gould. Multifrequency flux density measurements of 280 pulsars. *MNRAS*, 273:411–421, mar 1995.

[49] R. N. Manchester, G. B. Hobbs, A. Teoh, and M. Hobbs. The Australia Telescope National Facility Pulsar Catalogue. *AJ*, 129:1993–2006, apr 2005.

[50] O. Maron, J. Kijak, M. Kramer, and R. Wielebinski. Pulsar spectra of radio emission. *A&AS*, 147:195–203, dec 2000.

[51] M. Marongiu. Ottimizzazione di osservazioni di pulsar con il Sardinia Radio Telescope. Master's thesis, Università degli Studi di Cagliari, Corso di Laurea Magistrale in Fisica, 2013.

[52] J. R. Mattox, D. L. Bertsch, J. Chiang, B. L. Dingus, S. W. Digel, and et al. The Likelihood Analysis of EGRET Data. *ApJ*, 461:396, apr 1996.

[53] P. Moran, A. Shearer, R. P. Mignani, A. Słowikowska, A. De Luca, and et al. Optical polarimetry of the inner Crab nebula and pulsar. *MNRAS*, jun 2013.

[54] A. G. Muslimov and A. K. Harding. High-Altitude Particle Acceleration and Radiation in Pulsar Slot Gaps. *ApJ*, 606:1143–1153, may 2004.

[55] P. L. Nolan, A. A. Abdo, M. Ackermann, M. Ajello, A. Allafort, and et al. Fermi LAT second source catalog (2FGL) (Nolan+, 2012). *VizieR Online Data Catalog*, 219:90031, jun 2012.

[56] A. Orlati, M. Buttu, A. Melis, C. Migoni, S. Poppi, and et al. The control software for the Sardinia Radio Telescope. In *Society of Photo-Optical Instrumentation Engineers (SPIE) Conference Series*, volume 8451 of *Society of Photo-Optical Instrumentation Engineers (SPIE) Conference Series*, page 2, sep 2012.

[57] D. Parent, M. Kerr, P. R. den Hartog, M. G. Baring, M. E. DeCesar, and et al. Observations of Energetic High Magnetic Field Pulsars with the Fermi Large Area Telescope. *ApJ*, 743:170, dec 2011.

[58] A. Pellizzoni, M. Pilia, A. Possenti, A. Chen, A. Giuliani, and et al. Discovery of New Gamma-Ray Pulsars with AGILE. *ApJ*, 695:L115–L119, apr 2009.

[59] A. Pellizzoni, A. Trois, M. Tavani, M. Pilia, A. Giuliani, and et al. Detection of Gamma-Ray Emission from the Vela Pulsar Wind Nebula with AGILE. *Science*, 327:663–, feb 2010.

[60] J. Pétri. The pulsar force-free magnetosphere linked to its striped wind: time-dependent pseudo-spectral simulations. *MNRAS*, 424:605–619, jul 2012.

[61] S. A. Petrova. Mechanisms of the Physical Connection between the Radio and High-energy Emissions of Pulsars. 407:309, sep 2009.

[62] M. Pierbattista, I. A. Grenier, A. K. Harding, and P. L. Gonthier. Constraining γ-ray pulsar gap models with a simulated pulsar population. *A&A*, 545:A42, sep 2012.

[63] H. J. Pletsch, L. Guillemot, B. Allen, M. Kramer, C. Aulbert, and et al. Discovery of Nine Gamma-Ray Pulsars in Fermi Large Area Telescope Data Using a New Blind Search Method. *ApJ*, 744:105, jan 2012.

[64] A. Possenti. Pulsars and collapsed objects. In *Proceedings of the First MCCT-SKADS Training School*, page 14, 2007.

[65] A. Possenti, R. Cerutti, M. Colpi, and S. Mereghetti. Re-examining the X-ray versus spin-down luminosity correlation of rotation powered pulsars. *A&A*, 387:993–1002, jun 2002.

[66] V. Radhakrishnan and D. J. Cooke. Magnetic Poles and the Polarization Structure of Pulsar Radiation. *Astrophys. Lett.*, 3:225, 1969.

[67] S. M. Ransom, S. S. Eikenberry, and J. Middleditch. Fourier Techniques for Very Long Astrophysical Time-Series Analysis. *AJ*, 124:1788–1809, sep 2002.

[68] S. M. Ransom, P. S. Ray, F. Camilo, M. S. E. Roberts, Ö. Çelik, and et al. Three Millisecond Pulsars in Fermi LAT Unassociated Bright Sources. *ApJ*, 727:L16, jan 2011.

[69] P. S. Ray, A. A. Abdo, D. Parent, D. Bhattacharya, B. Bhattacharyya, and et al. Radio Searches of Fermi LAT Sources and Blind Search Pulsars: The Fermi Pulsar Search Consortium. *ArXiv e-prints*, 1205.3089, may 2012.

[70] P. S. Ray, M. Kerr, D. Parent, A. A. Abdo, L. Guillemot, and et al. Precise γ-ray Timing and Radio Observations of 17 Fermi γ-ray Pulsars. *ApJS*, 194:17, jun 2011.

[71] R. W. Romani. 2FGL J1311.7-3429 Joins the Black Widow Club. *ApJ*, 754:L25, aug 2012.

[72] P. M. Saz Parkinson, M. Dormody, M. Ziegler, P. S. Ray, A. A. Abdo, and et al. Eight γ-ray Pulsars Discovered in Blind Frequency Searches of Fermi LAT Data. *ApJ*, 725:571–584, dec 2010.

[73] A. Shearer and A. Golden. Implications of the Optical Observations of Isolated Neutron Stars. *ApJ*, 547:967–972, feb 2001.

[74] I. S. Shklovskii. Possible Causes of the Secular Increase in Pulsar Periods. *Sov. Astron.*, 13:562, feb 1970.

[75] D. Sowards-Emmerd, R. W. Romani, and P. F. Michelson. The Gamma-Ray Blazar Content of the Northern Sky. *ApJ*, 590:109–122, jun 2003.

[76] B. W. Stappers, B. M. Gaensler, V. M. Kaspi, M. van der Klis, and W. H. G. Lewin. An X-ray nebula associated with the millisecond pulsar B1957+20. *Science*, 299:1372–1374, 2003.

[77] J. Takata, Y. Wang, and K. S. Cheng. Pulsar High Energy Emissions from Outer Gap Accelerator Closed by a Magnetic Pair-creation Process. *ApJ*, 715:1318–1326, jun 2010.

[78] M. Tavani, G. Barbiellini, A. Argan, F. Boffelli, A. Bulgarelli, and et al. The AGILE Mission. *A&A*, 502:995–1013, aug 2009.

[79] The Fermi-LAT Collaboration. Fermi Large Area Telescope Third Source Catalog. *ArXiv e-prints*, 1501.02003, jan 2015.

[80] C. Thompson. Nature of the Soft Gamma Repeaters and Anomalous X-ray Pulsars. In M. Feroci, S. Mereghetti, and L. Stella, editors, *The Rome 2000 Mini-workshop*, 2001.

[81] D. J. Thompson. Gamma Ray Pulsars. In *Cosmic Gamma-Ray Sources*, volume 304 of *Astrophysics and Space Science Library*, page 149, 2004.

[82] D. J. Thompson. Gamma ray astrophysics: the EGRET results. *Reports on Progress in Physics*, 71(11):116901, nov 2008.

[83] D. J. Thompson, Z. Arzoumanian, D. L. Bertsch, K. T. S. Brazier, J. Chiang, and et al. EGRET high-energy gamma-ray pulsar studies. 1: Young spin-powered pulsars. *ApJ*, 436:229–238, nov 1994.

[84] D. J. Thompson, C. E. Fichtel, D. A. Kniffen, and H. B. Ogelman. SAS-2 high-energy gamma-ray observations of the VELA pulsar. *ApJ*, 200:L79–L82, sep 1975.

[85] V. Vacca, M. N. Iacolina, A. Pellizzoni, S. A. Iacolina, A. Trois, and et al. CASTIA - A Source Visibility Tool for the Italian Radio Telescopes. *Internal Report INAF - IRA*, 468/13:10, may 2013.

[86] C. Venter, T. J. Johnson, and A. K. Harding. Modeling Phase-aligned Gamma-Ray and Radio Millisecond Pulsar Light Curves. *ApJ*, 744:34, jan 2012.

[87] R.-B. Wang and K. Hirotani. Death Line of Gamma-Ray Pulsars with Outer Gaps. *ApJ*, 736:127, aug 2011.

[88] Y. Wang, J. Takata, and K. S. Cheng. Three-dimensional two-layer outer gap model: Fermi energy-dependent light curves of the Vela pulsar. *MNRAS*, 414:2664–2673, jul 2011.

[89] D. Zyuzin, Y. Shibanov, A. Danilenko, R. E. Mennickent, and S. Zharikov. The Vela pulsar and its likely counter-jet in the K_s band. *ApJ*, 775:101, oct 2013.

A Sample of 326 gamma-ray sources potentially observable by SRT to search for new pulsars

Tables 10 and 11 show the sample of 326 gamma-ray sources (selected from 1009 unidentified gamma-ray sources in the 3FGL catalog), potentially observable with SRT, among which new radio and/or gamma-ray pulsars could be identified, with the procedure described in section 4.2.3.

In the tables, ra and dec are the right ascension and the declination of the gamma-ray source respectively; s_{max} and s_{min} are the semi-major and the semi-minor axis of the error box at 95% confidence respectively; l and b are the galactic longitude and the galactic latitude respectively; G_{100} is the energy flux in range $0.1 \div 100$ GeV; $signif_{avg}$ is the significance of the detection of the gamma-ray source; $\mathcal{V}$ is the variability; α_γ is the photon spectral index; $n_{punt\,P}$, $n_{punt\,L}$, $n_{punt\,C}$ and $n_{punt\,K}$ are the number of pointings practicable by SRT respectively in P-band ($\nu_0 = 0.3575$ GHz), L-band ($\nu_0 = 1.55$ GHz), C-band ($\nu_0 = 6.7$ GHz) and K-band ($\nu_0 = 22.25$ GHz); finally, h_{trans} is the maximum elevation of the gamma-ray source.
The designator "c" to the names of the sources indicates *flags* (§3.4.5) and therefore these sources can be considered as potentially confused with interstellar emission. Their position, emission characteristics, or even existence may not be reliable.
Recently, multi-frequency studies show that the low-mass X-ray binary system 1RXS J154439.4-112820 is the most probable counterpart of the unassociated Fermi-LAT source 3FGL J1544.6-1125 (Bogdanov & Halpern, 2015[17]).

These samples are sorted by both energy flux (G_{100}, Table 10) and right ascension (ra, Table 11), in order to easier list the observational selection.

Table 10: *Sample of 326 gamma-ray sources, selected from 1009 unidentified gamma-ray sources in the 3FGL catalog, sorted by energy flux (G_{100}).*

Gamma-ray source	ra [deg]	dec [deg]	s_{max} [deg]	s_{min} [deg]	l [deg]	b [deg]	G_{100} [a]	$signif_{avg}$	$\mathcal{V}$	α_γ	$n_{punt\,P}$	$n_{punt\,L}$	$n_{punt\,C}$	$n_{punt\,K}$	h_{trans} [deg]
3FGL J1745.3-2903c	266.34	-29.0	0.02	0.02	359.86	-0.02	2.30	20.65	48.41	2.36	0.002	0.04	0.84	9.32	21.4
3FGL J1747.0-2828	266.77	-28.4	0.04	0.03	0.5571	-0.04	1.45	20.26	90.61	2.04	0.006	0.12	2.42	26.6	22.0
3FGL J1848.4-0141	282.11	-1.69	0.08	0.05	31.088	-0.11	1.14	18.67	52.63	2.58	0.022	0.41	7.84	86.2	48.8
3FGL J1839.3-0552	279.84	-5.88	0.03	0.02	26.327	-0.01	1.00	14.91	37.43	2.54	0.004	0.08	1.63	17.9	44.6
3FGL J1906.6+0720	286.67	7.333	0.03	0.02	41.192	-0.02	0.99	26.27	41.70	2.35	0.004	0.09	1.69	18.6	57.8
3FGL J1843.7-0322	280.92	-3.37	0.08	0.07	29.046	0.176	0.93	13.08	70.62	2.73	0.031	0.59	11.1	123.	47.1
3FGL J1823.2-1339	275.82	-13.6	0.02	0.02	17.604	-0.09	0.92	16.63	47.54	2.22	0.003	0.06	1.24	13.7	36.8
3FGL J1747.7-2904	266.94	-29.0	0.06	0.06	0.1261	-0.47	0.84	6.975	65.34	2.51	0.020	0.37	7.08	78.0	21.4
3FGL J1852.8+0158	283.20	1.972	0.06	0.05	34.847	0.587	0.82	13.71	54.51	2.54	0.016	0.31	5.91	65.0	52.4
3FGL J1814.1-1734c	273.54	-17.5	0.06	0.05	13.104	-0.02	0.81	9.017	56.90	2.54	0.017	0.33	6.23	68.5	32.9
3FGL J1800.8-2402	270.22	-24.0	0.03	0.03	5.9563	-0.45	0.73	17.48	46.64	2.33	0.005	0.10	1.99	21.9	26.4
3FGL J1857.9+0210	284.49	2.170	0.06	0.05	35.607	-0.46	0.68	15.18	50.61	2.59	0.016	0.31	5.87	64.6	52.6
3FGL J1740.5-2843	265.12	-28.7	0.06	0.05	359.59	1.068	0.67	15.12	46.42	2.39	0.017	0.32	5.99	65.9	21.7
3FGL J2017.9+3627	304.48	36.45	0.03	0.03	74.541	0.410	0.65	25.03	39.85	2.61	0.005	0.09	1.85	20.4	86.9
3FGL J1850.5-0024	282.63	-0.40	0.05	0.04	32.468	0.017	0.57	9.435	64.26	2.41	0.011	0.21	4.03	44.4	50.1
3FGL J1857.2+0059	284.31	0.986	0.04	0.03	34.471	-0.84	0.48	12.39	57.13	2.26	0.007	0.13	2.56	28.2	51.4
3FGL J1919.9+1407	289.98	14.11	0.07	0.06	48.710	0.241	0.46	10.87	67.72	2.69	0.023	0.43	8.14	89.5	64.6
3FGL J0634.1+0424	98.528	4.406	0.10	0.08	207.03	-1.83	0.46	21.06	42.87	2.75	0.046	0.87	16.4	180.	54.9
3FGL J1749.2-2911	267.31	-29.1	0.08	0.05	0.1925	-0.81	0.45	11.72	41.77	2.57	0.021	0.41	7.70	84.8	21.3
3FGL J1855.4+0454	283.85	4.911	0.08	0.06	37.758	1.352	0.45	9.476	38.60	2.54	0.028	0.54	10.1	111.	55.4
3FGL J2004.4+3338	301.10	33.64	0.03	0.03	70.671	1.185	0.43	18.46	50.29	2.29	0.005	0.10	1.98	21.8	84.1
3FGL J1831.7-0230	277.94	-2.50	0.09	0.08	28.458	3.228	0.42	9.250	31.10	2.85	0.038	0.71	13.3	146.	48.0
3FGL J1748.3-2815c	267.09	-28.2	0.03	0.02	0.8925	-0.16	0.42	15.10	34.06	2.27	0.004	0.07	1.46	16.1	22.2
3FGL J1754.0-2538	268.50	-25.6	0.02	0.02	3.7810	0.084	0.41	16.83	66.89	2.15	0.003	0.07	1.32	14.5	24.8
3FGL J1754.0-2930	268.50	-29.5	0.10	0.08	0.4506	-1.86	0.41	15.03	59.67	2.62	0.043	0.81	15.2	167.	21.0
3FGL J1819.5-1345	274.89	-13.7	0.08	0.08	17.083	0.645	0.41	7.689	77.81	2.47	0.036	0.67	12.6	139.	36.7
3FGL J0223.6+6204	35.906	62.08	0.03	0.03	133.49	1.115	0.39	12.87	41.77	2.80	0.006	0.12	2.36	25.9	67.4
3FGL J2038.4+4212	309.62	42.20	0.05	0.05	81.527	0.542	0.39	11.75	45.66	2.69	0.015	0.28	5.34	58.8	87.2
3FGL J1740.5-2726	265.13	-27.4	0.09	0.08	0.6765	1.733	0.38	12.75	43.15	2.32	0.036	0.69	12.9	142.	23.0
3FGL J1744.7-3043	266.18	-30.7	0.07	0.05	358.37	-0.76	0.38	6.583	58.49	2.36	0.019	0.37	6.97	76.7	19.7
3FGL J1857.9+0355	284.48	3.927	0.07	0.06	37.170	0.342	0.37	9.268	55.58	2.68	0.022	0.41	7.78	85.6	54.4
3FGL J0340.4+5302	55.100	53.04	0.10	0.09	146.78	-1.81	0.36	22.30	46.59	2.36	0.048	0.91	17.1	188.	76.4
3FGL J1758.8-2346	269.70	-23.7	0.05	0.05	5.9409	0.081	0.36	7.314	41.79	2.07	0.014	0.27	5.15	56.7	26.7
3FGL J1901.5-0126	285.39	-1.44	0.05	0.05	32.801	-2.92	0.36	13.97	60.36	2.61	0.014	0.27	5.04	55.5	49.0
3FGL J2023.5+4126	305.87	41.43	0.09	0.09	79.253	2.341	0.34	11.63	48.95	2.53	0.042	0.80	15.0	165.	88.0
3FGL J1849.5-0124c	282.39	-1.41	0.07	0.06	31.463	-0.23	0.34	4.902	36.74	2.28	0.024	0.46	8.60	94.7	49.0
3FGL J1653.6-0158	253.41	-1.98	0.03	0.03	16.618	24.92	0.33	31.94	55.40	2.06	0.005	0.11	2.07	22.7	48.5
3FGL J1742.6-3321	265.66	-33.3	0.06	0.06	355.90	-1.77	0.32	15.31	48.24	2.36	0.019	0.37	7.01	77.2	17.1

[a] *In units of* 10^{-10} *erg* s^{-1} cm^{-2}

This table continues in the next page

This table continues from the previous page

Gamma-ray source	ra [deg]	dec [deg]	s_{max} [deg]	s_{min} [deg]	l [deg]	b [deg]	G_{100} [(a)]	$signif_{avg}$	$\mathcal{V}$	α_γ	$n_{punt\,P}$	$n_{punt\,L}$	$n_{punt\,C}$	$n_{punt\,K}$	h_{trans} [deg]
3FGL J1809.2-2016c	272.32	-20.2	0.05	0.04	10.182	-0.31	0.32	5.413	42.14	2.32	0.012	0.23	4.33	47.7	30.2
3FGL J2041.1+4736	310.28	47.60	0.05	0.04	86.091	3.461	0.31	18.37	56.27	2.13	0.011	0.22	4.16	45.8	81.8
3FGL J1857.8+0129c	284.47	1.497	0.10	0.07	35.000	-0.75	0.31	4.475	41.47	2.34	0.037	0.70	13.2	145.	52.0
3FGL J2032.5+3921	308.13	39.35	0.09	0.06	78.573	-0.26	0.31	11.31	49.41	2.64	0.031	0.60	11.2	123.	89.8
3FGL J1901.1+0728	285.29	7.475	0.10	0.10	40.693	1.249	0.31	8.694	55.34	2.73	0.051	0.96	18.0	198.	57.9
3FGL J1814.0-1757c	273.51	-17.9	0.09	0.06	12.757	-0.17	0.31	5.365	50.07	2.18	0.028	0.53	10.0	110.	32.5
3FGL J1915.2+0954	288.80	9.908	0.09	0.07	44.449	-0.70	0.31	7.705	52.03	2.60	0.034	0.65	12.2	134.	60.4
3FGL J1827.6-0846	276.90	-8.77	0.05	0.04	22.418	1.241	0.30	8.678	51.62	2.36	0.012	0.23	4.32	47.6	41.7
3FGL J1830.7-1630	277.69	-16.5	0.07	0.05	15.911	-3.03	0.30	12.13	49.00	2.43	0.020	0.37	7.04	77.5	33.9
3FGL J1838.9-0646	279.72	-6.77	0.07	0.05	25.477	-0.31	0.29	7.123	50.15	1.92	0.022	0.41	7.80	85.9	43.7
3FGL J1844.3-0344	281.10	-3.74	0.05	0.04	28.795	-0.14	0.28	10.06	44.78	2.28	0.012	0.23	4.45	49.0	46.7
3FGL J1747.0-3506	266.75	-35.1	0.09	0.07	354.87	-3.45	0.27	11.69	64.48	2.66	0.032	0.61	11.4	126.	15.4
3FGL J1831.7-0157c	277.94	-1.96	0.10	0.09	28.940	3.471	0.27	5.065	38.17	2.53	0.050	0.95	17.8	196.	48.5
3FGL J1626.2-2428c	246.57	-24.4	0.05	0.05	352.99	16.89	0.26	9.404	46.86	2.27	0.013	0.26	4.90	53.9	26.0
3FGL J1837.6-0717	279.40	-7.29	0.08	0.05	24.866	-0.26	0.26	5.551	41.26	2.03	0.023	0.44	8.40	92.4	43.2
3FGL J1739.9-3124c	264.99	-31.4	0.08	0.05	357.25	-0.25	0.26	5.092	48.21	2.28	0.024	0.46	8.62	94.9	19.1
3FGL J0225.8+6159	36.472	61.98	0.09	0.08	133.77	1.120	0.26	8.304	46.68	2.88	0.037	0.70	13.2	145.	67.5
3FGL J2034.4+3833c	308.62	38.56	0.05	0.05	78.158	-1.04	0.26	8.889	55.76	2.52	0.013	0.24	4.65	51.1	89.0
3FGL J1758.8-2402	269.70	-24.0	0.07	0.07	5.7203	-0.04	0.25	5.339	54.83	1.99	0.026	0.49	9.34	102.	26.4
3FGL J1928.9+1739	292.23	17.65	0.08	0.05	52.854	0.007	0.25	8.506	47.86	2.63	0.022	0.42	7.92	87.2	68.1
3FGL J2108.1+5202	317.04	52.04	0.08	0.06	92.302	2.977	0.24	9.666	57.21	2.50	0.024	0.46	8.69	95.6	77.4
3FGL J0359.5+5413	59.881	54.22	0.04	0.04	148.25	0.871	0.24	19.16	33.63	2.02	0.007	0.14	2.78	30.6	75.2
3FGL J0744.1-2523	116.04	-25.3	0.05	0.05	241.33	-0.69	0.23	18.10	61.34	2.08	0.013	0.24	4.65	51.1	25.1
3FGL J1628.2-2431c	247.06	-24.5	0.10	0.09	353.26	16.51	0.23	7.913	30.28	2.37	0.044	0.83	15.5	170.	25.9
3FGL J1816.5-1145	274.12	-11.7	0.10	0.08	18.488	2.253	0.23	5.896	48.28	2.48	0.041	0.77	14.4	158.	38.7
3FGL J1827.3-1446	276.83	-14.7	0.06	0.04	17.076	-1.48	0.22	9.099	40.00	2.47	0.013	0.24	4.64	51.0	35.7
3FGL J1902.6+0655	285.65	6.931	0.08	0.05	40.373	0.682	0.22	5.976	32.63	2.23	0.021	0.40	7.59	83.5	57.4
3FGL J1824.3-0620	276.09	-6.33	0.05	0.05	24.198	3.082	0.21	9.762	42.05	2.24	0.014	0.26	4.92	54.1	44.1
3FGL J1810.8-2412	272.71	-24.2	0.10	0.06	6.9129	-2.52	0.21	6.206	62.02	2.32	0.033	0.63	11.8	130.	26.2
3FGL J1834.8-0630c	278.71	-6.51	0.08	0.07	25.249	0.701	0.21	4.682	36.02	2.21	0.030	0.57	10.6	117.	43.9
3FGL J1904.7-0708	286.19	-7.13	0.06	0.06	28.071	-6.20	0.21	11.68	57.99	2.58	0.020	0.37	7.05	77.6	43.3
3FGL J0426.7+5437	66.681	54.61	0.07	0.06	150.86	3.873	0.21	14.19	51.83	2.46	0.023	0.43	8.14	89.6	74.8
3FGL J1925.4+1727	291.37	17.46	0.10	0.08	52.291	0.638	0.21	9.610	47.33	2.24	0.042	0.80	15.0	165.	67.9
3FGL J1734.7-2930	263.69	-29.5	0.09	0.08	358.26	1.700	0.21	8.971	70.28	2.52	0.039	0.74	13.8	152.	21.0
3FGL J2037.4+4132c	309.35	41.53	0.08	0.07	80.868	0.294	0.20	6.446	40.86	2.17	0.030	0.57	10.7	117.	87.9
3FGL J0647.6+0032	101.91	0.534	0.08	0.07	212.02	-0.59	0.20	11.19	49.28	2.45	0.029	0.55	10.3	113.	51.0
3FGL J0523.3-2528	80.839	-25.4	0.04	0.04	228.20	-29.8	0.19	26.14	50.15	2.15	0.008	0.15	2.90	31.9	25.0
3FGL J1804.5-0850	271.13	-8.84	0.10	0.08	19.649	6.238	0.19	8.071	55.43	2.74	0.046	0.86	16.2	178.	41.6
3FGL J2036.8+4234c	309.22	42.56	0.07	0.07	81.633	0.997	0.19	5.376	42.08	2.25	0.027	0.51	9.62	105.	86.9

[a] *In units of* 10^{-10} *erg* s^{-1} cm^{-2}

This table continues in the next page

This table continues from the previous page

Gamma-ray source	ra [deg]	dec [deg]	s_{max} [deg]	s_{min} [deg]	l [deg]	b [deg]	G_{100} [(a)]	$signif_{avg}$	$\mathcal{V}$	α_γ	$n_{punt\,P}$	$n_{punt\,L}$	$n_{punt\,C}$	$n_{punt\,K}$	h_{trans} [deg]
3FGL J1759.6-2141	269.91	-21.6	0.07	0.05	7.8477	0.960	0.19	5.153	37.28	2.28	0.017	0.33	6.26	68.9	28.8
3FGL J2112.5-3044	318.14	-30.7	0.03	0.03	14.898	-42.4	0.19	30.14	51.84	1.67	0.005	0.10	1.96	21.6	19.7
3FGL J0002.6+6218	0.6745	62.30	0.06	0.05	117.30	-0.03	0.18	17.97	48.02	2.08	0.015	0.29	5.55	61.0	67.1
3FGL J1625.1-0021	246.27	-0.35	0.03	0.03	13.880	31.83	0.18	28.53	37.31	1.66	0.006	0.12	2.32	25.6	50.1
3FGL J1732.4-2709	263.12	-27.1	0.07	0.06	359.96	3.402	0.18	6.138	51.77	2.37	0.022	0.42	7.92	87.2	23.3
3FGL J1736.0-2701	264.01	-27.0	0.08	0.08	0.5107	2.801	0.18	8.272	38.45	2.55	0.033	0.62	11.6	128.	23.4
3FGL J0605.9+2039c	91.476	20.65	0.10	0.08	189.47	-0.20	0.17	6.884	50.56	2.35	0.043	0.81	15.2	167.	71.1
3FGL J1733.5-2811	263.38	-28.1	0.06	0.05	359.21	2.642	0.17	5.154	44.61	2.44	0.018	0.34	6.41	70.5	22.3
3FGL J0637.5+0418	99.383	4.315	0.08	0.07	207.50	-1.11	0.17	8.777	71.36	3.03	0.033	0.62	11.7	128.	54.8
3FGL J2233.1+6542	338.27	65.71	0.09	0.08	109.34	6.561	0.17	12.69	52.49	2.27	0.039	0.75	14.0	154.	63.7
3FGL J0212.1+5320	33.037	53.33	0.03	0.03	134.92	-7.64	0.17	25.06	51.47	1.95	0.005	0.10	1.97	21.7	76.1
3FGL J1904.9+0818	286.24	8.306	0.10	0.07	41.861	0.795	0.16	4.663	48.07	2.29	0.040	0.76	14.3	158.	58.8
3FGL J1949.3+2433	297.32	24.56	0.07	0.06	61.203	-0.72	0.16	8.171	42.17	2.77	0.025	0.47	8.79	96.7	75.0
3FGL J1119.9-2204	169.98	-22.0	0.04	0.03	276.47	36.05	0.16	30.16	62.62	1.81	0.007	0.14	2.77	30.5	28.4
3FGL J1740.5-2642	265.13	-26.7	0.09	0.07	1.3043	2.122	0.16	8.788	33.42	2.30	0.033	0.63	11.9	131.	23.7
3FGL J1943.8+2518	295.97	25.30	0.12	0.08	61.222	0.708	0.16	6.386	40.48	2.35	0.052	0.98	18.4	203.	75.8
3FGL J1801.6-2213	270.40	-22.2	0.05	0.03	7.6147	0.304	0.16	5.131	40.07	1.96	0.010	0.19	3.70	40.7	28.2
3FGL J0611.5+1957	92.899	19.96	0.09	0.08	190.72	0.628	0.15	6.924	46.41	2.38	0.040	0.75	14.1	155.	70.4
3FGL J0419.1+6636	64.778	66.60	0.05	0.04	141.53	11.56	0.15	14.46	49.15	2.31	0.012	0.24	4.50	49.5	62.8
3FGL J0619.4+2242	94.874	22.70	0.10	0.06	189.18	3.552	0.15	5.485	51.68	2.01	0.035	0.67	12.5	138.	73.2
3FGL J0221.8+6138c	35.472	61.64	0.10	0.07	133.45	0.631	0.14	4.666	44.20	2.41	0.038	0.72	13.4	148.	67.8
3FGL J1856.1-1217	284.03	-12.2	0.06	0.05	22.464	-6.60	0.14	8.368	50.87	2.58	0.018	0.35	6.63	73.0	38.2
3FGL J1803.1-2728	270.78	-27.4	0.10	0.07	3.2211	-2.58	0.14	5.917	57.27	2.33	0.039	0.75	14.0	154.	23.0
3FGL J1548.4+1455	237.11	14.92	0.03	0.03	25.632	47.17	0.14	17.25	67.42	2.11	0.007	0.13	2.59	28.5	65.4
3FGL J1911.7+0307	287.93	3.130	0.08	0.06	38.036	-3.07	0.14	7.057	52.94	2.32	0.027	0.51	9.64	106.	53.6
3FGL J0307.3+4916	46.843	49.27	0.03	0.02	144.53	-7.81	0.14	14.80	53.47	2.09	0.004	0.08	1.53	16.8	80.2
3FGL J0737.2-3233	114.31	-32.5	0.10	0.08	246.84	-5.53	0.13	12.86	51.33	2.25	0.040	0.75	14.1	156.	17.9
3FGL J1924.8-1034	291.20	-10.5	0.11	0.08	27.158	-12.1	0.13	10.53	48.62	2.34	0.043	0.82	15.3	169.	39.9
3FGL J0000.1+6545	0.0377	65.75	0.10	0.07	117.69	3.402	0.13	6.813	40.75	2.41	0.038	0.72	13.4	148.	63.7
3FGL J1544.6-1125	236.17	-11.4	0.07	0.06	356.21	32.98	0.13	10.84	47.47	2.41	0.025	0.47	8.80	96.8	39.0
3FGL J1845.5-2524	281.38	-25.4	0.10	0.08	9.4406	-10.0	0.12	9.181	40.44	2.28	0.042	0.79	14.8	163.	25.0
3FGL J1749.7-0305	267.44	-3.08	0.08	0.07	22.979	12.21	0.12	7.365	47.41	2.42	0.032	0.61	11.5	126.	47.4
3FGL J2117.6+3725	319.42	37.42	0.11	0.08	82.798	-8.27	0.12	14.49	49.94	2.09	0.047	0.88	16.5	181.	87.9
3FGL J0838.8-2829	129.70	-28.4	0.05	0.05	250.60	7.800	0.12	13.74	42.93	2.22	0.014	0.26	4.99	55.0	22.0
3FGL J0535.7-0617c	83.934	-6.29	0.09	0.08	209.92	-19.6	0.12	6.202	41.18	2.39	0.042	0.80	14.9	164.	44.2
3FGL J2033.3+4348c	308.33	43.81	0.07	0.06	82.243	2.258	0.12	4.392	39.38	2.24	0.022	0.42	7.92	87.2	85.6
3FGL J1722.7-0415	260.69	-4.26	0.11	0.08	18.495	17.51	0.12	6.431	34.02	2.29	0.046	0.87	16.3	180.	46.2
3FGL J2035.0+3634	308.75	36.58	0.05	0.04	76.633	-2.31	0.12	11.92	52.58	1.89	0.011	0.21	3.92	43.1	87.0
3FGL J1949.6+2355	297.41	23.92	0.10	0.09	60.689	-1.11	0.12	4.709	30.03	2.29	0.048	0.91	17.1	188.	74.4

[a] *In units of* 10^{-10} *erg* s^{-1} cm^{-2}

This table continues in the next page

This table continues from the previous page

Gamma-ray source	ra [deg]	dec [deg]	s_{max} [deg]	s_{min} [deg]	l [deg]	b [deg]	G_{100} [(a)]	$signif_{avg}$	$\mathcal{V}$	α_γ	$n_{punt\,P}$	$n_{punt\,L}$	$n_{punt\,C}$	$n_{punt\,K}$	h_{trans} [deg]
3FGL J0004.2+6757	1.0551	67.95	0.10	0.08	118.50	5.494	0.11	6.005	34.81	2.49	0.043	0.82	15.4	169.	61.5
3FGL J2114.0+5239	318.52	52.65	0.06	0.05	93.366	2.734	0.11	6.950	56.83	2.38	0.019	0.37	6.97	76.7	76.8
3FGL J0609.2+2051c	92.318	20.86	0.06	0.06	189.67	0.587	0.11	4.960	33.28	2.27	0.020	0.38	7.25	79.8	71.3
3FGL J0659.2-0439c	104.80	-4.65	0.10	0.08	217.95	-0.39	0.11	5.624	41.52	2.40	0.040	0.77	14.3	158.	45.8
3FGL J0238.0+5237	39.504	52.62	0.05	0.05	138.84	-6.92	0.11	14.99	36.58	2.13	0.014	0.27	5.13	56.4	76.8
3FGL J1539.2-3324	234.82	-33.4	0.03	0.03	338.75	17.53	0.11	19.23	57.87	1.55	0.006	0.11	2.19	24.1	17.0
3FGL J0342.3+3148c	55.576	31.80	0.10	0.07	160.34	-18.3	0.11	6.768	47.92	2.27	0.039	0.73	13.8	152.	82.3
3FGL J2217.2+6346	334.30	63.77	0.06	0.05	106.86	5.823	0.11	7.129	38.68	2.30	0.018	0.34	6.50	71.5	65.7
3FGL J0248.4+5130	42.110	51.51	0.04	0.03	140.78	-7.25	0.11	11.91	33.03	2.06	0.007	0.14	2.64	29.1	77.9
3FGL J2250.3+1747	342.58	17.79	0.09	0.07	86.354	-36.3	0.11	7.183	87.05	2.78	0.033	0.63	11.8	129.	68.3
3FGL J1720.7+0711	260.19	7.189	0.09	0.07	28.997	23.41	0.11	9.546	44.07	2.35	0.032	0.60	11.3	124.	57.6
3FGL J0235.7+5647	38.927	56.78	0.10	0.09	136.88	-3.23	0.11	8.243	60.79	2.60	0.050	0.94	17.5	193.	72.7
3FGL J1806.7-2451	271.68	-24.8	0.08	0.06	5.8945	-2.01	0.11	4.210	41.68	2.20	0.029	0.56	10.4	115.	25.6
3FGL J1802.4-3043	270.61	-30.7	0.08	0.05	0.3038	-4.05	0.10	6.031	37.90	2.11	0.023	0.44	8.29	91.3	19.7
3FGL J1625.6-2058	246.42	-20.9	0.10	0.09	355.66	19.28	0.10	6.498	39.46	2.54	0.047	0.88	16.5	181.	29.5
3FGL J1659.0-0142	254.77	-1.70	0.09	0.08	17.646	23.90	0.10	8.527	56.58	2.19	0.039	0.74	13.9	153.	48.8
3FGL J1844.7-1224	281.18	-12.4	0.10	0.08	21.109	-4.16	0.10	5.359	52.43	2.27	0.040	0.76	14.3	157.	38.0
3FGL J1917.1-3024	289.28	-30.4	0.09	0.07	7.5514	-18.4	0.10	9.548	46.07	2.23	0.033	0.62	11.7	129.	20.0
3FGL J2109.4+1437	317.35	14.61	0.11	0.09	63.688	-21.8	0.10	10.20	101.6	2.73	0.051	0.96	18.0	198.	65.1
3FGL J1903.9+0052	285.99	0.869	0.07	0.07	35.139	-2.39	0.10	4.389	48.26	2.14	0.027	0.50	9.50	104.	51.3
3FGL J1704.4-0528	256.12	-5.47	0.08	0.06	14.913	20.79	0.10	7.911	41.66	2.18	0.026	0.50	9.36	103.	45.0
3FGL J0524.4+2839	81.124	28.65	0.06	0.04	177.73	-4.04	0.10	9.199	53.24	2.12	0.013	0.25	4.69	51.6	79.1
3FGL J0336.1+7500	54.043	75.01	0.04	0.04	133.10	15.50	0.09	17.75	33.84	1.94	0.010	0.19	3.72	40.9	54.4
3FGL J2110.4+5946	317.61	59.77	0.07	0.07	98.252	7.967	0.09	7.387	45.32	2.53	0.027	0.51	9.58	105.	69.7
3FGL J2237.9+6320	339.48	63.33	0.10	0.09	108.59	4.240	0.09	7.222	43.19	2.46	0.044	0.84	15.7	172.	66.1
3FGL J2102.8+4704	315.72	47.06	0.09	0.07	88.034	0.281	0.09	5.729	45.48	2.07	0.032	0.61	11.4	126.	82.4
3FGL J1221.5-0632	185.37	-6.55	0.09	0.07	289.71	55.55	0.09	11.52	52.54	2.24	0.033	0.63	11.8	130.	43.9
3FGL J1704.1+1234	256.03	12.57	0.06	0.06	32.465	29.42	0.09	9.432	47.00	2.58	0.022	0.43	8.05	88.6	63.0
3FGL J1315.7-0732	198.94	-7.54	0.05	0.04	313.44	54.82	0.09	12.87	72.48	2.01	0.010	0.19	3.58	39.3	42.9
3FGL J0039.3+6256	9.8342	62.94	0.05	0.05	121.55	0.102	0.09	11.99	57.84	1.87	0.014	0.27	5.18	57.0	66.5
3FGL J2212.5+0703	333.14	7.059	0.09	0.08	68.742	-38.5	0.09	14.27	57.47	2.00	0.038	0.72	13.5	149.	57.5
3FGL J0526.4+2247	81.609	22.79	0.05	0.04	182.87	-6.93	0.08	6.019	56.72	2.40	0.013	0.24	4.61	50.7	73.3
3FGL J0751.7-2944	117.93	-29.7	0.08	0.08	245.92	-1.43	0.08	5.486	52.25	2.45	0.033	0.62	11.6	127.	20.7
3FGL J1808.3-3357	272.09	-33.9	0.09	0.08	358.06	-6.71	0.08	8.716	50.88	2.22	0.035	0.67	12.5	137.	16.5
3FGL J1225.9+2953	186.49	29.89	0.05	0.04	185.15	83.76	0.08	17.37	58.04	1.94	0.012	0.23	4.48	49.3	80.3
3FGL J0748.8-2208	117.20	-22.1	0.12	0.08	239.04	1.857	0.08	5.874	39.66	2.36	0.051	0.96	18.0	198.	28.3
3FGL J0725.8+0212	111.46	2.206	0.08	0.06	214.89	8.666	0.08	9.182	54.32	2.18	0.025	0.47	8.95	98.5	52.7
3FGL J1502.2+5553	225.55	55.88	0.07	0.06	92.785	52.89	0.08	12.62	102.7	2.58	0.021	0.40	7.64	84.1	73.6
3FGL J1129.0+3758	172.25	37.97	0.06	0.05	175.66	69.59	0.08	10.25	44.75	2.28	0.017	0.32	6.04	66.5	88.4

[a] *In units of* 10^{-10} *erg* s^{-1} cm^{-2}

This table continues in the next page

This table continues from the previous page

Gamma-ray source	ra [deg]	dec [deg]	s_{max} [deg]	s_{min} [deg]	l [deg]	b [deg]	G_{100} [(a)]	$signif_{avg}$	$\mathcal{V}$	α_γ	$n_{punt\,P}$	$n_{punt\,L}$	$n_{punt\,C}$	$n_{punt\,K}$	h_{trans} [deg]
3FGL J1829.2-1504	277.32	-15.0	0.10	0.06	17.014	-2.04	0.08	5.131	33.49	1.60	0.034	0.64	12.0	132.	35.4
3FGL J1625.2-2845	246.30	-28.7	0.12	0.08	349.52	14.20	0.08	4.739	52.96	2.52	0.050	0.94	17.6	194.	21.7
3FGL J1645.7-2149	251.44	-21.8	0.12	0.08	358.09	15.13	0.08	8.848	37.08	2.29	0.049	0.93	17.4	191.	28.6
3FGL J0425.8+5600	66.451	56.01	0.06	0.05	149.76	4.750	0.08	6.336	51.67	2.34	0.015	0.29	5.50	60.5	73.4
3FGL J2210.2+6509	332.55	65.16	0.09	0.08	107.03	7.396	0.08	4.390	36.96	2.47	0.036	0.68	12.8	141.	64.3
3FGL J0537.4+3604c	84.350	36.07	0.08	0.06	173.02	2.301	0.08	4.531	28.44	2.27	0.025	0.48	9.05	99.5	86.5
3FGL J0051.6+6445	12.903	64.75	0.07	0.05	122.95	1.887	0.08	5.553	44.15	2.27	0.020	0.38	7.20	79.2	64.7
3FGL J1740.8-1933	265.21	-19.5	0.10	0.08	7.4322	5.826	0.08	4.276	49.45	2.21	0.045	0.84	15.8	173.	30.9
3FGL J2035.6+3146	308.90	31.77	0.10	0.08	72.840	-5.28	0.08	4.602	45.38	2.67	0.041	0.78	14.6	161.	82.2
3FGL J2134.5-2131	323.64	-21.5	0.05	0.04	28.921	-45.0	0.07	11.43	46.09	2.13	0.012	0.22	4.28	47.2	28.9
3FGL J0545.6+6019	86.415	60.32	0.05	0.04	152.49	15.74	0.07	15.39	35.95	1.79	0.011	0.21	4.10	45.2	69.1
3FGL J1842.2+2742	280.56	27.70	0.07	0.06	57.131	14.09	0.07	8.299	38.69	2.13	0.024	0.46	8.60	94.7	78.2
3FGL J0605.0-0000	91.271	-0.00	0.05	0.04	207.59	-10.3	0.07	8.132	51.87	2.00	0.012	0.23	4.39	48.4	50.4
3FGL J1059.3+0224	164.84	2.416	0.10	0.09	250.78	53.53	0.07	6.809	52.37	2.35	0.046	0.87	16.4	180.	52.9
3FGL J1827.7+1141	276.92	11.69	0.10	0.08	40.781	10.51	0.07	6.490	38.60	2.11	0.042	0.80	14.9	164.	62.2
3FGL J1410.9+7406	212.74	74.10	0.04	0.03	115.74	41.89	0.07	15.76	43.48	2.16	0.007	0.14	2.75	30.2	55.3
3FGL J2247.2-0004	341.81	-0.07	0.06	0.05	69.996	-49.7	0.07	10.07	48.40	2.10	0.017	0.33	6.21	68.4	50.4
3FGL J0802.3-0941	120.59	-9.69	0.06	0.05	229.91	10.97	0.07	8.704	35.88	2.28	0.018	0.34	6.40	70.4	40.8
3FGL J0609.7-1841	92.426	-18.6	0.10	0.09	225.46	-17.3	0.07	8.551	61.79	2.29	0.045	0.85	15.9	175.	31.8
3FGL J1644.6-0911	251.17	-9.18	0.07	0.07	8.6764	22.87	0.07	4.946	38.50	2.56	0.028	0.52	9.87	108.	41.3
3FGL J1808.4-3519	272.10	-35.3	0.09	0.09	356.85	-7.36	0.07	4.916	28.43	2.30	0.043	0.81	15.2	167.	15.1
3FGL J0758.6-1451	119.65	-14.8	0.07	0.07	233.96	7.561	0.07	12.06	38.62	1.98	0.026	0.49	9.32	102.	35.6
3FGL J0843.4+6713	130.85	67.21	0.06	0.04	147.79	35.60	0.07	13.16	55.97	1.99	0.014	0.27	5.06	55.7	62.2
3FGL J0746.4-0225	116.61	-2.42	0.07	0.06	221.48	11.08	0.07	9.604	59.80	2.00	0.021	0.40	7.65	84.2	48.0
3FGL J0644.6+6035	101.15	60.59	0.06	0.05	155.04	22.59	0.07	11.11	60.28	2.27	0.018	0.34	6.36	69.9	68.9
3FGL J1458.7-2120	224.68	-21.3	0.10	0.08	338.59	32.57	0.07	7.401	35.35	2.34	0.041	0.77	14.4	159.	29.1
3FGL J2151.6+4154	327.90	41.90	0.05	0.04	90.718	-9.44	0.06	8.404	33.77	1.84	0.012	0.24	4.53	49.8	87.5
3FGL J0855.4+7142	133.86	71.71	0.10	0.09	142.15	35.22	0.06	9.268	76.98	2.57	0.046	0.88	16.4	181.	57.7
3FGL J1115.0-0701	168.76	-7.02	0.05	0.05	265.11	48.63	0.06	10.01	86.88	2.10	0.013	0.24	4.65	51.2	43.4
3FGL J0258.9+0552	44.739	5.875	0.09	0.07	170.73	-44.8	0.06	7.956	38.93	2.12	0.034	0.65	12.2	134.	56.3
3FGL J1830.8-3136	277.71	-31.6	0.11	0.08	2.3540	-9.84	0.06	5.281	40.87	2.18	0.049	0.92	17.2	190.	18.9
3FGL J0451.7+5722	72.940	57.37	0.06	0.06	151.11	8.319	0.06	6.039	28.32	2.48	0.019	0.37	6.99	76.9	72.1
3FGL J0330.6+0437	52.665	4.625	0.10	0.08	179.52	-40.1	0.06	7.381	61.66	2.23	0.043	0.81	15.3	168.	55.1
3FGL J2329.8+6102	352.45	61.04	0.06	0.05	113.21	-0.28	0.06	5.633	38.02	2.06	0.017	0.33	6.23	68.5	68.4
3FGL J2047.9-3119	311.98	-31.3	0.11	0.07	12.830	-37.3	0.06	7.103	44.27	2.52	0.044	0.83	15.5	170.	19.1
3FGL J1730.6-0357	262.66	-3.95	0.07	0.07	19.803	15.96	0.06	8.330	29.97	1.86	0.026	0.50	9.37	103.	46.5
3FGL J1627.8+3217	246.96	32.29	0.07	0.06	52.958	43.20	0.06	10.16	33.02	2.13	0.024	0.45	8.46	93.1	82.8
3FGL J1628.1-3344	247.02	-33.7	0.06	0.05	346.19	10.36	0.06	5.556	36.83	2.11	0.015	0.29	5.50	60.5	16.7
3FGL J2210.1+6043	332.53	60.72	0.05	0.05	104.44	3.782	0.06	5.158	34.82	2.21	0.015	0.28	5.37	59.1	68.7

[a] *In units of* 10^{-10} *erg* s^{-1} cm^{-2}

This table continues in the next page

This table continues from the previous page

Gamma-ray source	ra [deg]	dec [deg]	s_{max} [deg]	s_{min} [deg]	l [deg]	b [deg]	G_{100} [(a)]	$signif_{avg}$	$\mathcal{V}$	α_γ	$n_{punt\,P}$	$n_{punt\,L}$	$n_{punt\,C}$	$n_{punt\,K}$	h_{trans} [deg]
3FGL J2103.7-1113	315.94	-11.2	0.06	0.05	37.857	-34.4	0.06	12.32	50.07	1.93	0.017	0.33	6.26	68.9	39.2
3FGL J1817.3-3033	274.34	-30.5	0.09	0.08	1.9905	-6.79	0.06	4.338	56.74	2.18	0.040	0.76	14.2	157.	19.9
3FGL J0752.6-1629	118.15	-16.4	0.10	0.07	234.62	5.489	0.06	6.479	42.07	2.19	0.039	0.74	13.9	153.	34.0
3FGL J2035.8+4902	308.95	49.04	0.05	0.04	86.712	5.034	0.06	4.771	44.30	2.09	0.013	0.24	4.58	50.4	80.4
3FGL J2026.3+1430	306.58	14.51	0.09	0.07	57.260	-13.4	0.06	7.096	48.74	2.15	0.033	0.62	11.7	128.	65.0
3FGL J1120.6+0713	170.17	7.223	0.07	0.06	251.53	60.68	0.06	13.17	69.98	2.02	0.023	0.44	8.37	92.1	57.7
3FGL J2144.6+6606	326.16	66.10	0.09	0.08	105.52	9.766	0.06	4.092	43.67	2.45	0.039	0.74	13.8	152.	63.3
3FGL J1958.1+2436	299.52	24.61	0.06	0.04	62.274	-2.41	0.06	5.321	47.27	1.67	0.014	0.27	5.11	56.3	75.1
3FGL J2053.9+2922	313.47	29.37	0.04	0.04	73.361	-9.86	0.06	7.720	45.97	1.54	0.008	0.16	3.07	33.8	79.8
3FGL J0921.6+2339	140.41	23.65	0.04	0.04	204.89	42.83	0.05	9.736	58.49	1.97	0.009	0.17	3.28	36.1	74.1
3FGL J1703.6-2850	255.92	-28.8	0.08	0.07	354.92	7.649	0.05	4.117	26.87	2.22	0.031	0.59	11.2	123.	21.6
3FGL J1944.1+3919	296.03	39.32	0.07	0.06	73.482	7.584	0.05	6.181	55.29	2.18	0.024	0.46	8.70	95.8	89.8
3FGL J1249.1-2808	192.29	-28.1	0.07	0.06	302.32	34.72	0.05	8.175	49.83	2.06	0.022	0.41	7.81	86.0	22.3
3FGL J0953.7-1510	148.42	-15.1	0.06	0.06	251.93	29.60	0.05	14.00	40.21	1.81	0.021	0.40	7.56	83.2	35.3
3FGL J1720.3-0428	260.09	-4.47	0.07	0.07	17.992	17.92	0.05	4.270	53.78	2.08	0.027	0.51	9.60	105.	46.0
3FGL J1632.8+3838	248.20	38.64	0.09	0.07	61.741	42.84	0.05	4.755	29.26	2.45	0.034	0.65	12.2	134.	89.1
3FGL J0318.1+0252	49.536	2.869	0.08	0.06	178.44	-43.6	0.05	12.75	50.21	1.71	0.026	0.49	9.15	100.	53.3
3FGL J1200.4+0202	180.11	2.041	0.06	0.06	274.81	62.09	0.05	8.817	55.79	2.03	0.021	0.39	7.44	81.8	52.5
3FGL J1424.3-1753	216.09	-17.8	0.06	0.05	332.12	39.66	0.05	7.301	49.36	2.17	0.018	0.34	6.42	70.7	32.6
3FGL J1944.0-0535	296.00	-5.59	0.10	0.08	33.905	-14.2	0.05	4.365	51.19	2.34	0.045	0.84	15.8	174.	44.9
3FGL J0003.5+5721	0.8903	57.35	0.08	0.07	116.48	-4.91	0.05	5.380	31.12	2.18	0.030	0.58	10.8	119.	72.1
3FGL J0312.1-0921	48.040	-9.35	0.08	0.08	191.51	-52.3	0.05	10.92	47.55	1.87	0.035	0.65	12.3	135.	41.1
3FGL J0447.1-2540	71.794	-25.6	0.10	0.09	225.60	-37.6	0.05	7.138	38.69	2.50	0.050	0.95	17.8	195.	24.8
3FGL J0747.4-0734	116.86	-7.58	0.08	0.06	226.19	8.819	0.05	5.485	34.82	2.11	0.029	0.55	10.4	114.	42.9
3FGL J0102.1+0943	15.540	9.728	0.08	0.06	127.33	-53.0	0.05	7.093	41.74	2.06	0.026	0.50	9.38	103.	60.2
3FGL J1646.9-1332	251.74	-13.5	0.10	0.07	5.2024	19.89	0.05	4.883	41.95	1.85	0.037	0.70	13.2	145.	36.9
3FGL J0628.4+2429	97.123	24.49	0.11	0.09	188.54	6.207	0.05	4.275	42.02	2.20	0.049	0.93	17.3	191.	75.0
3FGL J0538.9+1646	84.748	16.77	0.05	0.04	189.59	-7.65	0.05	5.920	45.33	1.89	0.013	0.25	4.78	52.6	67.2
3FGL J0239.4+1326	39.868	13.44	0.07	0.06	159.19	-41.6	0.05	6.577	51.05	1.99	0.024	0.46	8.68	95.5	63.9
3FGL J0133.3+5930	23.336	59.51	0.10	0.08	128.23	-2.92	0.04	4.348	42.57	2.21	0.044	0.83	15.5	171.	69.9
3FGL J0540.0+1208	85.002	12.14	0.07	0.06	193.73	-9.83	0.04	5.346	48.38	2.10	0.022	0.42	7.88	86.8	62.6
3FGL J0941.0+6151	145.27	61.86	0.07	0.07	151.48	43.24	0.04	9.010	52.87	2.29	0.028	0.53	9.96	109.	67.6
3FGL J1049.7+1548	162.43	15.80	0.08	0.08	228.51	59.61	0.04	7.553	58.39	2.15	0.034	0.64	12.0	132.	66.3
3FGL J1231.6+4825	187.90	48.41	0.09	0.08	131.87	68.36	0.04	5.928	44.38	2.51	0.042	0.79	14.8	163.	81.0
3FGL J0559.8+3042	89.962	30.71	0.05	0.04	180.03	3.561	0.04	5.908	38.99	1.71	0.010	0.20	3.84	42.2	81.2
3FGL J1351.1-2743	207.79	-27.7	0.09	0.08	318.77	33.30	0.04	5.401	48.98	2.38	0.038	0.72	13.6	149.	22.7
3FGL J1553.1+5437	238.29	54.62	0.08	0.08	85.581	47.16	0.04	8.511	56.25	2.25	0.036	0.67	12.6	139.	74.8
3FGL J1532.0-2618	233.01	-26.3	0.09	0.08	342.21	24.06	0.04	4.448	48.05	2.18	0.036	0.69	12.9	142.	24.2
3FGL J0935.1-1736	143.78	-17.6	0.05	0.05	250.49	24.69	0.04	6.844	33.44	1.74	0.014	0.27	5.13	56.4	32.9

[a] *In units of* 10^{-10} *erg* s^{-1} cm^{-2}

This table continues in the next page

This table continues from the previous page

Gamma-ray source	ra [deg]	dec [deg]	s_{max} [deg]	s_{min} [deg]	l [deg]	b [deg]	G_{100} [(a)]	$signif_{avg}$	$\mathcal{V}$	α_γ	$n_{punt\,P}$	$n_{punt\,L}$	$n_{punt\,C}$	$n_{punt\,K}$	h_{trans} [deg]
3FGL J0312.7+2011	48.190	20.18	0.07	0.05	162.52	-31.6	0.04	6.877	44.40	1.71	0.019	0.36	6.85	75.4	70.6
3FGL J1809.0+3517	272.27	35.28	0.09	0.08	61.983	23.38	0.04	5.438	38.00	2.44	0.039	0.74	13.8	152.	85.7
3FGL J0725.7-0550	111.44	-5.84	0.05	0.05	222.07	4.916	0.04	5.993	47.53	1.85	0.014	0.26	4.99	54.9	44.6
3FGL J2228.5-1636	337.14	-16.6	0.10	0.09	43.120	-55.3	0.04	5.734	49.62	2.50	0.046	0.87	16.2	179.	33.9
3FGL J2209.8-0450	332.46	-4.84	0.08	0.07	55.685	-45.5	0.04	6.460	45.62	1.26	0.030	0.57	10.7	118.	45.6
3FGL J0557.7-0720	89.449	-7.34	0.07	0.05	213.45	-15.2	0.04	4.743	33.05	2.14	0.019	0.37	6.94	76.4	43.1
3FGL J0031.6+0938	7.9225	9.647	0.09	0.08	114.84	-52.9	0.04	5.066	28.81	2.65	0.040	0.76	14.3	158.	60.1
3FGL J2358.5+3827	359.63	38.45	0.10	0.07	111.68	-23.2	0.04	5.892	52.31	2.07	0.036	0.68	12.7	140.	88.9
3FGL J1117.7+0217	169.43	2.283	0.08	0.07	256.86	56.53	0.04	6.076	55.40	2.15	0.033	0.62	11.6	128.	52.7
3FGL J0158.6+0102	29.673	1.041	0.07	0.06	155.51	-57.5	0.04	5.737	44.21	2.55	0.023	0.43	8.11	89.2	51.5
3FGL J0348.4+6039	57.105	60.66	0.11	0.08	142.99	4.884	0.04	4.530	39.29	1.88	0.045	0.85	15.8	174.	68.8
3FGL J2014.5+5246	303.64	52.76	0.08	0.07	87.889	9.900	0.04	4.388	49.03	2.42	0.028	0.53	9.93	109.	76.7
3FGL J2006.6+0150	301.65	1.846	0.06	0.06	43.443	-15.7	0.04	5.517	30.06	1.87	0.020	0.39	7.30	80.4	52.3
3FGL J1312.3+8513	198.09	85.22	0.09	0.08	122.42	31.88	0.04	5.867	28.95	2.56	0.040	0.76	14.2	156.	44.2
3FGL J0818.0+3237	124.52	32.63	0.08	0.06	189.56	31.50	0.04	6.585	56.42	2.18	0.026	0.50	9.38	103.	83.1
3FGL J2229.1+2255	337.28	22.92	0.05	0.05	85.032	-29.2	0.04	6.497	44.21	2.23	0.012	0.23	4.36	47.9	73.4
3FGL J1223.3+0818	185.84	8.313	0.09	0.08	282.18	70.04	0.04	6.417	40.27	1.98	0.038	0.71	13.4	147.	58.8
3FGL J1702.1-2524	255.53	-25.4	0.08	0.06	357.49	9.984	0.04	4.137	24.93	1.75	0.027	0.51	9.63	105.	25.0
3FGL J2223.3+0103	335.83	1.051	0.08	0.06	65.216	-44.5	0.04	6.337	41.57	1.80	0.027	0.50	9.50	104.	51.5
3FGL J2303.7+5555	345.94	55.91	0.05	0.05	108.20	-3.84	0.03	5.608	37.93	1.75	0.013	0.26	4.87	53.6	73.5
3FGL J1922.2+2313	290.56	23.22	0.07	0.05	57.022	4.022	0.03	4.682	43.62	1.62	0.018	0.35	6.66	73.3	73.7
3FGL J1146.1-0640	176.54	-6.68	0.09	0.07	275.53	52.68	0.03	5.999	33.63	1.92	0.035	0.66	12.3	136.	43.8
3FGL J1351.8-1524	207.96	-15.4	0.08	0.08	323.74	45.01	0.03	4.404	53.03	2.40	0.036	0.68	12.7	140.	35.1
3FGL J1748.0+2701	267.01	27.02	0.09	0.07	51.834	25.06	0.03	5.071	41.67	2.27	0.036	0.69	12.9	142.	77.5
3FGL J1209.9+7607	182.47	76.12	0.08	0.07	126.20	40.73	0.03	7.355	41.26	2.39	0.031	0.58	10.9	120.	53.3
3FGL J0937.9-1435	144.48	-14.5	0.06	0.06	248.50	27.20	0.03	6.048	50.74	1.88	0.020	0.38	7.23	79.6	35.9
3FGL J0032.5+3912	8.1464	39.21	0.08	0.08	118.95	-23.5	0.03	4.954	35.19	2.56	0.035	0.66	12.4	136.	89.7
3FGL J0221.2+2518	35.320	25.30	0.09	0.08	147.33	-33.2	0.03	5.522	38.03	1.93	0.036	0.69	12.9	142.	75.8
3FGL J1200.9-1432	180.24	-14.5	0.10	0.08	285.02	46.56	0.03	4.686	54.38	2.25	0.046	0.87	16.2	179.	35.9
3FGL J2358.6-1809	359.66	-18.1	0.07	0.06	66.603	-74.8	0.03	6.513	48.80	1.81	0.022	0.41	7.82	86.1	32.3
3FGL J1550.4+6027	237.62	60.46	0.05	0.05	93.475	45.09	0.03	7.712	44.80	1.84	0.014	0.27	5.08	55.9	69.0
3FGL J1112.1+0500	168.03	5.009	0.06	0.05	251.58	57.61	0.03	5.299	43.75	2.09	0.018	0.35	6.63	73.0	55.5
3FGL J2025.1-2858	306.27	-28.9	0.09	0.07	14.174	-32.0	0.03	4.546	32.87	2.18	0.034	0.65	12.1	133.	21.5
3FGL J1934.2+6002	293.55	60.03	0.07	0.05	91.826	18.21	0.03	6.571	35.67	2.14	0.019	0.36	6.87	75.6	69.4
3FGL J1220.0-2502	185.01	-25.0	0.09	0.08	293.98	37.28	0.03	4.490	51.54	2.25	0.037	0.70	13.1	144.	25.4
3FGL J0931.8+6739	142.96	67.65	0.08	0.06	145.16	39.77	0.03	6.855	44.00	2.16	0.026	0.49	9.31	102.	61.8
3FGL J1944.8+4300	296.22	43.00	0.09	0.08	76.807	9.241	0.03	4.254	39.74	2.01	0.041	0.77	14.4	158.	86.4
3FGL J2104.7+2113	316.19	21.22	0.07	0.06	68.447	-16.9	0.03	4.985	34.31	2.05	0.025	0.47	8.95	98.5	71.7
3FGL J1601.9+2306	240.48	23.11	0.11	0.09	38.537	46.93	0.03	7.783	47.04	2.14	0.048	0.91	17.0	187.	73.6

[a] *In units of* 10^{-10} *erg* s^{-1} cm^{-2}

This table continues in the next page

This table continues from the previous page

Gamma-ray source	ra [deg]	dec [deg]	s_{max} [deg]	s_{min} [deg]	l [deg]	b [deg]	G_{100} [(a)]	$signif_{avg}$	$\mathcal{V}$	α_γ	$n_{punt\,P}$	$n_{punt\,L}$	$n_{punt\,C}$	$n_{punt\,K}$	h_{trans} [deg]
3FGL J0658.8+2318	104.72	23.31	0.10	0.09	192.68	11.94	0.03	4.393	42.82	2.29	0.046	0.87	16.3	179.	73.8
3FGL J0936.3-2114	144.10	-21.2	0.07	0.06	253.62	22.43	0.03	5.669	46.87	1.84	0.024	0.45	8.46	93.1	29.2
3FGL J0516.6+1012	79.170	10.20	0.08	0.06	192.37	-15.7	0.03	4.299	36.38	1.99	0.024	0.46	8.66	95.3	60.7
3FGL J0603.3+2042	90.839	20.71	0.06	0.05	189.12	-0.69	0.03	4.371	24.92	1.49	0.019	0.36	6.77	74.5	71.2
3FGL J0708.7+1747	107.19	17.79	0.06	0.05	198.79	11.73	0.03	5.428	53.51	1.83	0.017	0.32	6.06	66.7	68.3
3FGL J1541.6+1414	235.40	14.23	0.08	0.07	23.676	48.39	0.03	4.865	38.18	1.97	0.029	0.56	10.4	115.	64.7
3FGL J1549.9-3044	237.47	-30.7	0.06	0.06	342.36	18.14	0.03	4.960	35.25	1.43	0.019	0.37	6.94	76.4	19.7
3FGL J1039.5+7324	159.88	73.40	0.10	0.08	134.73	40.55	0.03	5.601	62.39	2.09	0.042	0.79	14.8	163.	56.0
3FGL J0006.2+0135	1.5718	1.585	0.09	0.07	100.40	-59.2	0.03	5.521	45.56	2.18	0.035	0.66	12.4	136.	52.0
3FGL J0312.7-2222	48.175	-22.3	0.05	0.05	212.36	-57.6	0.03	6.911	35.81	1.62	0.014	0.26	4.92	54.2	28.1
3FGL J1119.8-2647	169.97	-26.7	0.08	0.07	278.83	31.76	0.03	5.555	54.07	1.83	0.028	0.52	9.89	108.	23.7
3FGL J0049.0+4224	12.253	42.41	0.04	0.04	122.45	-20.4	0.03	6.947	35.60	1.76	0.009	0.17	3.26	35.9	87.0
3FGL J1821.9+6636	275.47	66.60	0.09	0.06	96.535	27.63	0.03	6.524	32.86	2.04	0.029	0.55	10.3	114.	62.8
3FGL J0952.8+0711	148.21	7.199	0.07	0.05	229.72	43.26	0.03	5.812	39.52	1.69	0.021	0.39	7.37	81.1	57.7
3FGL J2224.4+0351	336.10	3.859	0.07	0.05	68.337	-42.9	0.03	5.843	34.30	1.59	0.018	0.34	6.53	71.9	54.3
3FGL J1027.8+8253	156.96	82.89	0.10	0.09	127.87	32.79	0.03	6.223	41.79	2.07	0.046	0.86	16.1	178.	46.5
3FGL J0342.8+1321	55.710	13.36	0.07	0.06	174.19	-31.9	0.03	4.246	38.95	1.90	0.023	0.44	8.40	92.5	63.8
3FGL J0731.8-3010	112.97	-30.1	0.05	0.04	244.19	-5.39	0.03	4.637	32.20	1.66	0.011	0.22	4.13	45.5	20.3
3FGL J1810.7+5335	272.68	53.58	0.09	0.07	81.776	27.40	0.03	5.592	41.36	1.78	0.036	0.69	12.9	142.	75.9
3FGL J0848.5+7018	132.13	70.30	0.08	0.07	144.01	35.16	0.03	6.324	54.54	2.01	0.030	0.57	10.7	118.	59.1
3FGL J0813.5-0356	123.38	-3.93	0.08	0.07	226.22	16.26	0.03	5.173	32.12	1.66	0.031	0.59	11.1	122.	46.5
3FGL J1411.4-0724	212.85	-7.41	0.07	0.06	335.07	50.39	0.03	4.717	37.25	1.89	0.021	0.41	7.69	84.6	43.0
3FGL J2321.3+5113	350.34	51.22	0.08	0.08	108.87	-9.17	0.03	4.332	39.18	2.01	0.034	0.64	12.1	133.	78.2
3FGL J1528.1-2904	232.03	-29.0	0.08	0.05	339.61	22.42	0.02	4.252	40.38	1.69	0.023	0.44	8.23	90.6	21.4
3FGL J0004.2+0843	1.0574	8.727	0.08	0.08	103.59	-52.3	0.02	4.716	45.33	2.05	0.037	0.69	13.0	143.	59.2
3FGL J1234.7-0437	188.69	-4.62	0.12	0.08	295.08	57.99	0.02	4.872	47.67	1.64	0.047	0.89	16.6	182.	45.8
3FGL J0020.9+0323	5.2311	3.395	0.05	0.05	108.19	-58.6	0.02	5.734	54.41	1.63	0.015	0.28	5.35	58.9	53.9
3FGL J0506.9+0321	76.735	3.361	0.09	0.06	197.19	-21.3	0.02	4.607	33.11	1.80	0.030	0.56	10.6	116.	53.8
3FGL J2015.3-1431	303.84	-14.5	0.06	0.06	28.806	-25.0	0.02	4.791	33.03	1.77	0.019	0.37	6.94	76.4	35.9
3FGL J0234.2-0629	38.564	-6.49	0.06	0.06	177.42	-58.0	0.02	5.728	35.25	1.81	0.019	0.36	6.89	75.9	44.0
3FGL J2309.0+5428	347.25	54.47	0.08	0.07	108.32	-5.46	0.02	4.580	34.10	1.69	0.028	0.52	9.86	108.	75.0
3FGL J1155.3-1112	178.82	-11.2	0.05	0.04	281.53	49.32	0.02	5.357	34.72	1.53	0.011	0.22	4.11	45.3	39.3
3FGL J2300.0+4053	345.02	40.89	0.05	0.05	101.24	-17.2	0.02	5.243	36.24	1.51	0.015	0.28	5.27	58.0	88.5
3FGL J1105.7+4427	166.42	44.45	0.07	0.07	166.68	62.64	0.02	5.308	28.52	2.40	0.027	0.52	9.72	106.	85.0
3FGL J2024.8-2331	306.21	-23.5	0.08	0.07	20.240	-30.3	0.02	4.208	37.63	1.94	0.028	0.53	9.96	109.	26.9
3FGL J0239.0+2555	39.767	25.92	0.08	0.07	151.27	-30.9	0.02	4.288	26.96	2.06	0.033	0.62	11.7	128.	76.4
3FGL J0017.1+1445	4.2937	14.76	0.08	0.08	110.67	-47.2	0.02	4.795	36.14	1.88	0.032	0.61	11.5	126.	65.2
3FGL J2043.6+0001	310.90	0.028	0.10	0.08	46.611	-24.7	0.02	4.259	41.63	1.68	0.041	0.77	14.5	159.	50.5
3FGL J1250.2-0233	192.56	-2.56	0.07	0.06	302.34	60.30	0.02	5.120	26.46	1.09	0.023	0.44	8.35	91.8	47.9

[a] *In units of* 10^{-10} *erg* s^{-1} cm^{-2}

This table continues in the next page

This table continues from the previous page

Gamma-ray source	ra [deg]	dec [deg]	s_{max} [deg]	s_{min} [deg]	l [deg]	b [deg]	G_{100} [(a)]	$signif_{avg}$	$\mathcal{V}$	α_γ	$n_{punt\,P}$	$n_{punt\,L}$	$n_{punt\,C}$	$n_{punt\,K}$	h_{trans} [deg]
3FGL J2145.5+1007	326.37	10.13	0.06	0.06	66.047	-31.5	0.02	5.198	38.22	1.55	0.019	0.36	6.81	74.9	60.6
3FGL J0359.7+7649	59.935	76.83	0.07	0.06	133.02	17.81	0.02	4.609	54.20	2.16	0.021	0.39	7.40	81.4	52.6
3FGL J0251.1-1829	42.797	-18.4	0.09	0.08	201.86	-61.1	0.02	4.791	37.67	1.61	0.036	0.69	12.9	142.	32.0
3FGL J2244.6+2503	341.16	25.05	0.09	0.07	89.763	-29.5	0.02	4.341	41.65	1.91	0.033	0.63	11.9	130.	75.5
3FGL J0216.0+0300	34.013	3.016	0.09	0.07	160.32	-53.5	0.02	4.456	37.60	2.01	0.034	0.64	12.0	132.	53.5
3FGL J2030.5-1439	307.62	-14.6	0.07	0.06	30.304	-28.4	0.02	4.441	39.49	1.86	0.023	0.44	8.26	90.9	35.8
3FGL J1525.8-0834	231.47	-8.57	0.07	0.06	354.76	38.28	0.02	4.157	42.68	1.64	0.024	0.46	8.70	95.7	41.9
3FGL J0430.1-3103	67.542	-31.0	0.10	0.09	231.40	-42.5	0.02	4.854	44.12	1.97	0.047	0.89	16.7	184.	19.4
3FGL J2142.7+1957	325.68	19.95	0.06	0.06	73.733	-24.3	0.02	4.440	37.63	2.00	0.019	0.37	6.92	76.1	70.4
3FGL J1225.4-3448	186.35	-34.8	0.05	0.05	296.90	27.75	0.02	4.830	33.92	1.75	0.014	0.26	4.91	54.1	15.7
3FGL J0527.3+6647	81.835	66.78	0.08	0.06	145.56	17.04	0.02	4.959	36.95	1.85	0.027	0.51	9.54	105.	62.7
3FGL J0351.0-2816	57.769	-28.2	0.08	0.08	225.37	-50.4	0.02	4.605	38.43	2.04	0.032	0.61	11.5	127.	22.2
3FGL J1222.7+7952	185.68	79.86	0.05	0.05	124.51	37.17	0.02	5.462	46.81	1.73	0.013	0.26	4.86	53.4	49.6
3FGL J0930.7+5133	142.68	51.55	0.10	0.08	165.73	45.36	0.02	4.744	32.83	2.06	0.042	0.80	15.0	165.	77.9
3FGL J1211.8+6413	182.97	64.22	0.09	0.08	129.95	52.36	0.02	4.534	37.72	2.43	0.041	0.77	14.4	159.	65.2

[a] *In units of* 10^{-10} *erg* s^{-1} cm^{-2}

This table is concluded from previous page

Table 11: *Sample of 326 gamma-ray sources, selected from 1009 unidentified gamma-ray sources in the 3FGL catalog, sorted by right ascension (ra).*

Gamma-ray source	ra [deg]	dec [deg]	s_{max} [deg]	s_{min} [deg]	l [deg]	b [deg]	G_{100} [(a)]	$signif_{avg}$	$\mathcal{V}$	α_γ	$n_{punt\,P}$	$n_{punt\,L}$	$n_{punt\,C}$	$n_{punt\,K}$	h_{trans} [deg]
3FGL J0000.1+6545	0.0377	65.75	0.10	0.07	117.69	3.402	0.13	6.813	40.75	2.41	0.038	0.72	13.4	148.	63.7
3FGL J0002.6+6218	0.6745	62.30	0.06	0.05	117.30	-0.03	0.18	17.97	48.02	2.08	0.015	0.29	5.55	61.0	67.1
3FGL J0003.5+5721	0.8903	57.35	0.08	0.07	116.48	-4.91	0.05	5.380	31.12	2.18	0.030	0.58	10.8	119.	72.1
3FGL J0004.2+6757	1.0551	67.95	0.10	0.08	118.50	5.494	0.11	6.005	34.81	2.49	0.043	0.82	15.4	169.	61.5
3FGL J0004.2+0843	1.0574	8.727	0.08	0.08	103.59	-52.3	0.02	4.716	45.33	2.05	0.037	0.69	13.0	143.	59.2
3FGL J0006.2+0135	1.5718	1.585	0.09	0.07	100.40	-59.2	0.03	5.521	45.56	2.18	0.035	0.66	12.4	136.	52.0
3FGL J0017.1+1445	4.2937	14.76	0.08	0.08	110.67	-47.2	0.02	4.795	36.14	1.88	0.032	0.61	11.5	126.	65.2
3FGL J0020.9+0323	5.2311	3.395	0.05	0.05	108.19	-58.6	0.02	5.734	54.41	1.63	0.015	0.28	5.35	58.9	53.9
3FGL J0031.6+0938	7.9225	9.647	0.09	0.08	114.84	-52.9	0.04	5.066	28.81	2.65	0.040	0.76	14.3	158.	60.1
3FGL J0032.5+3912	8.1464	39.21	0.08	0.08	118.95	-23.5	0.03	4.954	35.19	2.56	0.035	0.66	12.4	136.	89.7
3FGL J0039.3+6256	9.8342	62.94	0.05	0.05	121.55	0.102	0.09	11.99	57.84	1.87	0.014	0.27	5.18	57.0	66.5
3FGL J0049.0+4224	12.253	42.41	0.04	0.04	122.45	-20.4	0.03	6.947	35.60	1.76	0.009	0.17	3.26	35.9	87.0
3FGL J0051.6+6445	12.903	64.75	0.07	0.05	122.95	1.887	0.08	5.553	44.15	2.27	0.020	0.38	7.20	79.2	64.7
3FGL J0102.1+0943	15.540	9.728	0.08	0.06	127.33	-53.0	0.05	7.093	41.74	2.06	0.026	0.50	9.38	103.	60.2
3FGL J0133.3+5930	23.336	59.51	0.10	0.08	128.23	-2.92	0.04	4.348	42.57	2.21	0.044	0.83	15.5	171.	69.9
3FGL J0158.6+0102	29.673	1.041	0.07	0.06	155.51	-57.5	0.04	5.737	44.21	2.55	0.023	0.43	8.11	89.2	51.5
3FGL J0212.1+5320	33.037	53.33	0.03	0.03	134.92	-7.64	0.17	25.06	51.47	1.95	0.005	0.10	1.97	21.7	76.1
3FGL J0216.0+0300	34.013	3.016	0.09	0.07	160.32	-53.5	0.02	4.456	37.60	2.01	0.034	0.64	12.0	132.	53.5
3FGL J0221.2+2518	35.320	25.30	0.09	0.08	147.33	-33.2	0.03	5.522	38.03	1.93	0.036	0.69	12.9	142.	75.8
3FGL J0221.8+6138c	35.472	61.64	0.10	0.07	133.45	0.631	0.14	4.666	44.20	2.41	0.038	0.72	13.4	148.	67.8
3FGL J0223.6+6204	35.906	62.08	0.03	0.03	133.49	1.115	0.39	12.87	41.77	2.80	0.006	0.12	2.36	25.9	67.4
3FGL J0225.8+6159	36.472	61.98	0.09	0.08	133.77	1.120	0.26	8.304	46.68	2.88	0.037	0.70	13.2	145.	67.5
3FGL J0234.2-0629	38.564	-6.49	0.06	0.06	177.42	-58.0	0.02	5.728	35.25	1.81	0.019	0.36	6.89	75.9	44.0
3FGL J0235.7+5647	38.927	56.78	0.10	0.09	136.88	-3.23	0.11	8.243	60.79	2.60	0.050	0.94	17.5	193.	72.7
3FGL J0238.0+5237	39.504	52.62	0.05	0.05	138.84	-6.92	0.11	14.99	36.58	2.13	0.014	0.27	5.13	56.4	76.8
3FGL J0239.0+2555	39.767	25.92	0.08	0.07	151.27	-30.9	0.02	4.288	26.96	2.06	0.033	0.62	11.7	128.	76.4
3FGL J0239.4+1326	39.868	13.44	0.07	0.06	159.19	-41.6	0.05	6.577	51.05	1.99	0.024	0.46	8.68	95.5	63.9
3FGL J0248.4+5130	42.110	51.51	0.04	0.03	140.78	-7.25	0.11	11.91	33.03	2.06	0.007	0.14	2.64	29.1	77.9
3FGL J0251.1-1829	42.797	-18.4	0.09	0.08	201.86	-61.1	0.02	4.791	37.67	1.61	0.036	0.69	12.9	142.	32.0
3FGL J0258.9+0552	44.739	5.875	0.09	0.07	170.73	-44.8	0.06	7.956	38.93	2.12	0.034	0.65	12.2	134.	56.3
3FGL J0307.3+4916	46.843	49.27	0.03	0.02	144.53	-7.81	0.14	14.80	53.47	2.09	0.004	0.08	1.53	16.8	80.2
3FGL J0312.1-0921	48.040	-9.35	0.08	0.08	191.51	-52.3	0.05	10.92	47.55	1.87	0.035	0.65	12.3	135.	41.1
3FGL J0312.7-2222	48.175	-22.3	0.05	0.05	212.36	-57.6	0.03	6.911	35.81	1.62	0.014	0.26	4.92	54.2	28.1
3FGL J0312.7+2011	48.190	20.18	0.07	0.05	162.52	-31.6	0.04	6.877	44.40	1.71	0.019	0.36	6.85	75.4	70.6
3FGL J0318.1+0252	49.536	2.869	0.08	0.06	178.44	-43.6	0.05	12.75	50.21	1.71	0.026	0.49	9.15	100.	53.3
3FGL J0330.6+0437	52.665	4.625	0.10	0.08	179.52	-40.1	0.06	7.381	61.66	2.23	0.043	0.81	15.3	168.	55.1
3FGL J0336.1+7500	54.043	75.01	0.04	0.04	133.10	15.50	0.09	17.75	33.84	1.94	0.010	0.19	3.72	40.9	54.4
3FGL J0340.4+5302	55.100	53.04	0.10	0.09	146.78	-1.81	0.36	22.30	46.59	2.36	0.048	0.91	17.1	188.	76.4

[a] *In units of* 10^{-10} *erg* s^{-1} cm^{-2}

This table continues in the next page

This table continues from the previous page

Gamma-ray source	ra [deg]	dec [deg]	s_{max} [deg]	s_{min} [deg]	l [deg]	b [deg]	G_{100} [(a)]	$signif_{avg}$	$\mathcal{V}$	α_γ	$n_{punt\,P}$	$n_{punt\,L}$	$n_{punt\,C}$	$n_{punt\,K}$	h_{trans} [deg]
3FGL J0342.3+3148c	55.576	31.80	0.10	0.07	160.34	-18.3	0.11	6.768	47.92	2.27	0.039	0.73	13.8	152.	82.3
3FGL J0342.8+1321	55.710	13.36	0.07	0.06	174.19	-31.9	0.03	4.246	38.95	1.90	0.023	0.44	8.40	92.5	63.8
3FGL J0348.4+6039	57.105	60.66	0.11	0.08	142.99	4.884	0.04	4.530	39.29	1.88	0.045	0.85	15.8	174.	68.8
3FGL J0351.0-2816	57.769	-28.2	0.08	0.08	225.37	-50.4	0.02	4.605	38.43	2.04	0.032	0.61	11.5	127.	22.2
3FGL J0359.5+5413	59.881	54.22	0.04	0.04	148.25	0.871	0.24	19.16	33.63	2.02	0.007	0.14	2.78	30.6	75.2
3FGL J0359.7+7649	59.935	76.83	0.07	0.06	133.02	17.81	0.02	4.609	54.20	2.16	0.021	0.39	7.40	81.4	52.6
3FGL J0419.1+6636	64.778	66.60	0.05	0.04	141.53	11.56	0.15	14.46	49.15	2.31	0.012	0.24	4.50	49.5	62.8
3FGL J0425.8+5600	66.451	56.01	0.06	0.05	149.76	4.750	0.08	6.336	51.67	2.34	0.015	0.29	5.50	60.5	73.4
3FGL J0426.7+5437	66.681	54.61	0.07	0.06	150.86	3.873	0.21	14.19	51.83	2.46	0.023	0.43	8.14	89.6	74.8
3FGL J0430.1-3103	67.542	-31.0	0.10	0.09	231.40	-42.5	0.02	4.854	44.12	1.97	0.047	0.89	16.7	184.	19.4
3FGL J0447.1-2540	71.794	-25.6	0.10	0.09	225.60	-37.6	0.05	7.138	38.69	2.50	0.050	0.95	17.8	195.	24.8
3FGL J0451.7+5722	72.940	57.37	0.06	0.06	151.11	8.319	0.06	6.039	28.32	2.48	0.019	0.37	6.99	76.9	72.1
3FGL J0506.9+0321	76.735	3.361	0.09	0.06	197.19	-21.3	0.02	4.607	33.11	1.80	0.030	0.56	10.6	116.	53.8
3FGL J0516.6+1012	79.170	10.20	0.08	0.06	192.37	-15.7	0.03	4.299	36.38	1.99	0.024	0.46	8.66	95.3	60.7
3FGL J0523.3-2528	80.839	-25.4	0.04	0.04	228.20	-29.8	0.19	26.14	50.15	2.15	0.008	0.15	2.90	31.9	25.0
3FGL J0524.4+2839	81.124	28.65	0.06	0.04	177.73	-4.04	0.10	9.199	53.24	2.12	0.013	0.25	4.69	51.6	79.1
3FGL J0526.4+2247	81.609	22.79	0.05	0.04	182.87	-6.93	0.08	6.019	56.72	2.40	0.013	0.24	4.61	50.7	73.3
3FGL J0527.3+6647	81.835	66.78	0.08	0.06	145.56	17.04	0.02	4.959	36.95	1.85	0.027	0.51	9.54	105.	62.7
3FGL J0535.7-0617c	83.934	-6.29	0.09	0.08	209.92	-19.6	0.12	6.202	41.18	2.39	0.042	0.80	14.9	164.	44.2
3FGL J0537.4+3604c	84.350	36.07	0.08	0.06	173.02	2.301	0.08	4.531	28.44	2.27	0.025	0.48	9.05	99.5	86.5
3FGL J0538.9+1646	84.748	16.77	0.05	0.04	189.59	-7.65	0.05	5.920	45.33	1.89	0.013	0.25	4.78	52.6	67.2
3FGL J0540.0+1208	85.002	12.14	0.07	0.06	193.73	-9.83	0.04	5.346	48.38	2.10	0.022	0.42	7.88	86.8	62.6
3FGL J0545.6+6019	86.415	60.32	0.05	0.04	152.49	15.74	0.07	15.39	35.95	1.79	0.011	0.21	4.10	45.2	69.1
3FGL J0557.7-0720	89.449	-7.34	0.07	0.05	213.45	-15.2	0.04	4.743	33.05	2.14	0.019	0.37	6.94	76.4	43.1
3FGL J0559.8+3042	89.962	30.71	0.05	0.04	180.03	3.561	0.04	5.908	38.99	1.71	0.010	0.20	3.84	42.2	81.2
3FGL J0603.3+2042	90.839	20.71	0.06	0.05	189.12	-0.69	0.03	4.371	24.92	1.49	0.019	0.36	6.77	74.5	71.2
3FGL J0605.0-0000	91.271	-0.00	0.05	0.04	207.59	-10.3	0.07	8.132	51.87	2.00	0.012	0.23	4.39	48.4	50.4
3FGL J0605.9+2039c	91.476	20.65	0.10	0.08	189.47	-0.20	0.17	6.884	50.56	2.35	0.043	0.81	15.2	167.	71.1
3FGL J0609.2+2051c	92.318	20.86	0.06	0.06	189.67	0.587	0.11	4.960	33.28	2.27	0.020	0.38	7.25	79.8	71.3
3FGL J0609.7-1841	92.426	-18.6	0.10	0.09	225.46	-17.3	0.07	8.551	61.79	2.29	0.045	0.85	15.9	175.	31.8
3FGL J0611.5+1957	92.899	19.96	0.09	0.08	190.72	0.628	0.15	6.924	46.41	2.38	0.040	0.75	14.1	155.	70.4
3FGL J0619.4+2242	94.874	22.70	0.10	0.06	189.18	3.552	0.15	5.485	51.68	2.01	0.035	0.67	12.5	138.	73.2
3FGL J0628.4+2429	97.123	24.49	0.11	0.09	188.54	6.207	0.05	4.275	42.02	2.20	0.049	0.93	17.3	191.	75.0
3FGL J0634.1+0424	98.528	4.406	0.10	0.08	207.03	-1.83	0.46	21.06	42.87	2.75	0.046	0.87	16.4	180.	54.9
3FGL J0637.5+0418	99.383	4.315	0.08	0.07	207.50	-1.11	0.17	8.777	71.36	3.03	0.033	0.62	11.7	128.	54.8
3FGL J0644.6+6035	101.15	60.59	0.06	0.05	155.04	22.59	0.07	11.11	60.28	2.27	0.018	0.34	6.36	69.9	68.9
3FGL J0647.6+0032	101.91	0.534	0.08	0.07	212.02	-0.59	0.20	11.19	49.28	2.45	0.029	0.55	10.3	113.	51.0
3FGL J0658.8+2318	104.72	23.31	0.10	0.09	192.68	11.94	0.03	4.393	42.82	2.29	0.046	0.87	16.3	179.	73.8
3FGL J0659.2-0439c	104.80	-4.65	0.10	0.08	217.95	-0.39	0.11	5.624	41.52	2.40	0.040	0.77	14.3	158.	45.8

[a] *In units of* 10^{-10} *erg* s^{-1} cm^{-2}

This table continues in the next page

This table continues from the previous page

Gamma-ray source	ra [deg]	dec [deg]	s_{max} [deg]	s_{min} [deg]	l [deg]	b [deg]	G_{100} [(a)]	$signif_{avg}$	$\mathcal{V}$	α_γ	$n_{punt\,P}$	$n_{punt\,L}$	$n_{punt\,C}$	$n_{punt\,K}$	h_{trans} [deg]
3FGL J0708.7+1747	107.19	17.79	0.06	0.05	198.79	11.73	0.03	5.428	53.51	1.83	0.017	0.32	6.06	66.7	68.3
3FGL J0725.7-0550	111.44	-5.84	0.05	0.05	222.07	4.916	0.04	5.993	47.53	1.85	0.014	0.26	4.99	54.9	44.6
3FGL J0725.8+0212	111.46	2.206	0.08	0.06	214.89	8.666	0.08	9.182	54.32	2.18	0.025	0.47	8.95	98.5	52.7
3FGL J0731.8-3010	112.97	-30.1	0.05	0.04	244.19	-5.39	0.03	4.637	32.20	1.66	0.011	0.22	4.13	45.5	20.3
3FGL J0737.2-3233	114.31	-32.5	0.10	0.08	246.84	-5.53	0.13	12.86	51.33	2.25	0.040	0.75	14.1	156.	17.9
3FGL J0744.1-2523	116.04	-25.3	0.05	0.05	241.33	-0.69	0.23	18.10	61.34	2.08	0.013	0.24	4.65	51.1	25.1
3FGL J0746.4-0225	116.61	-2.42	0.07	0.06	221.48	11.08	0.07	9.604	59.80	2.00	0.021	0.40	7.65	84.2	48.0
3FGL J0747.4-0734	116.86	-7.58	0.08	0.06	226.19	8.819	0.05	5.485	34.82	2.11	0.029	0.55	10.4	114.	42.9
3FGL J0748.8-2208	117.20	-22.1	0.12	0.08	239.04	1.857	0.08	5.874	39.66	2.36	0.051	0.96	18.0	198.	28.3
3FGL J0751.7-2944	117.93	-29.7	0.08	0.08	245.92	-1.43	0.08	5.486	52.25	2.45	0.033	0.62	11.6	127.	20.7
3FGL J0752.6-1629	118.15	-16.4	0.10	0.07	234.62	5.489	0.06	6.479	42.07	2.19	0.039	0.74	13.9	153.	34.0
3FGL J0758.6-1451	119.65	-14.8	0.07	0.07	233.96	7.561	0.07	12.06	38.62	1.98	0.026	0.49	9.32	102.	35.6
3FGL J0802.3-0941	120.59	-9.69	0.06	0.05	229.91	10.97	0.07	8.704	35.88	2.28	0.018	0.34	6.40	70.4	40.8
3FGL J0813.5-0356	123.38	-3.93	0.08	0.07	226.22	16.26	0.03	5.173	32.12	1.66	0.031	0.59	11.1	122.	46.5
3FGL J0818.0+3237	124.52	32.63	0.08	0.06	189.56	31.50	0.04	6.585	56.42	2.18	0.026	0.50	9.38	103.	83.1
3FGL J0838.8-2829	129.70	-28.4	0.05	0.05	250.60	7.800	0.12	13.74	42.93	2.22	0.014	0.26	4.99	55.0	22.0
3FGL J0843.4+6713	130.85	67.21	0.06	0.04	147.79	35.60	0.07	13.16	55.97	1.99	0.014	0.27	5.06	55.7	62.2
3FGL J0848.5+7018	132.13	70.30	0.08	0.07	144.01	35.16	0.03	6.324	54.54	2.01	0.030	0.57	10.7	118.	59.1
3FGL J0855.4+7142	133.86	71.71	0.10	0.09	142.15	35.22	0.06	9.268	76.98	2.57	0.046	0.88	16.4	181.	57.7
3FGL J0921.6+2339	140.41	23.65	0.04	0.04	204.89	42.83	0.05	9.736	58.49	1.97	0.009	0.17	3.28	36.1	74.1
3FGL J0930.7+5133	142.68	51.55	0.10	0.08	165.73	45.36	0.02	4.744	32.83	2.06	0.042	0.80	15.0	165.	77.9
3FGL J0931.8+6739	142.96	67.65	0.08	0.06	145.16	39.77	0.03	6.855	44.00	2.16	0.026	0.49	9.31	102.	61.8
3FGL J0935.1-1736	143.78	-17.6	0.05	0.05	250.49	24.69	0.04	6.844	33.44	1.74	0.014	0.27	5.13	56.4	32.9
3FGL J0936.3-2114	144.10	-21.2	0.07	0.06	253.62	22.43	0.03	5.669	46.87	1.84	0.024	0.45	8.46	93.1	29.2
3FGL J0937.9-1435	144.48	-14.5	0.06	0.06	248.50	27.20	0.03	6.048	50.74	1.88	0.020	0.38	7.23	79.6	35.9
3FGL J0941.0+6151	145.27	61.86	0.07	0.07	151.48	43.24	0.04	9.010	52.87	2.29	0.028	0.53	9.96	109.	67.6
3FGL J0952.8+0711	148.21	7.199	0.07	0.05	229.72	43.26	0.03	5.812	39.52	1.69	0.021	0.39	7.37	81.1	57.7
3FGL J0953.7-1510	148.42	-15.1	0.06	0.06	251.93	29.60	0.05	14.00	40.21	1.81	0.021	0.40	7.56	83.2	35.3
3FGL J1027.8+8253	156.96	82.89	0.10	0.09	127.87	32.79	0.03	6.223	41.79	2.07	0.046	0.86	16.1	178.	46.5
3FGL J1039.5+7324	159.88	73.40	0.10	0.08	134.73	40.55	0.03	5.601	62.39	2.09	0.042	0.79	14.8	163.	56.0
3FGL J1049.7+1548	162.43	15.80	0.08	0.08	228.51	59.61	0.04	7.553	58.39	2.15	0.034	0.64	12.0	132.	66.3
3FGL J1059.3+0224	164.84	2.416	0.10	0.09	250.78	53.53	0.07	6.809	52.37	2.35	0.046	0.87	16.4	180.	52.9
3FGL J1105.7+4427	166.42	44.45	0.07	0.07	166.68	62.64	0.02	5.308	28.52	2.40	0.027	0.52	9.72	106.	85.0
3FGL J1112.1+0500	168.03	5.009	0.06	0.05	251.58	57.61	0.03	5.299	43.75	2.09	0.018	0.35	6.63	73.0	55.5
3FGL J1115.0-0701	168.76	-7.02	0.05	0.05	265.11	48.63	0.06	10.01	86.88	2.10	0.013	0.24	4.65	51.2	43.4
3FGL J1117.7+0217	169.43	2.283	0.08	0.07	256.86	56.53	0.04	6.076	55.40	2.15	0.033	0.62	11.6	128.	52.7
3FGL J1119.8-2647	169.97	-26.7	0.08	0.07	278.83	31.76	0.03	5.555	54.07	1.83	0.028	0.52	9.89	108.	23.7
3FGL J1119.9-2204	169.98	-22.0	0.04	0.03	276.47	36.05	0.16	30.16	62.62	1.81	0.007	0.14	2.77	30.5	28.4
3FGL J1120.6+0713	170.17	7.223	0.07	0.06	251.53	60.68	0.06	13.17	69.98	2.02	0.023	0.44	8.37	92.1	57.7

[a] *In units of* 10^{-10} *erg* s^{-1} cm^{-2}

This table continues in the next page

This table continues from the previous page

Gamma-ray source	ra [deg]	dec [deg]	s_{max} [deg]	s_{min} [deg]	l [deg]	b [deg]	G_{100} [(a)]	$signif_{avg}$	$\mathcal{V}$	α_γ	$n_{punt\,P}$	$n_{punt\,L}$	$n_{punt\,C}$	$n_{punt\,K}$	h_{trans} [deg]
3FGL J1129.0+3758	172.25	37.97	0.06	0.05	175.66	69.59	0.08	10.25	44.75	2.28	0.017	0.32	6.04	66.5	88.4
3FGL J1146.1-0640	176.54	-6.68	0.09	0.07	275.53	52.68	0.03	5.999	33.63	1.92	0.035	0.66	12.3	136.	43.8
3FGL J1155.3-1112	178.82	-11.2	0.05	0.04	281.53	49.32	0.02	5.357	34.72	1.53	0.011	0.22	4.11	45.3	39.3
3FGL J1200.4+0202	180.11	2.041	0.06	0.06	274.81	62.09	0.05	8.817	55.79	2.03	0.021	0.39	7.44	81.8	52.5
3FGL J1200.9-1432	180.24	-14.5	0.10	0.08	285.02	46.56	0.03	4.686	54.38	2.25	0.046	0.87	16.2	179.	35.9
3FGL J1209.9+7607	182.47	76.12	0.08	0.07	126.20	40.73	0.03	7.355	41.26	2.39	0.031	0.58	10.9	120.	53.3
3FGL J1211.8+6413	182.97	64.22	0.09	0.08	129.95	52.36	0.02	4.534	37.72	2.43	0.041	0.77	14.4	159.	65.2
3FGL J1220.0-2502	185.01	-25.0	0.09	0.08	293.98	37.28	0.03	4.490	51.54	2.25	0.037	0.70	13.1	144.	25.4
3FGL J1221.5-0632	185.37	-6.55	0.09	0.07	289.71	55.55	0.09	11.52	52.54	2.24	0.033	0.63	11.8	130.	43.9
3FGL J1222.7+7952	185.68	79.86	0.05	0.05	124.51	37.17	0.02	5.462	46.81	1.73	0.013	0.26	4.86	53.4	49.6
3FGL J1223.3+0818	185.84	8.313	0.09	0.08	282.18	70.04	0.04	6.417	40.27	1.98	0.038	0.71	13.4	147.	58.8
3FGL J1225.4-3448	186.35	-34.8	0.05	0.05	296.90	27.75	0.02	4.830	33.92	1.75	0.014	0.26	4.91	54.1	15.7
3FGL J1225.9+2953	186.49	29.89	0.05	0.04	185.15	83.76	0.08	17.37	58.04	1.94	0.012	0.23	4.48	49.3	80.3
3FGL J1231.6+4825	187.90	48.41	0.09	0.08	131.87	68.36	0.04	5.928	44.38	2.51	0.042	0.79	14.8	163.	81.0
3FGL J1234.7-0437	188.69	-4.62	0.12	0.08	295.08	57.99	0.02	4.872	47.67	1.64	0.047	0.89	16.6	182.	45.8
3FGL J1249.1-2808	192.29	-28.1	0.07	0.06	302.32	34.72	0.05	8.175	49.83	2.06	0.022	0.41	7.81	86.0	22.3
3FGL J1250.2-0233	192.56	-2.56	0.07	0.06	302.34	60.30	0.02	5.120	26.46	1.09	0.023	0.44	8.35	91.8	47.9
3FGL J1312.3+8513	198.09	85.22	0.09	0.08	122.42	31.88	0.04	5.867	28.95	2.56	0.040	0.76	14.2	156.	44.2
3FGL J1315.7-0732	198.94	-7.54	0.05	0.04	313.44	54.82	0.09	12.87	72.48	2.01	0.010	0.19	3.58	39.3	42.9
3FGL J1351.1-2743	207.79	-27.7	0.09	0.08	318.77	33.30	0.04	5.401	48.98	2.38	0.038	0.72	13.6	149.	22.7
3FGL J1351.8-1524	207.96	-15.4	0.08	0.08	323.74	45.01	0.03	4.404	53.03	2.40	0.036	0.68	12.7	140.	35.1
3FGL J1410.9+7406	212.74	74.10	0.04	0.03	115.74	41.89	0.07	15.76	43.48	2.16	0.007	0.14	2.75	30.2	55.3
3FGL J1411.4-0724	212.85	-7.41	0.07	0.06	335.07	50.39	0.03	4.717	37.25	1.89	0.021	0.41	7.69	84.6	43.0
3FGL J1424.3-1753	216.09	-17.8	0.06	0.05	332.12	39.66	0.05	7.301	49.36	2.17	0.018	0.34	6.42	70.7	32.6
3FGL J1458.7-2120	224.68	-21.3	0.10	0.08	338.59	32.57	0.07	7.401	35.35	2.34	0.041	0.77	14.4	159.	29.1
3FGL J1502.2+5553	225.55	55.88	0.07	0.06	92.785	52.89	0.08	12.62	102.7	2.58	0.021	0.40	7.64	84.1	73.6
3FGL J1525.8-0834	231.47	-8.57	0.07	0.06	354.76	38.28	0.02	4.157	42.68	1.64	0.024	0.46	8.70	95.7	41.9
3FGL J1528.1-2904	232.03	-29.0	0.08	0.05	339.61	22.42	0.02	4.252	40.38	1.69	0.023	0.44	8.23	90.6	21.4
3FGL J1532.0-2618	233.01	-26.3	0.09	0.08	342.21	24.06	0.04	4.448	48.05	2.18	0.036	0.69	12.9	142.	24.2
3FGL J1539.2-3324	234.82	-33.4	0.03	0.03	338.75	17.53	0.11	19.23	57.87	1.55	0.006	0.11	2.19	24.1	17.0
3FGL J1541.6+1414	235.40	14.23	0.08	0.07	23.676	48.39	0.03	4.865	38.18	1.97	0.029	0.56	10.4	115.	64.7
3FGL J1544.6-1125	236.17	-11.4	0.07	0.06	356.21	32.98	0.13	10.84	47.47	2.41	0.025	0.47	8.80	96.8	39.0
3FGL J1548.4+1455	237.11	14.92	0.03	0.03	25.632	47.17	0.14	17.25	67.42	2.11	0.007	0.13	2.59	28.5	65.4
3FGL J1549.9-3044	237.47	-30.7	0.06	0.06	342.36	18.14	0.03	4.960	35.25	1.43	0.019	0.37	6.94	76.4	19.7
3FGL J1550.4+6027	237.62	60.46	0.05	0.05	93.475	45.09	0.03	7.712	44.80	1.84	0.014	0.27	5.08	55.9	69.0
3FGL J1553.1+5437	238.29	54.62	0.08	0.08	85.581	47.16	0.04	8.511	56.25	2.25	0.036	0.67	12.6	139.	74.8
3FGL J1601.9+2306	240.48	23.11	0.11	0.09	38.537	46.93	0.03	7.783	47.04	2.14	0.048	0.91	17.0	187.	73.6
3FGL J1625.1-0021	246.27	-0.35	0.03	0.03	13.880	31.83	0.18	28.53	37.31	1.66	0.006	0.12	2.32	25.6	50.1
3FGL J1625.2-2845	246.30	-28.7	0.12	0.08	349.52	14.20	0.08	4.739	52.96	2.52	0.050	0.94	17.6	194.	21.7

[a] *In units of* 10^{-10} *erg* s^{-1} cm^{-2}

This table continues in the next page

This table continues from the previous page

Gamma-ray source	ra [deg]	dec [deg]	s_{max} [deg]	s_{min} [deg]	l [deg]	b [deg]	G_{100} [(a)]	$signif_{avg}$	$\mathcal{V}$	α_γ	$n_{punt\,P}$	$n_{punt\,L}$	$n_{punt\,C}$	$n_{punt\,K}$	h_{trans} [deg]
3FGL J1625.6-2058	246.42	-20.9	0.10	0.09	355.66	19.28	0.10	6.498	39.46	2.54	0.047	0.88	16.5	181.	29.5
3FGL J1626.2-2428c	246.57	-24.4	0.05	0.05	352.99	16.89	0.26	9.404	46.86	2.27	0.013	0.26	4.90	53.9	26.0
3FGL J1627.8+3217	246.96	32.29	0.07	0.06	52.958	43.20	0.06	10.16	33.02	2.13	0.024	0.45	8.46	93.1	82.8
3FGL J1628.1-3344	247.02	-33.7	0.06	0.05	346.19	10.36	0.06	5.556	36.83	2.11	0.015	0.29	5.50	60.5	16.7
3FGL J1628.2-2431c	247.06	-24.5	0.10	0.09	353.26	16.51	0.23	7.913	30.28	2.37	0.044	0.83	15.5	170.	25.9
3FGL J1632.8+3838	248.20	38.64	0.09	0.07	61.741	42.84	0.05	4.755	29.26	2.45	0.034	0.65	12.2	134.	89.1
3FGL J1644.6-0911	251.17	-9.18	0.07	0.07	8.6764	22.87	0.07	4.946	38.50	2.56	0.028	0.52	9.87	108.	41.3
3FGL J1645.7-2149	251.44	-21.8	0.12	0.08	358.09	15.13	0.08	8.848	37.08	2.29	0.049	0.93	17.4	191.	28.6
3FGL J1646.9-1332	251.74	-13.5	0.10	0.07	5.2024	19.89	0.05	4.883	41.95	1.85	0.037	0.70	13.2	145.	36.9
3FGL J1653.6-0158	253.41	-1.98	0.03	0.03	16.618	24.92	0.33	31.94	55.40	2.06	0.005	0.11	2.07	22.7	48.5
3FGL J1659.0-0142	254.77	-1.70	0.09	0.08	17.646	23.90	0.10	8.527	56.58	2.19	0.039	0.74	13.9	153.	48.8
3FGL J1702.1-2524	255.53	-25.4	0.08	0.06	357.49	9.984	0.04	4.137	24.93	1.75	0.027	0.51	9.63	105.	25.0
3FGL J1703.6-2850	255.92	-28.8	0.08	0.07	354.92	7.649	0.05	4.117	26.87	2.22	0.031	0.59	11.2	123.	21.6
3FGL J1704.1+1234	256.03	12.57	0.06	0.06	32.465	29.42	0.09	9.432	47.00	2.58	0.022	0.43	8.05	88.6	63.0
3FGL J1704.4-0528	256.12	-5.47	0.08	0.06	14.913	20.79	0.10	7.911	41.66	2.18	0.026	0.50	9.36	103.	45.0
3FGL J1720.3-0428	260.09	-4.47	0.07	0.07	17.992	17.92	0.05	4.270	53.78	2.08	0.027	0.51	9.60	105.	46.0
3FGL J1720.7+0711	260.19	7.189	0.09	0.07	28.997	23.41	0.11	9.546	44.07	2.35	0.032	0.60	11.3	124.	57.6
3FGL J1722.7-0415	260.69	-4.26	0.11	0.08	18.495	17.51	0.12	6.431	34.02	2.29	0.046	0.87	16.3	180.	46.2
3FGL J1730.6-0357	262.66	-3.95	0.07	0.07	19.803	15.96	0.06	8.330	29.97	1.86	0.026	0.50	9.37	103.	46.5
3FGL J1732.4-2709	263.12	-27.1	0.07	0.06	359.96	3.402	0.18	6.138	51.77	2.37	0.022	0.42	7.92	87.2	23.3
3FGL J1733.5-2811	263.38	-28.1	0.06	0.05	359.21	2.642	0.17	5.154	44.61	2.44	0.018	0.34	6.41	70.5	22.3
3FGL J1734.7-2930	263.69	-29.5	0.09	0.08	358.26	1.700	0.21	8.971	70.28	2.52	0.039	0.74	13.8	152.	21.0
3FGL J1736.0-2701	264.01	-27.0	0.08	0.08	0.5107	2.801	0.18	8.272	38.45	2.55	0.033	0.62	11.6	128.	23.4
3FGL J1739.9-3124c	264.99	-31.4	0.08	0.05	357.25	-0.25	0.26	5.092	48.21	2.28	0.024	0.46	8.62	94.9	19.1
3FGL J1740.5-2843	265.12	-28.7	0.06	0.05	359.59	1.068	0.67	15.12	46.42	2.39	0.017	0.32	5.99	65.9	21.7
3FGL J1740.5-2726	265.13	-27.4	0.09	0.08	0.6765	1.733	0.38	12.75	43.15	2.32	0.036	0.69	12.9	142.	23.0
3FGL J1740.5-2642	265.13	-26.7	0.09	0.07	1.3043	2.122	0.16	8.788	33.42	2.30	0.033	0.63	11.9	131.	23.7
3FGL J1740.8-1933	265.21	-19.5	0.10	0.08	7.4322	5.826	0.08	4.276	49.45	2.21	0.045	0.84	15.8	173.	30.9
3FGL J1742.6-3321	265.66	-33.3	0.06	0.06	355.90	-1.77	0.32	15.31	48.24	2.36	0.019	0.37	7.01	77.2	17.1
3FGL J1744.7-3043	266.18	-30.7	0.07	0.05	358.37	-0.76	0.38	6.583	58.49	2.36	0.019	0.37	6.97	76.7	19.7
3FGL J1745.3-2903c	266.34	-29.0	0.02	0.02	359.86	-0.02	2.30	20.65	48.41	2.36	0.002	0.04	0.84	9.32	21.4
3FGL J1747.0-3506	266.75	-35.1	0.09	0.07	354.87	-3.45	0.27	11.69	64.48	2.66	0.032	0.61	11.4	126.	15.4
3FGL J1747.0-2828	266.77	-28.4	0.04	0.03	0.5571	-0.04	1.45	20.26	90.61	2.04	0.006	0.12	2.42	26.6	22.0
3FGL J1747.7-2904	266.94	-29.0	0.06	0.06	0.1261	-0.47	0.84	6.975	65.34	2.51	0.020	0.37	7.08	78.0	21.4
3FGL J1748.0+2701	267.01	27.02	0.09	0.07	51.834	25.06	0.03	5.071	41.67	2.27	0.036	0.69	12.9	142.	77.5
3FGL J1748.3-2815c	267.09	-28.2	0.03	0.02	0.8925	-0.16	0.42	15.10	34.06	2.27	0.004	0.07	1.46	16.1	22.2
3FGL J1749.2-2911	267.31	-29.1	0.08	0.05	0.1925	-0.81	0.45	11.72	41.77	2.57	0.021	0.41	7.70	84.8	21.3
3FGL J1749.7-0305	267.44	-3.08	0.08	0.07	22.979	12.21	0.12	7.365	47.41	2.42	0.032	0.61	11.5	126.	47.4
3FGL J1754.0-2930	268.50	-29.5	0.10	0.08	0.4506	-1.86	0.41	15.03	59.67	2.62	0.043	0.81	15.2	167.	21.0

[a] *In units of* 10^{-10} *erg* s^{-1} cm^{-2}

This table continues in the next page

This table continues from the previous page

Gamma-ray source	ra [deg]	dec [deg]	s_{max} [deg]	s_{min} [deg]	l [deg]	b [deg]	G_{100} [(a)]	$signif_{avg}$	$\mathcal{V}$	α_γ	$n_{punt\,P}$	$n_{punt\,L}$	$n_{punt\,C}$	$n_{punt\,K}$	h_{trans} [deg]
3FGL J1754.0-2538	268.50	-25.6	0.02	0.02	3.7810	0.084	0.41	16.83	66.89	2.15	0.003	0.07	1.32	14.5	24.8
3FGL J1758.8-2402	269.70	-24.0	0.07	0.07	5.7203	-0.04	0.25	5.339	54.83	1.99	0.026	0.49	9.34	102.	26.4
3FGL J1758.8-2346	269.70	-23.7	0.05	0.05	5.9409	0.081	0.36	7.314	41.79	2.07	0.014	0.27	5.15	56.7	26.7
3FGL J1759.6-2141	269.91	-21.6	0.07	0.05	7.8477	0.960	0.19	5.153	37.28	2.28	0.017	0.33	6.26	68.9	28.8
3FGL J1800.8-2402	270.22	-24.0	0.03	0.03	5.9563	-0.45	0.73	17.48	46.64	2.33	0.005	0.10	1.99	21.9	26.4
3FGL J1801.6-2213	270.40	-22.2	0.05	0.03	7.6147	0.304	0.16	5.131	40.07	1.96	0.010	0.19	3.70	40.7	28.2
3FGL J1802.4-3043	270.61	-30.7	0.08	0.05	0.3038	-4.05	0.10	6.031	37.90	2.11	0.023	0.44	8.29	91.3	19.7
3FGL J1803.1-2728	270.78	-27.4	0.10	0.07	3.2211	-2.58	0.14	5.917	57.27	2.33	0.039	0.75	14.0	154.	23.0
3FGL J1804.5-0850	271.13	-8.84	0.10	0.08	19.649	6.238	0.19	8.071	55.43	2.74	0.046	0.86	16.2	178.	41.6
3FGL J1806.7-2451	271.68	-24.8	0.08	0.06	5.8945	-2.01	0.11	4.210	41.68	2.20	0.029	0.56	10.4	115.	25.6
3FGL J1808.3-3357	272.09	-33.9	0.09	0.08	358.06	-6.71	0.08	8.716	50.88	2.22	0.035	0.67	12.5	137.	16.5
3FGL J1808.4-3519	272.10	-35.3	0.09	0.09	356.85	-7.36	0.07	4.916	28.43	2.30	0.043	0.81	15.2	167.	15.1
3FGL J1809.0+3517	272.27	35.28	0.09	0.08	61.983	23.38	0.04	5.438	38.00	2.44	0.039	0.74	13.8	152.	85.7
3FGL J1809.2-2016c	272.32	-20.2	0.05	0.04	10.182	-0.31	0.32	5.413	42.14	2.32	0.012	0.23	4.33	47.7	30.2
3FGL J1810.7+5335	272.68	53.58	0.09	0.07	81.776	27.40	0.03	5.592	41.36	1.78	0.036	0.69	12.9	142.	75.9
3FGL J1810.8-2412	272.71	-24.2	0.10	0.06	6.9129	-2.52	0.21	6.206	62.02	2.32	0.033	0.63	11.8	130.	26.2
3FGL J1814.0-1757c	273.51	-17.9	0.09	0.06	12.757	-0.17	0.31	5.365	50.07	2.18	0.028	0.53	10.0	110.	32.5
3FGL J1814.1-1734c	273.54	-17.5	0.06	0.05	13.104	-0.02	0.81	9.017	56.90	2.54	0.017	0.33	6.23	68.5	32.9
3FGL J1816.5-1145	274.12	-11.7	0.10	0.08	18.488	2.253	0.23	5.896	48.28	2.48	0.041	0.77	14.4	158.	38.7
3FGL J1817.3-3033	274.34	-30.5	0.09	0.08	1.9905	-6.79	0.06	4.338	56.74	2.18	0.040	0.76	14.2	157.	19.9
3FGL J1819.5-1345	274.89	-13.7	0.08	0.08	17.083	0.645	0.41	7.689	77.81	2.47	0.036	0.67	12.6	139.	36.7
3FGL J1821.9+6636	275.47	66.60	0.09	0.06	96.535	27.63	0.03	6.524	32.86	2.04	0.029	0.55	10.3	114.	62.8
3FGL J1823.2-1339	275.82	-13.6	0.02	0.02	17.604	-0.09	0.92	16.63	47.54	2.22	0.003	0.06	1.24	13.7	36.8
3FGL J1824.3-0620	276.09	-6.33	0.05	0.05	24.198	3.082	0.21	9.762	42.05	2.24	0.014	0.26	4.92	54.1	44.1
3FGL J1827.3-1446	276.83	-14.7	0.06	0.04	17.076	-1.48	0.22	9.099	40.00	2.47	0.013	0.24	4.64	51.0	35.7
3FGL J1827.6-0846	276.90	-8.77	0.05	0.04	22.418	1.241	0.30	8.678	51.62	2.36	0.012	0.23	4.32	47.6	41.7
3FGL J1827.7+1141	276.92	11.69	0.10	0.08	40.781	10.51	0.07	6.490	38.60	2.11	0.042	0.80	14.9	164.	62.2
3FGL J1829.2-1504	277.32	-15.0	0.10	0.06	17.014	-2.04	0.08	5.131	33.49	1.60	0.034	0.64	12.0	132.	35.4
3FGL J1830.7-1630	277.69	-16.5	0.07	0.05	15.911	-3.03	0.30	12.13	49.00	2.43	0.020	0.37	7.04	77.5	33.9
3FGL J1830.8-3136	277.71	-31.6	0.11	0.08	2.3540	-9.84	0.06	5.281	40.87	2.18	0.049	0.92	17.2	190.	18.9
3FGL J1831.7-0230	277.94	-2.50	0.09	0.08	28.458	3.228	0.42	9.250	31.10	2.85	0.038	0.71	13.3	146.	48.0
3FGL J1831.7-0157c	277.94	-1.96	0.10	0.09	28.940	3.471	0.27	5.065	38.17	2.53	0.050	0.95	17.8	196.	48.5
3FGL J1834.8-0630c	278.71	-6.51	0.08	0.07	25.249	0.701	0.21	4.682	36.02	2.21	0.030	0.57	10.6	117.	43.9
3FGL J1837.6-0717	279.40	-7.29	0.08	0.05	24.866	-0.26	0.26	5.551	41.26	2.03	0.023	0.44	8.40	92.4	43.2
3FGL J1838.9-0646	279.72	-6.77	0.07	0.05	25.477	-0.31	0.29	7.123	50.15	1.92	0.022	0.41	7.80	85.9	43.7
3FGL J1839.3-0552	279.84	-5.88	0.03	0.02	26.327	-0.01	1.00	14.91	37.43	2.54	0.004	0.08	1.63	17.9	44.6
3FGL J1842.2+2742	280.56	27.70	0.07	0.06	57.131	14.09	0.07	8.299	38.69	2.13	0.024	0.46	8.60	94.7	78.2
3FGL J1843.7-0322	280.92	-3.37	0.08	0.07	29.046	0.176	0.93	13.08	70.62	2.73	0.031	0.59	11.1	123.	47.1
3FGL J1844.3-0344	281.10	-3.74	0.05	0.04	28.795	-0.14	0.28	10.06	44.78	2.28	0.012	0.23	4.45	49.0	46.7

[a] *In units of* 10^{-10} *erg* s^{-1} cm^{-2}

This table continues in the next page

This table continues from the previous page

Gamma-ray source	ra [deg]	dec [deg]	s_{max} [deg]	s_{min} [deg]	l [deg]	b [deg]	G_{100} [(a)]	$signif_{avg}$	$\mathcal{V}$	α_γ	$n_{punt\,P}$	$n_{punt\,L}$	$n_{punt\,C}$	$n_{punt\,K}$	h_{trans} [deg]
3FGL J1844.7-1224	281.18	-12.4	0.10	0.08	21.109	-4.16	0.10	5.359	52.43	2.27	0.040	0.76	14.3	157.	38.0
3FGL J1845.5-2524	281.38	-25.4	0.10	0.08	9.4406	-10.0	0.12	9.181	40.44	2.28	0.042	0.79	14.8	163.	25.0
3FGL J1848.4-0141	282.11	-1.69	0.08	0.05	31.088	-0.11	1.14	18.67	52.63	2.58	0.022	0.41	7.84	86.2	48.8
3FGL J1849.5-0124c	282.39	-1.41	0.07	0.06	31.463	-0.23	0.34	4.902	36.74	2.28	0.024	0.46	8.60	94.7	49.0
3FGL J1850.5-0024	282.63	-0.40	0.05	0.04	32.468	0.017	0.57	9.435	64.26	2.41	0.011	0.21	4.03	44.4	50.1
3FGL J1852.8+0158	283.20	1.972	0.06	0.05	34.847	0.587	0.82	13.71	54.51	2.54	0.016	0.31	5.91	65.0	52.4
3FGL J1855.4+0454	283.85	4.911	0.08	0.06	37.758	1.352	0.45	9.476	38.60	2.54	0.028	0.54	10.1	111.	55.4
3FGL J1856.1-1217	284.03	-12.2	0.06	0.05	22.464	-6.60	0.14	8.368	50.87	2.58	0.018	0.35	6.63	73.0	38.2
3FGL J1857.2+0059	284.31	0.986	0.04	0.03	34.471	-0.84	0.48	12.39	57.13	2.26	0.007	0.13	2.56	28.2	51.4
3FGL J1857.8+0129c	284.47	1.497	0.10	0.07	35.000	-0.75	0.31	4.475	41.47	2.34	0.037	0.70	13.2	145.	52.0
3FGL J1857.9+0355	284.48	3.927	0.07	0.06	37.170	0.342	0.37	9.268	55.58	2.68	0.022	0.41	7.78	85.6	54.4
3FGL J1857.9+0210	284.49	2.170	0.06	0.05	35.607	-0.46	0.68	15.18	50.61	2.59	0.016	0.31	5.87	64.6	52.6
3FGL J1901.1+0728	285.29	7.475	0.10	0.10	40.693	1.249	0.31	8.694	55.34	2.73	0.051	0.96	18.0	198.	57.9
3FGL J1901.5-0126	285.39	-1.44	0.05	0.05	32.801	-2.92	0.36	13.97	60.36	2.61	0.014	0.27	5.04	55.5	49.0
3FGL J1902.6+0655	285.65	6.931	0.08	0.05	40.373	0.682	0.22	5.976	32.63	2.23	0.021	0.40	7.59	83.5	57.4
3FGL J1903.9+0052	285.99	0.869	0.07	0.07	35.139	-2.39	0.10	4.389	48.26	2.14	0.027	0.50	9.50	104.	51.3
3FGL J1904.7-0708	286.19	-7.13	0.06	0.06	28.071	-6.20	0.21	11.68	57.99	2.58	0.020	0.37	7.05	77.6	43.3
3FGL J1904.9+0818	286.24	8.306	0.10	0.07	41.861	0.795	0.16	4.663	48.07	2.29	0.040	0.76	14.3	158.	58.8
3FGL J1906.6+0720	286.67	7.333	0.03	0.02	41.192	-0.02	0.99	26.27	41.70	2.35	0.004	0.09	1.69	18.6	57.8
3FGL J1911.7+0307	287.93	3.130	0.08	0.06	38.036	-3.07	0.14	7.057	52.94	2.32	0.027	0.51	9.64	106.	53.6
3FGL J1915.2+0954	288.80	9.908	0.09	0.07	44.449	-0.70	0.31	7.705	52.03	2.60	0.034	0.65	12.2	134.	60.4
3FGL J1917.1-3024	289.28	-30.4	0.09	0.07	7.5514	-18.4	0.10	9.548	46.07	2.23	0.033	0.62	11.7	129.	20.0
3FGL J1919.9+1407	289.98	14.11	0.07	0.06	48.710	0.241	0.46	10.87	67.72	2.69	0.023	0.43	8.14	89.5	64.6
3FGL J1922.2+2313	290.56	23.22	0.07	0.05	57.022	4.022	0.03	4.682	43.62	1.62	0.018	0.35	6.66	73.3	73.7
3FGL J1924.8-1034	291.20	-10.5	0.11	0.08	27.158	-12.1	0.13	10.53	48.62	2.34	0.043	0.82	15.3	169.	39.9
3FGL J1925.4+1727	291.37	17.46	0.10	0.08	52.291	0.638	0.21	9.610	47.33	2.24	0.042	0.80	15.0	165.	67.9
3FGL J1928.9+1739	292.23	17.65	0.08	0.05	52.854	0.007	0.25	8.506	47.86	2.63	0.022	0.42	7.92	87.2	68.1
3FGL J1934.2+6002	293.55	60.03	0.07	0.05	91.826	18.21	0.03	6.571	35.67	2.14	0.019	0.36	6.87	75.6	69.4
3FGL J1943.8+2518	295.97	25.30	0.12	0.08	61.222	0.708	0.16	6.386	40.48	2.35	0.052	0.98	18.4	203.	75.8
3FGL J1944.0-0535	296.00	-5.59	0.10	0.08	33.905	-14.2	0.05	4.365	51.19	2.34	0.045	0.84	15.8	174.	44.9
3FGL J1944.1+3919	296.03	39.32	0.07	0.06	73.482	7.584	0.05	6.181	55.29	2.18	0.024	0.46	8.70	95.8	89.8
3FGL J1944.8+4300	296.22	43.00	0.09	0.08	76.807	9.241	0.03	4.254	39.74	2.01	0.041	0.77	14.4	158.	86.4
3FGL J1949.3+2433	297.32	24.56	0.07	0.06	61.203	-0.72	0.16	8.171	42.17	2.77	0.025	0.47	8.79	96.7	75.0
3FGL J1949.6+2355	297.41	23.92	0.10	0.09	60.689	-1.11	0.12	4.709	30.03	2.29	0.048	0.91	17.1	188.	74.4
3FGL J1958.1+2436	299.52	24.61	0.06	0.04	62.274	-2.41	0.06	5.321	47.27	1.67	0.014	0.27	5.11	56.3	75.1
3FGL J2004.4+3338	301.10	33.64	0.03	0.03	70.671	1.185	0.43	18.46	50.29	2.29	0.005	0.10	1.98	21.8	84.1
3FGL J2006.6+0150	301.65	1.846	0.06	0.06	43.443	-15.7	0.04	5.517	30.06	1.87	0.020	0.39	7.30	80.4	52.3
3FGL J2014.5+5246	303.64	52.76	0.08	0.07	87.889	9.900	0.04	4.388	49.03	2.42	0.028	0.53	9.93	109.	76.7
3FGL J2015.3-1431	303.84	-14.5	0.06	0.06	28.806	-25.0	0.02	4.791	33.03	1.77	0.019	0.37	6.94	76.4	35.9

[a] *In units of* 10^{-10} *erg* s^{-1} cm^{-2}

This table continues in the next page

This table continues from the previous page

Gamma-ray source	ra [deg]	dec [deg]	s_{max} [deg]	s_{min} [deg]	l [deg]	b [deg]	G_{100} [(a)]	$signif_{avg}$	$\mathcal{V}$	α_γ	$n_{punt\,P}$	$n_{punt\,L}$	$n_{punt\,C}$	$n_{punt\,K}$	h_{trans} [deg]
3FGL J2017.9+3627	304.48	36.45	0.03	0.03	74.541	0.410	0.65	25.03	39.85	2.61	0.005	0.09	1.85	20.4	86.9
3FGL J2023.5+4126	305.87	41.43	0.09	0.09	79.253	2.341	0.34	11.63	48.95	2.53	0.042	0.80	15.0	165.	88.0
3FGL J2024.8-2331	306.21	-23.5	0.08	0.07	20.240	-30.3	0.02	4.208	37.63	1.94	0.028	0.53	9.96	109.	26.9
3FGL J2025.1-2858	306.27	-28.9	0.09	0.07	14.174	-32.0	0.03	4.546	32.87	2.18	0.034	0.65	12.1	133.	21.5
3FGL J2026.3+1430	306.58	14.51	0.09	0.07	57.260	-13.4	0.06	7.096	48.74	2.15	0.033	0.62	11.7	128.	65.0
3FGL J2030.5-1439	307.62	-14.6	0.07	0.06	30.304	-28.4	0.02	4.441	39.49	1.86	0.023	0.44	8.26	90.9	35.8
3FGL J2032.5+3921	308.13	39.35	0.09	0.06	78.573	-0.26	0.31	11.31	49.41	2.64	0.031	0.60	11.2	123.	89.8
3FGL J2033.3+4348c	308.33	43.81	0.07	0.06	82.243	2.258	0.12	4.392	39.38	2.24	0.022	0.42	7.92	87.2	85.6
3FGL J2034.4+3833c	308.62	38.56	0.05	0.05	78.158	-1.04	0.26	8.889	55.76	2.52	0.013	0.24	4.65	51.1	89.0
3FGL J2035.0+3634	308.75	36.58	0.05	0.04	76.633	-2.31	0.12	11.92	52.58	1.89	0.011	0.21	3.92	43.1	87.0
3FGL J2035.6+3146	308.90	31.77	0.10	0.08	72.840	-5.28	0.08	4.602	45.38	2.67	0.041	0.78	14.6	161.	82.2
3FGL J2035.8+4902	308.95	49.04	0.05	0.04	86.712	5.034	0.06	4.771	44.30	2.09	0.013	0.24	4.58	50.4	80.4
3FGL J2036.8+4234c	309.22	42.56	0.07	0.07	81.633	0.997	0.19	5.376	42.08	2.25	0.027	0.51	9.62	105.	86.9
3FGL J2037.4+4132c	309.35	41.53	0.08	0.07	80.868	0.294	0.20	6.446	40.86	2.17	0.030	0.57	10.7	117.	87.9
3FGL J2038.4+4212	309.62	42.20	0.05	0.05	81.527	0.542	0.39	11.75	45.66	2.69	0.015	0.28	5.34	58.8	87.2
3FGL J2041.1+4736	310.28	47.60	0.05	0.04	86.091	3.461	0.31	18.37	56.27	2.13	0.011	0.22	4.16	45.8	81.8
3FGL J2043.6+0001	310.90	0.028	0.10	0.08	46.611	-24.7	0.02	4.259	41.63	1.68	0.041	0.77	14.5	159.	50.5
3FGL J2047.9-3119	311.98	-31.3	0.11	0.07	12.830	-37.3	0.06	7.103	44.27	2.52	0.044	0.83	15.5	170.	19.1
3FGL J2053.9+2922	313.47	29.37	0.04	0.04	73.361	-9.86	0.06	7.720	45.97	1.54	0.008	0.16	3.07	33.8	79.8
3FGL J2102.8+4704	315.72	47.06	0.09	0.07	88.034	0.281	0.09	5.729	45.48	2.07	0.032	0.61	11.4	126.	82.4
3FGL J2103.7-1113	315.94	-11.2	0.06	0.05	37.857	-34.4	0.06	12.32	50.07	1.93	0.017	0.33	6.26	68.9	39.2
3FGL J2104.7+2113	316.19	21.22	0.07	0.06	68.447	-16.9	0.03	4.985	34.31	2.05	0.025	0.47	8.95	98.5	71.7
3FGL J2108.1+5202	317.04	52.04	0.08	0.06	92.302	2.977	0.24	9.666	57.21	2.50	0.024	0.46	8.69	95.6	77.4
3FGL J2109.4+1437	317.35	14.61	0.11	0.09	63.688	-21.8	0.10	10.20	101.6	2.73	0.051	0.96	18.0	198.	65.1
3FGL J2110.4+5946	317.61	59.77	0.07	0.07	98.252	7.967	0.09	7.387	45.32	2.53	0.027	0.51	9.58	105.	69.7
3FGL J2112.5-3044	318.14	-30.7	0.03	0.03	14.898	-42.4	0.19	30.14	51.84	1.67	0.005	0.10	1.96	21.6	19.7
3FGL J2114.0+5239	318.52	52.65	0.06	0.05	93.366	2.734	0.11	6.950	56.83	2.38	0.019	0.37	6.97	76.7	76.8
3FGL J2117.6+3725	319.42	37.42	0.11	0.08	82.798	-8.27	0.12	14.49	49.94	2.09	0.047	0.88	16.5	181.	87.9
3FGL J2134.5-2131	323.64	-21.5	0.05	0.04	28.921	-45.0	0.07	11.43	46.09	2.13	0.012	0.22	4.28	47.2	28.9
3FGL J2142.7+1957	325.68	19.95	0.06	0.06	73.733	-24.3	0.02	4.440	37.63	2.00	0.019	0.37	6.92	76.1	70.4
3FGL J2144.6+6606	326.16	66.10	0.09	0.08	105.52	9.766	0.06	4.092	43.67	2.45	0.039	0.74	13.8	152.	63.3
3FGL J2145.5+1007	326.37	10.13	0.06	0.06	66.047	-31.5	0.02	5.198	38.22	1.55	0.019	0.36	6.81	74.9	60.6
3FGL J2151.6+4154	327.90	41.90	0.05	0.04	90.718	-9.44	0.06	8.404	33.77	1.84	0.012	0.24	4.53	49.8	87.5
3FGL J2209.8-0450	332.46	-4.84	0.08	0.07	55.685	-45.5	0.04	6.460	45.62	1.26	0.030	0.57	10.7	118.	45.6
3FGL J2210.1+6043	332.53	60.72	0.05	0.05	104.44	3.782	0.06	5.158	34.82	2.21	0.015	0.28	5.37	59.1	68.7
3FGL J2210.2+6509	332.55	65.16	0.09	0.08	107.03	7.396	0.08	4.390	36.96	2.47	0.036	0.68	12.8	141.	64.3
3FGL J2212.5+0703	333.14	7.059	0.09	0.08	68.742	-38.5	0.09	14.27	57.47	2.00	0.038	0.72	13.5	149.	57.5
3FGL J2217.2+6346	334.30	63.77	0.06	0.05	106.86	5.823	0.11	7.129	38.68	2.30	0.018	0.34	6.50	71.5	65.7
3FGL J2223.3+0103	335.83	1.051	0.08	0.06	65.216	-44.5	0.04	6.337	41.57	1.80	0.027	0.50	9.50	104.	51.5

[a] *In units of* 10^{-10} *erg* s^{-1} cm^{-2}

This table continues in the next page

This table continues from the previous page

Gamma-ray source	ra [deg]	dec [deg]	s_{max} [deg]	s_{min} [deg]	l [deg]	b [deg]	G_{100} [(a)]	$signif_{avg}$	$\mathcal{V}$	α_γ	$n_{punt\,P}$	$n_{punt\,L}$	$n_{punt\,C}$	$n_{punt\,K}$	h_{trans} [deg]
3FGL J2224.4+0351	336.10	3.859	0.07	0.05	68.337	-42.9	0.03	5.843	34.30	1.59	0.018	0.34	6.53	71.9	54.3
3FGL J2228.5-1636	337.14	-16.6	0.10	0.09	43.120	-55.3	0.04	5.734	49.62	2.50	0.046	0.87	16.2	179.	33.9
3FGL J2229.1+2255	337.28	22.92	0.05	0.05	85.032	-29.2	0.04	6.497	44.21	2.23	0.012	0.23	4.36	47.9	73.4
3FGL J2233.1+6542	338.27	65.71	0.09	0.08	109.34	6.561	0.17	12.69	52.49	2.27	0.039	0.75	14.0	154.	63.7
3FGL J2237.9+6320	339.48	63.33	0.10	0.09	108.59	4.240	0.09	7.222	43.19	2.46	0.044	0.84	15.7	172.	66.1
3FGL J2244.6+2503	341.16	25.05	0.09	0.07	89.763	-29.5	0.02	4.341	41.65	1.91	0.033	0.63	11.9	130.	75.5
3FGL J2247.2-0004	341.81	-0.07	0.06	0.05	69.996	-49.7	0.07	10.07	48.40	2.10	0.017	0.33	6.21	68.4	50.4
3FGL J2250.3+1747	342.58	17.79	0.09	0.07	86.354	-36.3	0.11	7.183	87.05	2.78	0.033	0.63	11.8	129.	68.3
3FGL J2300.0+4053	345.02	40.89	0.05	0.05	101.24	-17.2	0.02	5.243	36.24	1.51	0.015	0.28	5.27	58.0	88.5
3FGL J2303.7+5555	345.94	55.91	0.05	0.05	108.20	-3.84	0.03	5.608	37.93	1.75	0.013	0.26	4.87	53.6	73.5
3FGL J2309.0+5428	347.25	54.47	0.08	0.07	108.32	-5.46	0.02	4.580	34.10	1.69	0.028	0.52	9.86	108.	75.0
3FGL J2321.3+5113	350.34	51.22	0.08	0.08	108.87	-9.17	0.03	4.332	39.18	2.01	0.034	0.64	12.1	133.	78.2
3FGL J2329.8+6102	352.45	61.04	0.06	0.05	113.21	-0.28	0.06	5.633	38.02	2.06	0.017	0.33	6.23	68.5	68.4
3FGL J2358.5+3827	359.63	38.45	0.10	0.07	111.68	-23.2	0.04	5.892	52.31	2.07	0.036	0.68	12.7	140.	88.9
3FGL J2358.6-1809	359.66	-18.1	0.07	0.06	66.603	-74.8	0.03	6.513	48.80	1.81	0.022	0.41	7.82	86.1	32.3

[a] *In units of* 10^{-10} *erg* s^{-1} cm^{-2}

This table is concluded from previous page